SYNTHESIS AND CHARACTERIZATION OF HOLLOW CORE-SHELL SILICA NANOPARTICLES AS DRUG DELIVERY VECTOR

Thesis

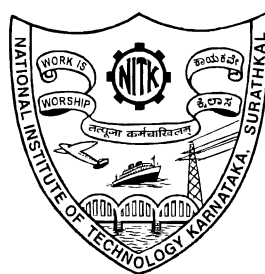Submitted in partial fulfillment of the requirements for the degree of

DOCTOR OF PHILOSOPHY

By

DEEPIKA D.

Register No. 155005CH15F03

DEPARTMENT OF CHEMICAL ENGINEERING

NATIONAL INSTITUTE OF TECHNOLOGY KARNATAKA,

SURATHKAL, MANGALORE - 575025

DECEMBER, 2020

D E C L A R A T I O N

I hereby *declare* that the Research Thesis entitled **"SYNTHESIS AND CHARACTERIZATION OF HOLLOW CORE-SHELL SILICA NANOPARTICLES AS DRUG DELIVERY VECTOR"** which is being submitted to the **National Institute of Technology Karnataka, Surathkal** in partial fulfilment of the requirements for the award of the Degree of **Doctor of Philosophy** in the **Department of Chemical Engineering** is a *bonafide report of the research work carried out by me*. The material contained in this Research Thesis has not been submitted to any University or Institution for the award of any degree.

DEEPIKA D
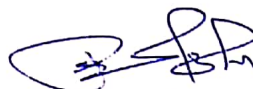
Register Number: 155005CH15F03

Department of Chemical Engineering

Place: NITK Surathkal,

Date: 14/12/2020

CERTIFICATE

This is to certify that the Research Thesis entitled **"SYNTHESIS AND CHARACTERIZATION OF HOLLOW CORE-SHELL SILICA NANOPARTICLES AS DRUG DELIVERY VECTOR"** submitted by **Mrs. Deepika D (Register Number: 155005CH15F03)** as the record of the research work carried out by her, *is accepted as the Research Thesis submission* in partial fulfilment of the requirements for the award of degree of **Doctor of Philosophy.**

Research Guide

Dr. P. E. JagadeeshBabu

Associate Professor

Department of Chemical Engineering

NITK, Surathkal

Chairman- DRPC

Department of Chemical Engineering

NITK, Surathkal

Srinivasnagar, Mangalore- 575025

ACKNOWLEDGEMENT

Deepika D

DEDICATED TO MY

BELOVED HUSBAND

ABSTRACT

Nanodrug carriers are found to be better choice in the treatment of benign cancerous tumors which deliver small dosages of drugs specific to the diseased area. Scarcity in the emergence of new drug carriers with specific features like targeted delivery, higher drug loading capacity and biocompatibility has enhanced the research interest in them. Hollow core-shell silica nanoparticles (HCSNs) are being considered as one of the most favorable nanodrug carriers to accomplish targeted drug delivery, due to their unique properties like large surface area, tunable thickness, tunable pore diameter, low density, high chemical/thermal stability and good biocompatibility.

In the present research work, we report a simple two-step method to synthesize HCSNs. HCSNs are synthesized using sacrificial template method. Polystyrene nanoparticles and funtionalized polystyrene nanoparticles (sulfonate and nitro functionalization) are used as sacrificial templates to obtain desirable morphology for the HCSNs. Polymer templates are synthesized in the first step and they are used as sacrificial templates in the second step during the synthesis of HCSNs by modified Stober method. Effect of the parameters like water-ethanol volume ratio, concentration of ammonia, concentration of cetyl trimethylammonium bromide (CTAB) and PS/tetraethyl orthosilicate (TEOS) weight ratio on morphology of HCSNs is analyzed. Further, polystyrene nanoparticles are functionalized to improve the surface charge properties by sulfonation and nitration. Functionalized PS nanoparticles are used as templates for the synthesis of HCSNs with enhanced shell thickness and pore size respectively. Effect of surface area, thickness of the silica shell and pore size on drug release from HCSNs are studied in detail using doxorubicin as a model drug.

Application of HCSNs synthesized using sulfonated PS in sustained release of doxorubicin is found to be advantageous compared to the other synthesized samples. The properties of HCSNs samples synthesized using sulfonated PS such as higher shell thickness and pore size lead to higher encapsulation efficiency with sustained release of doxorubicin for 300 minutes. SPION embedded HCSNs are synthesized by sacrificial PS

template method. Presence of SPION is an added advantage which aided radio frequency heating of the nanoparticles and allowed to study the variation of SPION concentration on the temperature rise. The release of drug from the SPION embedded HCSNs are found to be temperature dependant. The doxorubicin release kinetic profiles of HCSNs and SPION embedded HCSNs are studied using models such as zero order, first order and Higuchi model. Release kinetics showed best fit for first order model. In vitro cytotoxicity assays carried out on normal cells and cancer cells confirmed the biocompatibility of HCSNs and SPION embedded HCSNs. However, doxorubicin loaded samples achieved death of >85% of the cancer cells.

Keywords: Hollow core-shell, silica nanoparticles, polystyrene, doxorubicin, drug delivery, pore size, surface area, shell thickness

TABLE OF CONTENTS

targeted drug delivery

LIST OF FIGURES

LIST OF TABLES

LIST OF ABBREVIATIONS

BET	Brunauer-Emmett-Teller
BJH	Barrett-Joyner-Halenda
CTAB	Cetyl trimethyl ammonium bromide
CTMA	Cetyl trimethyl ammonium chloride
DMEM	Dulbecco's modified eagles medium
FESEM	Field emission scanning electron microscope
FTIR	Fourier transform infrared spectroscope
KPS	Potassium persulfate
HCSNs	Hollow core–shell silica nanoparticles
MPS	3-(trimethoxysilyl)-propyl methacrylate
MRI	Magnetic resonance image
MSNs	Mesoporous silica nanoparticles
MTT	3-(4,5-dimethylthiazol-2-yl)-2,5-diphenyltetrazolium bromide
OVAT	One variable at a time method
PAA	Polyacrylic acid
PS	Polystyrene
PSS	Polystyrene sulfonate acid sodium salt
PVP	Polyvinyl pyrrolidone
SDS	Sodium dodecyl sulfonate
SEM	Scanning electron microscope
SPION	Superparamagnetic iron oxide nanoparticle
SQUID	Superconducting quantum interference device
TEOS	Tetraethyl orthosilicate
TEM	Transmission electron microscope
TGA	Thermogravimetric analysis
VSM	Vibrating sample magnetometer
XRD	X-ray diffraction

NOMENCLATURE

t   Time

Q_t Quantity of drug released at time t

Q_0 Initial amount of drug in the medium

k_0 Rate constant for the zero order model

C_t Concentration of drug released in time t

C_0 Initial concentration of drug remaining in the silica nanoparticles

k_1 First order rate constant

k_H Higuchi constant

vol%   Volume percentage

wt%   Weight percentage

CHAPTER 1

1. INTRODUCTION

1.1 Background of the research and motivation

Drugs play a crucial role in human lives by preventing, reducing and eradicating various diseased states. The science of drug development includes various stages such as discovery, development and usage of the drug. A drug from its design stage to commercialization stage is a tedious and expensive process that requires high quality research in each step. The success rate of a drug formulation depends on several parameters such as pharmacokinetics, efficacy, toxicology, physical and chemical properties (Kuhlmann 1997). The utilization of drugs in daily life has elevated to a greater degree with rise in ageing population since 1980. The significant number of side effects associated with the usage of drugs continued to increase as the usage of drugs increased (Kwon et al. 2013; Zhang et al. 2007). The constraints of conventional medical practices in diagnosis and therapy of various diseases could be uplifted by the application of nanomedicine. Modern healthcare techniques use nanomedicines for the treatment of various diseases.

Nanomedicine is one of the tools being widely used in targeted drug delivery systems to carry drugs into the human body (Balakrishnan et al. 2013). Superior drug carrier designs with multifunctional properties are part of smart drug delivery systems. Nano drug carriers can be used in the treatment of benign cancer causing tumors, which involve uncontrollable and abnormal growth of tissues (Thakur et al. 2017). The difficulties linked with the traditional treatment techniques have given a new horizon for the development of smart drug delivery systems using nanodrug carriers. In the case of targeted drug delivery systems, the drugs can be delivered to a specific diseased site in the form of small dosages. The traditional methods to cure cancer are surgery, chemotherapy and radiotherapy. Surgery is not an efficient route to cure cancer. The healthy tissues also get affected while the cancer cells are treated by chemotherapy

technique. Some of the present cancer medicines are found to be deficit in specificity and selectivity. But, the usage of higher concentration of drug during the remediation of the disease will lead to the undesirable side reactions on the healthy organs. However, reducing the drug quantity may not be effective in curing the disease and thus, there is a need for intelligent drug delivery system which can enhance the effectiveness of the drug at low cost and with less toxicity (Kwon et al. 2013; Obayemi et al. 2016).

Superior drug carriers with multifunctional properties are part of the smart drug delivery systems. The drugs can be delivered to a specific diseased site in the form of small dosages for longer period using a targeted and sustained drug delivery system. The major disadvantages of conventional drugs are poor stability, poor solubility, low shelf life and low specificity in comparison with the targeted drug delivery system. Drugs are also needed in larger dosages due to their reduced absorption by the tissues which have lowered the therapeutic value. These difficulties could be overcome by employing the targeted drug delivery systems (Lim et al. 2013). It is a technique where the therapeutic amount of drug is delivered to the specific diseased area for desired time period. Success of a targeted drug delivery also depends on the drug carrier or drug deliver vector which holds the drug and carries to the desired site. Nano sized drug carriers have received great recognition, since they could be multifunctional and allow hassle free synthesis at low cost.

Smart nano drug delivery systems used in treating organs or cells and they can release the drug in the controlled fashion by virtue of various internal and external triggers such as pH, specific surface area and thickness of the shell. An ideal drug delivery system must have certain salient features (Rani and Paliwal 2014). First a developer should know about the nature of the disease whether acute or chronic and the organs/tissues affected. The characteristics of the drug, specific functional groups present and side effects have to be studied before developing a drug carrier. The drug carrier should be nontoxic and should not show any biochemical interactions with the healthy tissues and should be removed from the body without any issues. The drug carrier should be mechanically,

2

physically and chemically stable in the drug delivery environment. Drug delivery should be limited to the targeted tissues with consistent supply. Drug release rate should be anticipated prior to its application. Facile method for the synthesis of drug carrier should be adopted which could be reproducible at ease and reduced cost.

Various nano sized drug carriers employed in drug delivery application are dendrimers, liposomes, polymers, carbon materials, mesoporous silica nanoparticles (MSNs), titanium dioxide, gold and iron oxide nanoparticles (Kwon et al. 2013).

Dendrimers: Dendrimers are biomolecules with defined structures and with high functionality that are used in drug delivery system and the best example is polyamidoamine. The toxicity of the dendrimers limit their application in targeted drug delivery system, even though they can carry the drug to the specified site (Kumar et al. 2014).

Liposomes: Liposomes are spherical in nature, which are made up of multiple layers of lipid with a hollow aqueous core, which are also used as drug carriers. Liposomes are nontoxic and they can deliver both hydrophobic and hydrophilic drugs to the diseased area. However, they have a low shelf life and lack in solubility (Alavi et al. 2017).

Polymers: Polymers such as hydrogels are good options as drug delivery vectors. They have porous and hydrated structures which resemble the properties of tissue microenvironment (Siamak and Hassan 2018). Polymers are capable of carrying the encapsulated drugs and release it in the inaccessible cancer site or targeted site without causing any damage to the surrounding healthy tissues.

Carbon materials: Carbon materials such as carbon nanotubes are used as drug deliver vector due to their flexibility in synthesis. Their unique properties allow the transportation of medicines such as vaccine, protein and antibiotics. But insolubility of the carbon nanostructures may cause health issues (Elhissi et al. 2001).

Titanium dioxide: Titanium dioxide films are also used in the form of micro or nano-porous structures that can be loaded with the drug/antibiotic. These loaded films can be applied to the tumor site to destroy the tumor. However, they show a potential risk in pulmonary problems (Kafshgari et al. 2019; Kwon et al. 2013).

Gold and iron oxide nanoparticles: They are widely used in the form of composites with other materials such as silica or polymer. The synthesis of gold nanoparticles is found to be considerably expensive. Iron oxide nanoparticles require surface treatments, since they have poor solubility (Kong et al. 2017; Kopanja et al. 2016).

MSNs: MSNs are one of the assured drug delivery vectors since they have mesoporous structure with numerous benefiting features. They can be synthesized in the form of hollow core-shell structures with mesoporous shell. Studies on the biomedical applications of hollow core–shell silica nanoparticles (HCSNs) are comparatively less than that of mesoporous silica nanoparticles. The schematic representation of the application of hollow core-shell nanoparticles in drug delivery is depicted in Figure 1.1.
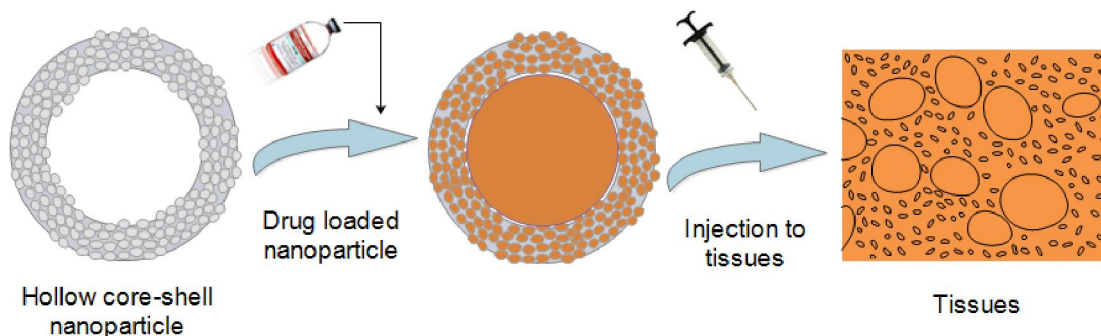
Figure 1.1 Schematic representation of the application of hollow core-shell nanoparticles in drug delivery

The properties of HCSNs that are suitable for drug delivery system are listed below (Liberman et al. 2014).

1. Tunable particle size: HCSNs can be synthesized in the size range of 50 nm to 300 nm without causing cytotoxicity and permitting endocytosis by the living cells.

2. Stability: HCSNs are stable at different pHs and temperatures in comparison with other polymeric and biomolecular drug carriers. They have higher mechanical strength and good chemical resistance.

3. Tunable pore size: HCSNs can be produced with narrow pore sizes and they can be tuned accordingly. Thus, they empower drug loading at different dosages and slow release to the target site.

4. Large surface area and high pore volume: They have a high surface area with low density and thus making them as a lightweight material. High pore volume enables the higher loading capacity (Slowing et al. 2008).

HCSNs can be synthesized using different synthesis techniques like sacrificial template, hydrothermal, sol/gel, galvanic displacement, self assembly, solvothermal method, solution growth method and sonochemical methods. Among the various available synthesis techniques, sacrificial template method is one of the most versatile methods adopted for the synthesis of HCSNS at sub-micrometer or nanometer scale. Two major categories of templates that are used in the synthesis of HCSNs are soft templates and hard templates. Soft templates include surfactants, micelles and gas bubbles. But soft templates do not assure fabrication of uniform and tunable hollow particles. Thus, usage of hard templates like polymer, SiO_2 and carbon are preferred. During the synthesis of HCSNs, silica particles were coated on the hard templates (Li et al. 2010). It is possible to synthesize the desirable morphology for HCSNs by controlling the reaction parameters. Further, the template particles are eliminated by dissolving it in a suitable medium or by calcination at high temperatures (Chen 2012). Thus, we can obtain a hollow internal core and porous shell structure of silica nanoparticles.

Polystyrene (PS) is a widely used as the sacrificial template due to its uniform spherical shape, monodispersity and wide particle size range. They are synthesized in the form of nanoparticles by emulsion polymerization. PS nanoparticles were found to be

advantageous in the synthesis of nanostructured materials (Milosevic et al. 2009). Modifying the surface charge properties and synthesis of the composite of HCSNs with iron oxide nanoparticles are found to be added advantage for the drug delivery vector.

Superparamagnetic iron oxide nanoparticles (SPIONs) are composited with HCSNs due to their unique properties such as physical, electrical and magnetic properties. The primary causes for these properties are nanoscale sizes and large surface area. Magnetic nanoparticles are utilized in various bio-applications like magnetic bioseparation, detection of biological entities, diagnosis of diseases using magnetic resonance image technique (MRI), treatment using magnetic fluid hyperthermia and targeted drug delivery (Wu et al. 2008). Superparamagnetic nature without hysteresis and any remnant magnetization in an applied magnetic field enable them for the application in cancer therapy as well (Mulens et al. 2013). Magnetic hyperthermia treatment on the tumor site introduces heat by the magnetic energy loss. SPIONs are utilized to accomplish the selective death of cancer cells with hyperthermia treatments. Some of the heating methods such as microwaves, laser and ionizing radiation would also affect the healthy tissues surrounding the cancer cells. However, magnetic hyperthermia involves electromagnetic radiation in the range of radiofrequency which is found to be healthy.

Absence of remnant magnetization when the magnetic field is removed is one of the most favorable magnetic properties for biomedical applications, which is referred as superparamagnetic behavior. Since magnetic dipolar interactions and agglomerations of particles would lead to the formation of blood clots and other unfavorable health conditions. Particle size of iron oxide nanoparticles plays a major role in controlling superparamagnetic nature. Particle size below a critical size is used in biomedical field, since iron oxide nanoparticles become ferromagnetic above the critical size. SPIONs can be determined and targeted to the specific site in the body by means of their magnetic properties. SPIONs can be readily eradicated from the body by the renal clearance mechanisms and reticuloendothelial system (Lopez et al. 2013).

HCSNs are found to have good biocompatibility and chemical stability which fit to the basic requirements of targeted drug delivery systems. The tunable morphology of mesoporous silica nanoparticles has permitted the incorporation of drug particles and deliver to the targeted diseased sites (He and Shi 2011; Kwon et al. 2013). The drug release rate depends on parameters like variation in pore size, shell thickness and surface area of silica nanoparticles (Jiao et al. 2012; Mohamed El-Toni et al. 2012). There are fewer studies which evaluated the loading and release properties of HCSNs with varied shell thickness and narrow pore size.

In the present research work, we report a simple two-step method to synthesize HCSNs. As a first step PS nanoparticles are synthesized and then the synthesized PS nano particles are used as sacrificial templates in the second step while synthesizing HCSNs by modified Stober method. Effect of operating parameters like water-ethanol volume ratio, concentration of ammonia, concentration of cetyl trimethylammonium bromide (CTAB) and PS/tetraethyl orthosilicate (TEOS) weight ratio on the morphology of HCSNs is analyzed. Further, PS nanoparticles are functionalized to improve the surface charge properties by sulfonation and nitration. Functionalized PS nanoparticles are used as templates for the synthesis of HCSNs to enhance shell thickness and pore size respectively. Effect of surface area and thickness of the silica shell on drug release from HCSNs are studied in detail using doxorubicin as a model drug. SPION embedded HCSNs are also synthesized by the sacrificial PS template method. The presence of SPION is an added advantage which aided radiofrequency heating of the nanoparticles and allowed to study the variation of SPION concentration on the temperature rise. Temperature dependence of the release of drug from the SPION embedded HCSNs is determined and analyzed. The doxorubicin release kinetics is fitted on zero order, first order and Higuchi model to determine the release mechanism. In vitro cytotoxicity assays were carried out on normal cells and cancer cells to determine the biocompatibility of HCSNs and SPION embedded HCSNs.

CHAPTER 2

2. LITERATURE REVIEW

2.1 Inorganic core-shell nanoparticles

Inorganic core-shell nanoparticles have attracted significant attention in the recent past, due to their wide range of applications in various fields such as environmental pollution treatments, catalysis, energy storage and biomedical (Kumar and Himanshu 2014; Sandberg et al. 2013; Zhang et al. 2013). Pollution control methods comprised of the catalytic absorption of toxic gases, absorption of heavy metal ions and CO_2. Inorganic core-shell materials were utilized in thermal insulations, batteries and electronic devices. They exhibited good performance in the biomedical field when they were employed in controlled drug delivery, enzyme/protein immobilization, molecular imaging and tissue engineering (Chen 2012). These applications were achieved mainly due to the unique properties like large surface area (Zhao et al. 1998; Zhou et al. 2014), tunable shell thickness (Jiao et al. 2012), tunable pore diameter (Slowing et al. 2008), low density, high chemical/thermal stability and good biocompatibility (Liu et al. 2012).

Synthesis techniques reported in the literature for various hollow core-shell nanoparticles are sacrificial template, hydrothermal, sol/gel, galvanic displacement, self assembly, solvothermal method, solution growth method and sonochemical techniques. Fe_2O_3/SnO_2 hollow nanoparticles were synthesized through a hydrothermal method and used in gas sensors (Zhang et al. 2013). Similarly sol/gel method was adopted for the synthesis of mesoporous aluminium composite with silica nanoparticles for petrochemical refinery (Keshavarz and Ahmad 2013). Galvanic displacement method was used to obtain hollow Au/Pt particles, Au/Pd core–shell nanoparticles, hollow metallic Au and Pt nanoparticles from silver nanoparticles. In this method, higher reduction potential of gold compared to platinum and palladium allowed to produce hollow gold nanoparticles by galvanic displacement with silver (Song et al. 2012). Solution growth method is used by Chen et al. (2012) to synthesize silicon core hollow carbon shell nanoparticles with controllable

pores between the silicon cores and the hollow carbon shells for the application in lithium ion batteries.

Several studies on the different synthesis techniques for hollow core-shell nanoparticles are listed in Table 2.1. Self assembly technique was employed using a gemini surfactant to synthesize hollow mesoporous silica nanoparticles for the application in drug delivery (Li et al. 2013). Ultrasonic irradiation method was also used to synthesize mesoporous silica in a short duration under basic environment (Vetrivel et al. 2010). Yolk/shell zirconium titanium oxide nanoparticles were synthesized by template directed solvothermal method with uniform pores for catalytic applications (Guan et al. 2013). Synthesis of hollow structured and nanosized silica particles using sacrificial PS template method was reported initially by Sandberg et al. (2013). Sacrificial template method is found to be advantageous compared to other methods, since desired morphology of hollow core-shell nanoparticles could be obtained by monitoring the parameters such as template size, template concentration, reaction time and temperature. Major techniques utilized for the removal of template were by dissolving in an appropriate solvent or calcination to evaporate the template.

Table 2.1 List of papers on synthesis of hollow core-shell nanoparticles

Sl. No.	Author	Core-shell Nanoparticles	Particle size (nm)	Synthesis technique	Application
1	Agrawal et al. (2008)	PS/Ta_2O_5	500	Sacrificial template	surface coatings, catalysts, drug delivery
2	Vetrivel et al. (2010)	Mesoporous silica	1μm	Ultrasonic irradiation	Catalysis
3	Gharibe et al. (2011)	ZnSe/Silica	30	Sol/gel	Catalyst, drug delivery
4	Song et al. (2012)	Au/Pt, Au/Pd	60-200	Galvanic displacement	Nanomedicine
5	Chen et al. (2012)	Silicon/Carbon	100	Solution growth	Li ion batteries
6	Guan et al.	zirconium	210	Solvothermal	Catalysis

		titanium oxide			
7	Li et al. (2013)	Hollow mesoporous silica	350	Self assembly	Drug delivery
8	Keshavarz and Ahmad (2013)	Al/Silica	-	Sol/gel	Petrochemical refinery
9	Sandberg et al. (2013)	Hollow silica nanospheres	180-900	Sacrificial template	Thermal insulation
10	Bo et al. (2013)	carbon nanocapsules/ silica	200	Template	Drug delivery
11	Kim et al. (2013)	Silver/silica	35-138	Electron beam irradiation system	-
12	Zhang et al. (2013)	Fe_2O_3 /SnO_2	300	Hydrothermal	Gas sensors
13	Kobayashi et al. (2013)	GdC/SiO_2 core-shell	50	Homogeneous precipitation	Drug delivery

Hollow core-shell nanoparticles were synthesized by using metals, inorganic materials and metal oxides. Metals used were silver, gold, aluminium and platinum nanoparticles. Metal oxides used were Fe_2O_3, SnO_2, Ta_2O_5, zirconium titanium oxide and silica. Inorganic materials used were ZnSe, GdC and carbon. Table 2.1 gives the list of researches on the usage of various materials during the synthesis of hollow core-shell nanoparticles. Among them, hollow core-shell silica nanoparticles are considered to be one of the best materials for targeted drug delivery applications. Since hollow core-shell structured silica nanoparticles were found to be nontoxic, highly biocompatible, mechanically stable and chemically inert (Ogi et al. 2014).

2.2 Hollow core-shell silica nanoparticles

Hollow silica nanostructures have made a notable impact in different research areas such as absorption, controlled drug delivery, bioimaging, optical coatings and catalysis. Their unique properties like high surface area and pore volume, ease of surface

functionalization, chemical stability and low toxicity provide a significant influence for their application in targeted drug delivery. However, there are limited numbers of researches for efficient, simple and economical synthetic techniques for the fabrication of HCSNs. One of the most common methods of synthesis of HCSNs is by using the sacrificial template method. Coating of the PS template could be easily achieved by the modified Stober method. Synthesis of monodispersed silica spheres by the Stober method involved hydrolysis and condensation of TEOS in the water-ethanol mixture using ammonia as a catalyst (Stober et al. 1968). The reactions occurring during the formation of silica nanoparticles are given below (Brinker 1988; Shin et al. 2010). Hydrolysis and condensation rates were found to depend on the pH of the medium.

Hydrolysis

$\equiv Si - OR + H_2O \leftrightarrow \equiv Si - OH + ROH$
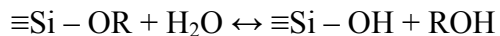
(i)   Alcohol condensation

$\equiv Si - OR + HO - Si \equiv \leftrightarrow \equiv Si - O - Si \equiv + ROH$
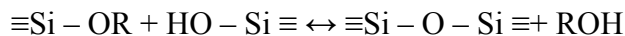
(ii)   Water condensation

$\equiv Si - OH + HO - Si \equiv \leftrightarrow \equiv Si - O - Si \equiv + H_2O$
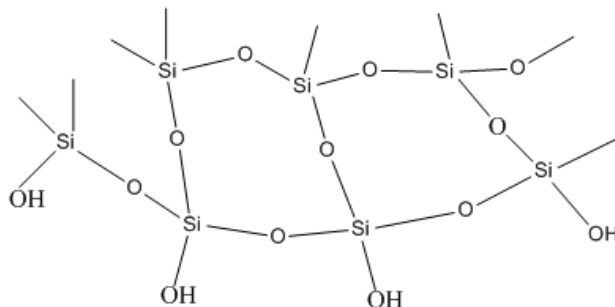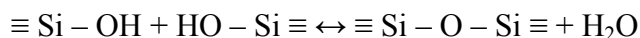
Figure 2.1 Silica network in the shell of HCSNs (Shin et al. 2010)

Stober method was altered by the use of polymeric template and cationic surfactant to synthesize nanometer or sub-micrometer sized hollow silica spheres (Ge et al. 2009; Nguyen et al. 2014). Various precursors of silica were used during the synthesis of HCSNs like tetramethoxysilane, tetraethoxysilane and colloidal silica particles (Lee et al. 2008; Yang et al. 2008; Zhang et al. 2009a). Facile synthesis of HCSNs by merging template method and Stober method resulted in the formation of HCSNs with tunable thickness and narrow pore sizes. Some of the important parameters considered during the synthesis of silica hollow core-shell nanoparticles are pH, morphology, zeta potential and template removal techniques which are discussed below.

The pH of medium played an important role in the synthesis of HCSNs. According to the Stober method, basic and dilute conditions were preferred for the synthesis of silica particles (Stober et al. 1968). It was evident that nearly no silica coating was occurred at pH below 10, since very less amount of residue was found after calcination at 600 ^{0}C. The low rate of hydrolysis of TEOS i.e. at pH ≤10 was not desirable for the coating of silica on the surface of PS. The rise in pH of the medium enhanced the hydrolysis rate of TEOS. Thus, at pH-11.3, silica coating was done smoothly and covered the PS surface. However, at very high pH, i.e. pH >12 lead to the heterogeneous nucleation of silica and formation of free solid silica particles. This condition was not advisable as the uniform coating of the silica particles on the PS surface did not occur. Rough surface features were exhibited by the HCSNs synthesized at pH>12. The possible reason could be due to the nucleation of multiple layers of silica particles on the PS surface. A higher rate of hydrolysis and condensation of silica encouraged rapid nucleation (Park et al. 2009).

Morphology of HCSNs was altered by tailoring the parameters such as concentration of silica precursor, concentration of catalyst-ammonia, reaction medium, sacrificial template, reaction time and reaction temperatures. HCSNs with different shell thicknesses were obtained by tuning the concentration of silica precursor. Thickness of the silica was increased by raising the concentration of silica precursor (Deng et al. 2006). Wall thickness was also affected by the quantity of the polymer template. There was a rise in

the concentration of micelles when the concentration of polymer increased. Thus, less deposition of silica on the surface of CTAB coated polymer template was observed (Zhou et al. 2014). Ammonia acted as a catalyst during the synthesis of silica in the Stober process. The rate of hydrolysis of TEOS was found to vary with the concentration of ammonia. At higher concentration of ammonia, PS particles found to dissolve. However, lower concentrations of ammonia had reduced the rate of hydrolysis of silica precursor (Yuan et al. 2010).

The morphology of HCSNs was influenced by the quantity of water present during the synthesis. It was observed that the quantity of water had control over the rate of hydrolysis and condensation of silica precursor. This would lead to the rapid formation of silica coating of the template (Yuan et al. 2008). PS nanoparticles were used as sacrificial templates and CTAB as the shell structure directing agent by Ge et al. (2009) . CTAB acted as a surfactant that binds the negatively charged PS and the silica micelles together. CTAB is a cationic surfactant which produces CTA^+ and Br^- ions. Negatively charged PS nanoparticles were coated with CTA^+ ions leading to the formation of positive charge on the surface of PS nanoparticles which attracted the negatively charged silica micelles by electrostatic force (Ge et al. 2009).

Silica walls synthesized by the Stober method were found to be porous (Wu et al. 2006). The pores were formed during the calcination of silica coated polymer in the presence of air. Structures of pores were altered by altering the reaction temperature. Calcination of silica coated PS-methyl acrylic acid template prepared at room temperature produced HCSNs with micropores. However, HCSNs synthesized by ageing them at 150 ^{0}C, gave rise to mesopores with an average pore size of 15 nm (Ge et al. 2009). Lower rate of reaction resulted in the polycondensation of the silica coating and formation of loosely structured silica shells and formation of micropores. Mesopores were formed in the second case, since the rise in reaction temperature accelerated the polycondensation reaction with the silica micelles. In the latter case, raising the reaction temperature in the silica coating process promoted the polycondensation reaction among the siliceous

micelles coated on the latex surfaces, resulting in the formation of silica shells with a dense structure (Ge et al. 2009). Pore diameters were found to enhance from 12 nm to 18 nm with an increase in the number of polymer blocks (Niu et al. 2010). Lee et al. (2008) reported that the increasing concentration of trimethyl ammonium functional groups had altered the structure of mesoporous silica from two dimensional pores to a worm like structure. BET isotherms revealed that the pores present in the shells of the HCSNs synthesized by using carboxylic acid functionalized templates had both micropores and mesopores. But those prepared by using the sulfonated latex templates had mesopores (Liu et al. 2011).

Surface areas of HCSNs were analyzed by the Brunauer-Emmett-Teller (BET) analysis by using the N_2 adsorption/desorption data using the IUPAC technical report (Thommes et al. 2015). Mesoporous structure of the silica shell was confirmed by analyzing the specific surface area of silica particles (Chen et al. 2013). High surface area of mesoporous silica nanoparticles is preferable for several applications. Large surface area enabled high volume for drug loading in the targeted drug delivery (She et al. 2015). The specific surface area of SiO_2 spheres were found to decrease with the increase in the diameter of the sacrificial templates (Liu et al. 2012). There was also an increase in the surface area with increase in amount of water added (Liu and Zhao 2016). Venkatathri (2007) reported the effect of catalyst on the surface area of hollow mesoporous silica. There was increase in the specific surface area of silica with increase in the catalyst size. The mesoporous silica nanoparticles with large specific surface area (1379 m^2/g) were obtained using Na_2SiO_3 precursor compared to that of TEOS precursor (848 m^2/g). This phenomenon occurred because of the presence of inorganic salts which had increased the total number of the surfactant micelles which in turn increased the pore diameters of mesoporous silica (Tang et al. 2012).

The particle size increased with increase in the reaction time as more number of silica particles were deposited forming multiple layers of silica on the surface of polymer template and thus, the thickness of the silica shell also increased (Ding et al. 2004). The

particle size of the HCSNs showed the dependence on the particle size of the template and the amount of copolymer. It was observed that enhancing the amount of copolymer, particle size of hollow mesoporous silica increased. Since the increased amount of copolymer led to the increase in number of micelles and there was less silica deposition on the polymer template (Zhou et al. 2014). In the literature, it has been reported that zeta potential is function of the comonomer (3-(trimethoxysilyl)-propyl methacrylate (MPS)) concentration, since silanol groups increased as the MPS quantity increased (Tissot et al. 2002).

Micelles of silica had a negative surface charge which was not useful while coating negatively charged PS. Thus, organo-silica precursors were introduced to decrease the negative surface charge of silica, but it did not affect well. Precursors also influenced the hydrophilic nature of the generated surfaces. Silica obtained by the Stober method was found to be hydrophilic due to the existence of -OH groups on the surface. Usage of organo-silica precursors resulted in reduced -OH groups and hydrocarbon groups on the surface. Thus, the HCSNs surface became hydrophobic and enhanced the interfacial tension leading to higher critical seed size for particles. The silica hollow particles had higher mechanical stability to withstand heat treatment and ultrasonication (Deng et al. 2015).

Removal of the sacrificial template is one of the major steps during the synthesis of HCSNs. The methods used for template removal are by dissolving them in a suitable solvent or calcination at elevated temperature. PS templates were dissolved in an aqueous ammoniacal alcohol solution (at 50 ^{0}C) during the synthesis of hollow SiO_2 nanoparticles by Deng et al. (2006). Liu et al. (2012) reported the removal of the CTAB, PS and PS-methyl acrylic acid templates by calcination. Silica coated templates were heated from room temperature to 550 ^{0}C with 1 ^{0}C per minute for 4 hours under the atmospheric condition for the oxidation of organic cores. The calcination methods were found to be advantageous, since dissolution in a solvent would affect the mesoporous hollow

structure of SiO$_2$ nanoparticles. The selection of suitable solvent was also found to be a tedious process.

Several polymer sacrificial templates used in the literature are PS, SiOH functionalized PS, polystyrene-b-poly (acrylic acid), sulfuric acid and carboxylic acid functionalized PS and methyl acrylic acid (Table 2.2). Among them, PS is a versatile template using which morphology of silica shell could be improved by monitoring the surface charge properties.

Table 2.2 List of papers on synthesis of HCSNs by sacrificial template method

Sl. No.	Author (year)	Polymer template	Surfactant	Particle size (nm)
1	Tissot et al. (2002)	SiOH functionalized PS	Sodium dedecyl sulfonate (SDS)	105-132
2	Deng et al. (2006)	PS	-	260
3	Wu et al. (2007)	PS	Polyvinyl pyrrolidone (PVP)	260
4	Lee et al. (2008)		CTAB	100
5	Ge et al. (2009)	PS methyl acrylic acid	CTAB	350
6	Yuan et al. (2010)	PS	-	40
7	Niu et al. (2010)	polystyrene-b-poly (acrylic acid)	CTAB	250
8	Liu et al. (2011)	Sulfuric acid and carboxylic acid functionalized PS	CTAB	360-650
9	Liu et al. (2012)	PS and PS-methyl acrylic acid	CTAB	407
10	Chen et al. (2013)	PS-block-poly (acrylic acid)	CTAB	300
11	Nguyen et al. (2014)	PSS, PAA	MTMS	100-270
12	Zhou et al. (2014)	PS-b-poly (acrylic acid)	CTAB	230-290

13	She et al. (2015)	Eudragit nanoparticles	-	120
14	Deng et al. (2015)	PS	-	284
15	Liu and Zhao (2016)	Dodecyl amine	-	1 μm
16	Wu et al. (2018)	poly(N-isopropyl acrylamide)-b-poly(4-vinyl-pyridine)	-	510
17	Dobo et al. (2017)	PS	CTAB	500
18	Peng et al. (2019)	PS	CTAB	157-245

2.3 PS template synthesis

The sacrificial template method for producing monodispersed hollow silica with mesoporous shell structure is associated with usage of polymer templates. PS nanoparticles are considered to be superior amongst the other templates as they could be tuned to different sizes (from several nm to μm) producing monodispersed particles. They also have good shelf life and could be synthesized by simple techniques. Chemical structures of styrene and PS are given in Figure 2.2.
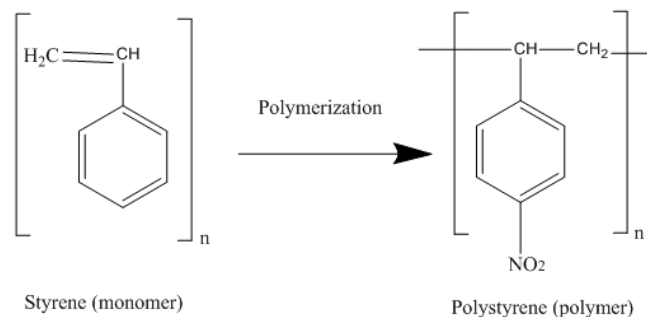
Figure 2.2 Styrene polymerization (Edewele 2010)

PS nanoparticles were generally synthesized by dispersion polymerization, emulsion polymerization and soap-free polymerization (Milosevic et al. 2009; Yamamoto et al. 2006). Dispersion polymerization is a technique where polymerization of monomer

occurs in the presence of polymeric stabilizer soluble in the reaction medium. The monomer and stabilizer should be soluble in the reaction medium except for the newly formed polymer. But PS synthesized by this method were found to be polydispersed and in micron size (Lei and Zhou 2014). The soap-free polymerization does not involve the usage of surfactants and produces polymer particles with minimal contaminants. The nucleation and mechanism of polymer growth are studied by using soap-free polymerization. However, there is less control over the particle size of the resulting polymer produced (Yamamoto et al. 2006).
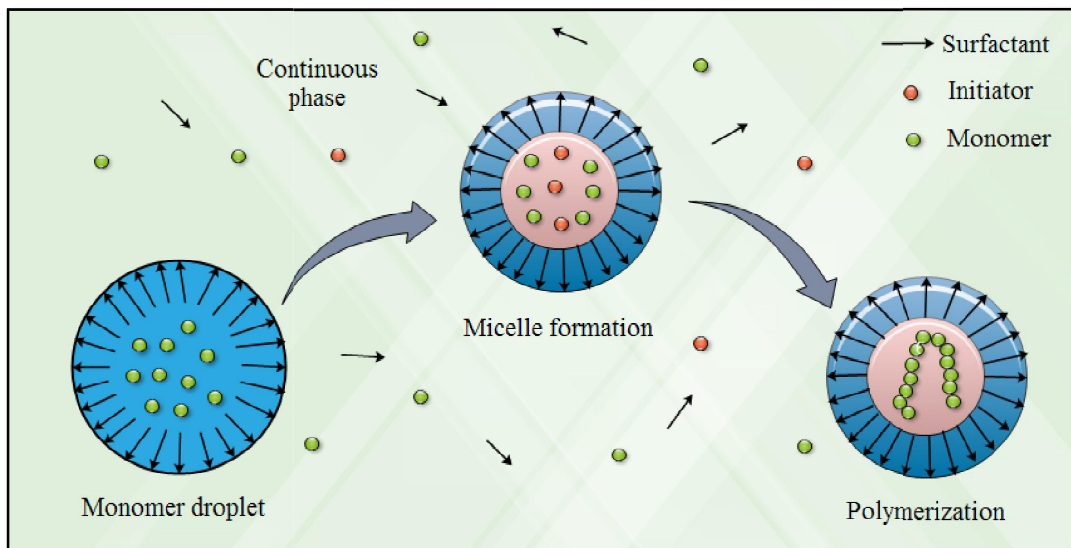
Figure 2.3 Mechanism of emulsion polymerization (Bonham et al. 2014)

Emulsion polymerization consists of oil in water emulsion, where monomer droplets are emulsified in water, which is the continuous phase. Polymerization occurs impulsively in the latex particles during the initial minutes of the emulsion polymerization. Agglomerations of particles are reduced by the usage of a suitable surfactant. Surfactants surround the particles and electrostatic repulsion between the particles further avoided the coagulation. The advantages of emulsion polymerization process are - it is possible to obtain controlled size and desired molecular weight for PS (Milosevic et al. 2009).

The surfactants also aid in lowering the surface tension of the monomer droplets by forming a network around them. But, when the surfactant concentrations exceed the permissible limits, molecular droplets were referred as micelles. Surfactants are categorized as anionic, cationic and non-ionic surfactants. During the formation of micelles, surfactants aggregate, such that hydrophilic groups face the outer surface and hydrocarbon groups which are hydrophobic nature, face toward inside (Gowariker et al. 2015). The pictorial representation of the emulsion polymerization system is shown in Figure 2.3.

The particle size of the PS was dependent on the parameters such as initiator concentration, surfactant concentration, reaction time and temperature. There was growth in PS particle size with the increase in the initiator concentration as a result of the large number of nuclei formation. But particle size reduced with the rise in concentration of surfactant such as PVP. The surfactant gave a colloidal stability for the polymer nuclei formed and helped to avoid agglomerations resulting in the growth of polymer (Sandberg et al. 2013; Yun et al. 2010). It was found that particles were of random shape during the initial hour with a wide size range. After 2 hours, particles with a narrow size and spherical shape were obtained. The rapid growth of particles was observed during the initial stages of polymerization (1- 3 hours). However, growth rate reached constant value after 6 hours. PS particle sizes showed an increase when the reactant concentrations increased. A bimodal size distribution was seen at higher concentrations (Yun et al. 2010).

Metal stearates were used to provide a positive surface charge on the surface of PS. The stearate groups had hydrophobic nature which resulted in the increase of osmotic pressure for monomer droplets. Higher osmotic pressure intercepted the diffusing of monomer molecules from the monomer droplet leading to the formation of monodispersed PS nanoparticles. This phenomenon improved emulsion stability and reduced the Ostwald ripening process. Zeta potential of PS nanoparticles was found to be 60-80 mV (Kim et al. 2008).

PS particles with cross-linked structure had comparatively high hydrophobic surface. PS surface showed a negative surface charge when hydrophilic comonomer sodium tetraborate was employed during the synthesis of PS. Since the sulfate groups on the surface were positioned towards outside facing the water was confirmed to be hydrophilic (Kim et al. 2009). In a study, PS particle size was monitored by regulating the PVP/styrene weight ratio. PVP was used as the surfactant to bind the silica nanoparticles on the surface of PS. At a lower concentration of PVP, buffering effect was not sufficient to coat the silica particles. PVP concentration was maintained such that the negative surface charge of PS was masked resulting in coating of the negatively charged silica particles (Sandberg et al. 2013). Table 2.3 gives a list of papers discussing about PS synthesis.

The reaction temperature is found to be an important factor during polymerization which decides the morphology of resulting particles. Initiators were found to decompose above 60 ^{0}C and produce free radicals aiding in initiation of the polymerization reactions. When the initiator was added at 70 ^{0}C, number of free radicals was produced rapidly leading to the formation of several polymer nuclei. Thus, the particle sizes of PS nanoparticles were comparatively less. However, when the initiator was added at room temperature resulted in PS particles with higher particle size. Formation of polydispersed PS particles was found at high reaction temperatures above 70 ^{0}C. Maintaining an optimum temperature for polymerization reaction determined particle size and morphology (Du and He 2008; Yoon et al. 2014). Table 2.3 gives the list of papers on PS synthesis.

Table 2.3 List of papers on PS synthesis

Sl. No.	Author (year)	Method used	Particle size (nm)	Surfactant	Application
1	Antonietti et al. (1991)	Emulsion polymerization	20-120	Cetyl trimethyl ammonium chloride	Medical

				(CTMA)	
2	Bourgeat-Lami and Lang (1998)	Dispersion polymerization	140-300	PVP	Silica coating on PS
3	Ding et al. (2004)	Dispersion polymerization	100	PVP	Hollow silica synthesis
4	Yamamoto et al. (2006)	Soap free emulsion polymerization	100-380	-	
5	Yoon et al. (2006)	Dispersion polymerization	330-500	-	Hollow silica synthesis
6	Yan et al. (2007)	Emulsion polymerization	1 μm	PVP	SiCN synthesis
7	Kim et al. (2008)	Polymerization with metal stearates	75-480	-	Biotechnology
8	Kim et al. (2009)	Copolymerization with acrylic acid and sodium tetraborate	93-260	Sodium dodecyl sulfonate (SDS)	Immunoassay
9	Guo et al. (2009)	Copolymerization	88-233	acryloyl chloride	TiO_2 core shell particles
10	Yun et al. (2010)	Emulsion polymerization	100-400	PVP	Inks, coatings
11	Sandberg et al. (2013)	Emulsion polymerization	180-900	PVP	Hollow silica nanospheres
12	Lei and Zhou (2014)	Dispersion polymerization	2-4 μm	PVP K-30	Biomedical
13	Yoon et al. (2014)	Emulsion polymerization	1.2-5 μm	PVP K-30	Biomedical
14	Gorsd et al. (2015)	Emulsion polymerization	2-3 μm	PVP	Hollow spherical materials
15	Aimable et al. (2017)	Emulsion polymerization	370	-	Ceramic field
16	Soleimani and Mohammadi (2018)	Emulsion polymerization	-	SDS	NiO composite synthesis

2.4 Functionalization of PS template

Studies on functionalized PS template would help to synthesize monodispersed spherical silica hollow core-shell nanoparticles with desired morphology (such as thickness and pore size). Functionalized PS templates have several advantages over the PS template and they were comparatively less studied. The application of functionalized PS nanoparticles as the sacrificial template for the synthesis of HCSNs needed much attention. PS may be functionalized with several functional groups such as carboxyl, amino, sulfonate and nitro. A list of approaches on functionalizing PS is given in Table 2.4.

The thickness of silica shell was influenced by the acidity of acidic functional group. Shell thickness showed an increase by 3 times while sulfonated PS- methyl acrylic acid was used as a template, compared to that of silica synthesized by using PS- methyl acrylic acid (Liu et al. 2011). Sulfonation of PS was done using gaseous SO_3 and fuming sulfuric acid. PS particles were allowed to react with the sulfonating environment for a known interval of time. The concentration of sulfuric acid decided the yield of sulfonation on the surface of PS (Kucera and Jancar 1996). Thus, the polarity on the surface of the PS particle was increased. Liu et al. (2011) found that the particle sizes of the PS methyl acrylic acid latex spheres were less than that of the PS spheres. However, the sulfonation of the PS-methyl acrylic acid spheres did not affect their size and morphology. Hollow silica spheres synthesized using PS template produced more broken particles compared to that of sulfonated PS-methyl acrylic acid templates, after heat treatment procedures. Yang et al. (2005) achieved sulfonation of PS particles with concentrated sulfuric acid. Sulfonation was carried out at 40 ^{0}C in a magnetic stirrer by introducing sulfonate group on the surface of PS.

Table 2.4 List of papers on functionalization of PS

Sl. No.	Author (Year)	Functional group	Method used	Particle size (nm)	Application
1	Philippides et al. (1993)	$-NO_2$	Nitration of PS in N,N'- dimethyl formamide and nitric acid/sulfuric acid	-	-
2	Kucera and Jancar (1996)	$-SO_3H$	Homogenous and heterogeneous sulfonation	-	-
3	Holzapfel et al. (2005)	$-COOH$, $-NH_2$	Emulsion copolymerization	97-175	Drug delivery
4	Brijmohan et al. (2005)	$-SO_3H$	Emulsifier free emulsion polymerization	40-80	Catalysis
5	Yang et al. (2005)	$-SO_3H$	Sulfonation using sulfuric acid	1µm	Polyaniline synthesis
6	Ge et al. (2009)	$-COOH$	Emulsion copolymerization	350	Drug delivery
7	Liu et al. (2011)	$-COOH$ $-SO_3H$	Emulsion copolymerization	360-650	Drug delivery
8	Shultsev (2013)	$-NO_2$	4-nitro styrene preparation	-	-
9	Huang et al. (2018)	$-SO_3H$	Sulfonation using sulfuric acid	2 µm	Super capacitor

The particle size of polymer and the number of functional groups on the surface of the polymer were directed by the functional comonomers during PS functionalization with carboxyl and amino group. When the concentration of comonomer- acrylic acid was increased, there was increase in the particle size of the polymer and the polymerization was promoted at low pH. However, increasing the concentration of amino group comonomer (2-aminoethyl methacrylate hydrochloride) did not aid in polymer growth. This phenomenon occurred since it acted as a surfactant and gave electrostatic stabilization for the micelles formed. It was also observed that the number of carboxyl

groups was higher compared to the number of amino groups in their respective polymers (Holzapfel et al. 2005). Cross-linked PS particles with broad size distribution were obtained by employing sodium styrene sulfonate as a stabilizing comonomer and divinylbenzene as a cross-linker. The wider size distribution was due to the dual nucleation mechanism as a consequence of more number of surface active agents (Brijmohan et al. 2005).

Usage of double electrolyte templates such as polystyrene sulfonate acid sodium salt (PSS) and polyacrylic acid (PAA) for the synthesis of HCSNs was studied by Nguyen et al. (2014). Formation of uniform silica nanoparticles was achieved by using double electrolytes (PSS and PAA). PAA helped in monitoring the pH of the medium and PSS allowed the synthesis of hollow structured silica particles. Agglomeration of silica formed was successfully avoided by employing methyltrimethoxysilane. Ethanol was used as the solvent which aided in creation of micelles which further lead to the formation of good quality hollow structure. Samples were washed with base to partially dissolve silica cluster and to form porous structure.

Nitro functionalization of PS particles was carried out using a nitrating mixture consisting of nitric acid and sulfuric acid mixture in N,N'- dimethylformamide medium (Philippides et al. 1993). A study on D,L-1-(4-nitrophenyl)ethanol interaction with thionyl chloride and phosphorus oxide and upgrading of the known method of 4-nitrostyrene preparation via the treatment of 2-(4-nitrophenyl)ethyl nitrate with alkoxy anion done by Shultsev (2013). The interaction of D,L-1- (4-nitrophenyl)ethanol and P_4O_{10} in toluene was influenced by the solution concentration and process of reagent insertion. Synthesis of 4-Nitrostyrene was carried out by adding P_4O_{10} to dilute D,L-1-(4-nitrophenyl)ethanol followed by a reflux. The method of synthesis of 4-nitrostyrene through breakage of 2-(4-nitrophenyl)ethyl nitrate and alkoxy anion was updated.

2.5 Application in drug delivery

Spherical nanoparticles with desirable hollow interior space have found their major applications in the field of targeted drug delivery working as a drug carrier. HCSNs are found to be suitable to perform as a drug delivery vector, due to their characteristic features. Factors influencing the drug release studies are pH of the release medium, temperature and morphology of the nanocarrier (thickness of the shell, pore size, surface area and particle size).

Tuning the shell thickness of silica is a governing factor in the targeted drug delivery studies. The drug entrapment efficiency was found highest for the silica particles with the highest shell thickness (Mohamed El-Toni et al. 2012). The drug release rate was found to reduce with the increase in the thickness of silica shell. The loaded drug molecules diffuse out easily to the medium when the thickness of the shell was comparatively less and there was shorter meso-channel length (Jiao et al. 2012). Drug release from the HCSNs showed a reduction for the samples with the lower surface area. However, the HCSNs samples with large surface area resulted in the rapid release of drug (Mohamed El-Toni et al. 2012).

The effect of particle size of mesoporous silica nanoparticles on targeted drug delivery was investigated by Bouchoucha et al. (2016). Silica nanoparticles <50 nm had better drug delivery performances compared to those particles with higher particle size. Silica nanoparticles ~50 nm size showed higher accumulation in the tumor site. When the drug loaded nanocarriers were given through intravenous injection, different sizes of nanoparticles were spread across the liver, spleen, lung, kidney and heart. It was seen that, number of particles in the spleen and liver increased with rise in particle size from 80-200 nm after injection. However, the smaller sized particles had longer blood circulation duration. The excretion through urine began to increase with an increase in the particle sizes of mesoporous silica nanoparticles (He et al. 2011; Tang et al. 2012).

The drug delivery rate also showed a dependence on the pore size of silica nanoparticles. Synthesis of hollow mesoporous silica nanoparticles with tunable pores was a boon for the controlled release of drug (Slowing et al. 2008). There was a decrease in the drug release with reduction in the pore size. It was also found that smaller sized pores stabilized the drugs from hydrolysis and diffusing out from the carrier very soon (Kwon et al. 2013). Ethylcellulose membrane coated mesoporous silica nanoparticles were synthesized while PVP was used as a pore former by Hacene et al. (2016). They reported the increase in drug release rate with increasing pore former and decreasing coating. The osmolality of the medium was altered using NaCl at different concentrations. The initial burst release of the drug was proportional to the average pore size in mesoporous silica nanoparticles (Mitran et al. 2016). Jiao et al. (2012) observed that a major part of the loaded drug was stored in the hollow core and very less amount of drug was found in the pores of the silica shell. The drug selected for the study was loaded on the HCSNs nanocarrier by dispersing them in the solution of drug at a known concentration.

Doxorubicin is one of the majorly used drugs in cancer treatments. Doxorubicin is used in the treatment of various cancers such as bladder, breast, ovarian and lung. Doxorubicin acts on the DNA and hindered the replication, transcription and damages the DNA units (Denard et al. 2012). The structural formula of doxorubicin ($C_{27}H_{29}NO_{11}$) is given below (Figure 2.4).
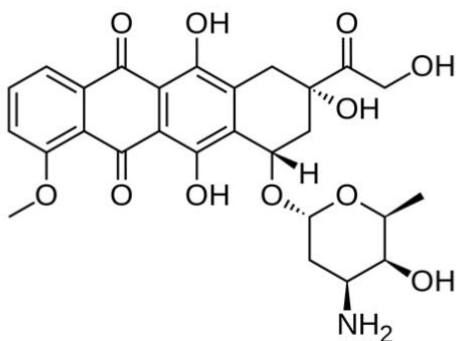
Figure 2.4 Chemical structure of doxorubicin (Zhao et al. 2018)

The pH of the phosphate buffer release medium affected the solubility of the doxorubicin in the medium. Doxorubicin solubility was comparatively high at lower pH (<7). However, at higher pH values above 8, doxorubicin release was significantly reduced. The tumor microenvironment studies revealed that the pH of the cancer cells was found to be lower (<7) than the pH of the healthy tissues (~7.4). Thus, doxorubicin drug action in destroying them was found to be more effective on cancer cells compared to other cells (Danhier et al. 2010; He and Shi 2011; Jiao et al. 2012). The pH responsive mesoporous silica nanoparticles were designed by introducing positive charges on silica structure using trimethyl amine. Thus, the anionic drug molecules adsorbed on the mesoporous silica nanoparticles easily at lower pH values (Lee et al. 2008).

In vitro cytotoxicity assays were done to judge the potential application of nanocarriers in drug delivery. The cell cytotoxicities produced by the silica nanoparticles and drug loaded nanoparticles were studied on cancer cells and normal cells. The cytotoxicity results were represented in the form of % cell viability versus concentration of nanoparticles. Cytotoxicity caused by the hollow mesoporous silica nanoparticles was negligible on cancer cells. However, drug loaded silica samples achieved successful destruction of cancer cells (>70%) (Balakrishnan et al. 2013; Jiao et al. 2012).

2.6 Kinetic models for drug delivery

Study of the mechanism of drug delivery with the experimental drug release study data allows the development of a successful targeted drug delivery system. Understanding the process of mass transport occurring during the loading and release of drug to the targeted site plays a significant job during the application of HCSNs in cancer therapy. The experimental data from the release studies are fitted in various diffusion models. Interpretation of the precise model for the controlled release data would help to foresee the possible outcomes of the release studies and to design new experiments to overcome the limitations whenever necessary. A number of studies focused on modeling the drug release data and analyzing the kinetics by considering the physical parameters like diffusion coefficients, release time and initial concentrations. The majority of the models

are based on the Fick's law of diffusion with suitable boundary conditions (Wang and Edwards 2016). There are several models for drug release kinetics which are discussed below such as zero order, first order and Higuchi model.

Zero order model:

The zero order model is based on the principle that the rate of drug release is independent of the concentration of drug released. The model equation is represented below.

$$Q_t = Q_0 + k_0 \times t \qquad (1)$$

Where, Q_t is the quantity of drug released at time t, Q_0 is the initial amount of drug in the medium and k_0 is the rate constant for the zero order model. k_0 was determined from the slope of the plot of % cumulative drug release versus time.

First order model:

The first order kinetic model describes the release from the system where the release rate is concentration dependent and can be expressed as follows:

$$\log C_t = \log C_0 - k_1 \times t / 2.303 \qquad (2)$$

Where, C_t is the concentration of drug released in time t, C_0 is the initial concentration of drug remaining in the silica nanoparticles and k_1 is the first order rate constant. The value of k_1 was calculated from the slope of the linear plot of log cumulative % drug release versus time.

Higuchi model:

The Higuchi model gives the drug release from an insoluble matrix as the square root of time based on Fickian diffusion. In general, the Higuchi model can be expressed as:

$$Q_t = k_H \times t^{0.5} \qquad (3)$$

Where, k_H is the Higuchi constant. The value of k_H was obtained from the slope of the linear plot of cumulative % drug release versus the square root of time.

2.7 SPIONs in drug delivery

The SPIONs have attracted attention in the medical field because of their alternating magnetic properties at the nanoscale. Nanosized maghemite and magnetite are ferrimagnetic in nature. They are used in various biomedical applications like targeted drug delivery, tissue engineering, local hyperthermia, nuclear magnetic resonance imaging and magnetic separation. Some of the major features of them include biocompatibility, nontoxicity, high magnetic moments, superparamagnetism and economical synthesis (Kopanja et al. 2016; Wu et al. 2008).

SPIONs can be synthesized by top-down (mechanical attrition) or bottom-up (chemical synthesis) approaches. However, chemical methods of synthesis were found better to produce SPIONs with uniform size and composition (Knezevic et al. 2013). Chen et al. (2010) reported the fabrication and usage of nanocapsules with Fe_3O_4 nanocrystals as the cores. Tunable hollow core-shell nanoparticles were synthesized and used as MRI contrast agents and drug delivery vectors. Nanoparticles with multifunctional moieties were synthesized by assembling Fe_3O_4 nanocrystals on mesoporous silica nanoparticles. Superparamagnetic nature enabled the application of iron oxide composite with mesoporous silica in fluorescence imaging and MRI as well as drug delivery carriers. The composite nanoparticles loaded with cancer treatment drug were injected into the tumor site (Lee et al. 2010).

In a research, mesoporous silica composited with Fe_3O_4 nanoparticles was synthesized using PS templates. The polymer core was removed by dissolution in toluene and heating at low temperature. However, iron oxide nanoparticles retained their superparamagnetic properties as analyzed in superconducting quantum interference device (SQUID) magnetometer (Wu et al. 2007). Nalbandian et al. (2016) reported synthesis of Fe_3O_4 nanoparticles by chemical co-precipitation method and coated with silica using TEOS precursor. The plots of magnetic moment versus magnetic field obtained from SQUID, confirmed the superparamagnetic behavior of iron oxide nanoparticles. Since the magnetization curve did not show hysteresis and passed through the origin which

indicated the absence of magnetization in the absence of external magnetic field at 300 K. Vibrating sample magnetometer (VSM) analysis was also used to determine the superparamagnetic property of iron oxide nanoparticles. Magnetic properties of the silica-iron oxide composites were tested with VSM showed superparamagnetic features (Kopanja et al. 2016).

2.8 Scope and objectives of the work

Based on the detailed literature survey, it is clear that there is a huge need for stable and versatile drug delivery vector to combat life threatening diseases like cancer. Though the literature shows that, lot of research is going on in the development of drug delivery vector; the major focus is on the mesoporous nanoparticles rather than hollow core-shell nanoparticle due to ease of synthesis techniques. Few literatures discuses about the disadvantages of mesoporous drug delivery vector, research on hollow core-shell drug delivery vectors is limited.

Few literatures discuss about the application of hollow core-shell nanoparticles as drug delivery vectors. However, the possibility of tuning the characteristics of core-shell drug delivery vectors is less studied. Tuning the properties of HCSNs could be a huge turning point in the drug delivery research, which can address many issues in the field of drug delivery system. Keeping this research gap in mind, the present research topic is framed. HCSNs morphology can be tuned as required by using the sacrificial PS template method. Functionalization of PS with different functional groups is proposed in order to alter the morphology of silica nanoparticles. Further, to achieve the targeted drug delivery system, SPION embedded HCSNs were synthesized and characterized. To achieve the above hypothesis, following objectives are framed and executed.

1. Synthesis and characterization of PS nanoparticles by emulsion polymerization
   - Studies on the effect of operating variables (initiator, monomer, surfactant, temperature)
   - Characterization with SEM, FTIR, particle size and TGA

2. Functionalization of PS nanoparticles with -SO$_3$H and -NO$_2$ groups

   ■ Characterization with SEM, zeta potential, FTIR and TGA

3. Synthesis and characterization of HCSNs using sacrificial PS template and functionalized PS (sulfonated PS, nitrated PS) templates

   ■ Studies on the effect of parameters such as concentration of ammonia, concentration of CTAB and ratio of template/TEOS on the morphology of HCSNs

   ■ Characterization with SEM/TEM, FTIR, XRD, TGA and BET

4. Synthesis and characterization of SPION embedded HCSNs

   ■ Studies on the effect of concentration of SPION on the morphology of SPION embedded HCSNs

   ■ Characterization with SEM, TEM, FTIR and BET

5. Studies on release kinetics and development of release kinetic model using model drug release studies

6. Cytotoxicity studies of HCSNs and SPION embedded HCSNs

2.9 Outline of the thesis

The present research work is divided into the following chapters.

Chapter 1, Introduction: This chapter deals with the background of research, the need for the study and the importance of the present study. It starts with an introduction about the features of the targeted drug delivery system and the application of HCSNs as drug delivery vector.

Chapter 2, Literature Review: This chapter summarizes the detailed literature review carried out during the current study and research gaps are highlighted in the existing literature reports. Based on the literature review, the scope and objectives of the work are planned and presented at the end of this chapter.

Chapter 3, Materials and Methods: This chapter lists the materials used and their purity. The experimental procedures followed to achieve the stated objectives during the research are also explained in this chapter.

Chapter 4, Results and discussion: This chapter consists of four parts:

Part I deals with the results and discussion on the HCSNs synthesis by using sacrificial PS template and application in targeted drug delivery. Synthesis and optimization of PS template, synthesis and optimization of HCSNs using PS template, drug delivery and cytotoxicity studies are discussed in this section.

Part II involves HCSNs synthesis from the sulfonated PS template and application in targeted drug delivery. Synthesis of sulfonated PS template, application of sulfonated PS in the synthesis of HCSNs, drug delivery and cytotoxicity studies are included in this part.

Part III deals with the HCSNs synthesis by using a sacrificial nitrated PS template and application in targeted drug delivery. Synthesis of nitrated PS template, synthesis of HCSNs using nitrated PS, drug delivery and cytotoxicity studies are discussed in this part.

Part IV includes the synthesis of SPION embedded HCSNs and application in targeted drug delivery. Synthesis of SPION embedded HCSNs, radiofrequency studies, drug

delivery and cytotoxicity studies are included in this section. Results are presented in the form of tables and figures wherever necessary.

Chapter 5, Summary and Conclusions: Summary and conclusions derived based on the study along with the future scope for research are presented in this chapter.

CHAPTER 3

3. MATERIALS AND METHODS

3.1 Materials

The chemicals used in the present research work were styrene (99%), polyvinyl pyrrolidone (PVP, molecular weight-40,000), TEOS (98%), doxorubicin and SPION (98%) which were purchased from Sigma Aldrich. Potassium persulfate (KPS, 98%), CTAB (98%), sulfuric acid (98%) and nitric acid (69%) were procured from Loba Chemie. Aqueous ammonia solution (25%) and ethanol were purchased from Spectrum Chemicals and Changshu Hongsheng Fine Chemical Co. respectively. All the chemicals were used without further purification. Millipore water was used throughout the experiments.

3.2 Synthesis of PS template

Styrene was polymerized by emulsion polymerization method in water using KPS as an initiator and PVP as a stabilizer. KPS and PVP were dissolved in water separately. 43.4 mmols of styrene was taken in a 100 mL round bottom flask and then PVP solution was added while 1:9 volume ratio of styrene to water was maintained. The reaction mixture was gradually heated to 70 ^{0}C and the initiator (KPS) was added. The solution was stirred at 70 ^{0}C for 24 hours in the presence of nitrogen. The reaction mixture was cooled to the room temperature before separation of PS. Centrifugation of reaction mixture was carried out at 13,000 rpm for 20 minutes to separate PS particles. The resultant product was subsequently washed with water to remove unreacted chemicals. Samples were freeze dried to eliminate the retained moisture. The effect of process variables such as initiator concentration, stabilizer concentration, reaction time and reaction temperatures were analyzed and optimized by using one variable at a time method (OVAT). Experimental details by varying reaction parameters are tabulated in Appendix AI.1.

3.3 Sulfonation of PS

1 g of PS was dispersed in 8 mL of known concentration of sulfuric acid. The sulfonation reaction was carried out at room temperature under continuous stirring for 2 hours. The sulfuric acid concentration was varied as 1 M, 5 M, 10 M and 17.9 M. Ethanol was added in excess to the reaction mixture to resume the sulfonation reaction and continued to stir for another 15 minutes. The sulfonated PS was separated by centrifugation at 10,000 rpm for 10 minutes and washed five times with water. Thus, obtained samples were lyophilized to remove water.

3.4 Nitration of PS

The nitration of synthesized PS nanoparticles was carried out using nitric acid and sulfuric acid. 1g of PS was dispersed in a mixture of 15.14 M nitric acid and 17.9 M sulfuric acid mixed at different volume ratios such as 2:3, 3:2 and 1:2. The reaction mixture was stirred in a magnetic stirrer for 2 hours. The nitration reaction was resumed by adding distilled water in excess to the reaction mixture and continued to stir for another 30 minutes. Resulting nitrated PS nanoparticles were obtained by centrifugation (13,000 rpm for 15 minutes) and washed in distilled water. Nitrated PS samples were dried in a lyophilizer to remove moisture.

3.5 Synthesis of HCSNs

1 g of synthesized polymer template was dispersed uniformly by ultrasonication for 30 minutes in water-ethanol mixture. 5 % CTAB solution was added to the mixture and stirred in a magnetic stirrer for 2 hours. Ammonia was added drop wise to the reaction mixture, followed by the addition of TEOS-ethanol mixture (TEOS mixed with an equal amount of ethanol) and continued to stir for 4 hours at room temperature. The resulting suspension was aged at room temperature for 24 hours. The precipitate was separated by centrifugation at 10,000 rpm for 10 minutes and washed five times with water.
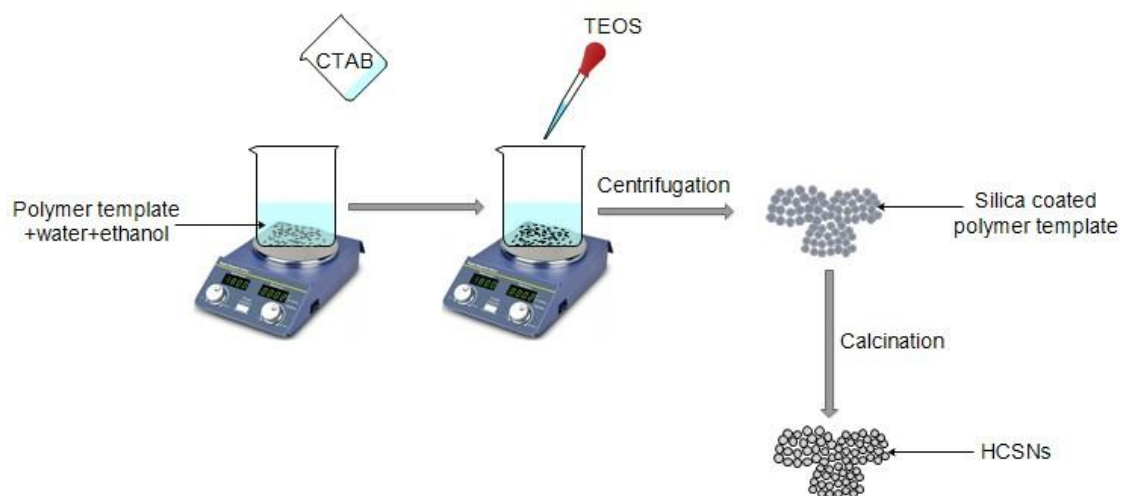
Figure 3.1 Schematic representation of synthesis of HCSNs using polymer templates

Samples obtained were freeze dried to remove moisture content and the obtained silica coated nanoparticles were calcined at 550 ^{0}C for 4 hours at a heating rate of 1 ^{0}C/min to remove polymer core. HCSNs were synthesized by using different templates such as PS, sulfonated PS and nitrated PS. A schematic of the synthesis of HCSNs using polymer templates is represented in Figure 3.1. Parameters like volume ratio of water/ethanol, the concentration of ammonia, concentration of CTAB and weight ratio of PS/TEOS were optimized to obtain spherical monodispersed HCSNs. Experimental optimization was carried out by OVAT method. The schematic representation of synthesis of HCSNs using polymer templates is given in Figure 3.1. Variation of reaction parameters for synthesis of HCSNs using PS, sulfonated PS and nitrated PS templates are tabulated in Appendix AI. 2-4.

3.6 Synthesis of SPION embedded HCSNs

0.1 g of PS nanoparticles were dispersed in water-ethanol mixture by ultrasonication for 30 minutes. 5 % CTAB solution was added to the mixture and magnetic stirring was carried out for 2 hours. SPION was added to the mixture and samples were ultrasonicated for 40 minutes. Ammonia was added drop wise to the reaction mixture before the addition of TEOS-ethanol mixture (TEOS mixed with the same amount of ethanol) and

stirred for 4 hours at room temperature. The suspension obtained was aged at room temperature for 24 hours. Separation of the precipitate was done by centrifugation at 10,000 rpm for 10 minutes and washed five times with water. Samples obtained were freeze dried to remove moisture content and were calcined at 550 ^{0}C for 4 hours at a heating rate of 1 ^{o}C/min to remove the PS core. HCSNs were synthesized by varying concentration of SPION as 5, 10 and 30 mg. A Schematic representation of synthesis of SPION embedded HCSNs using PS template is given in Figure 3.2.
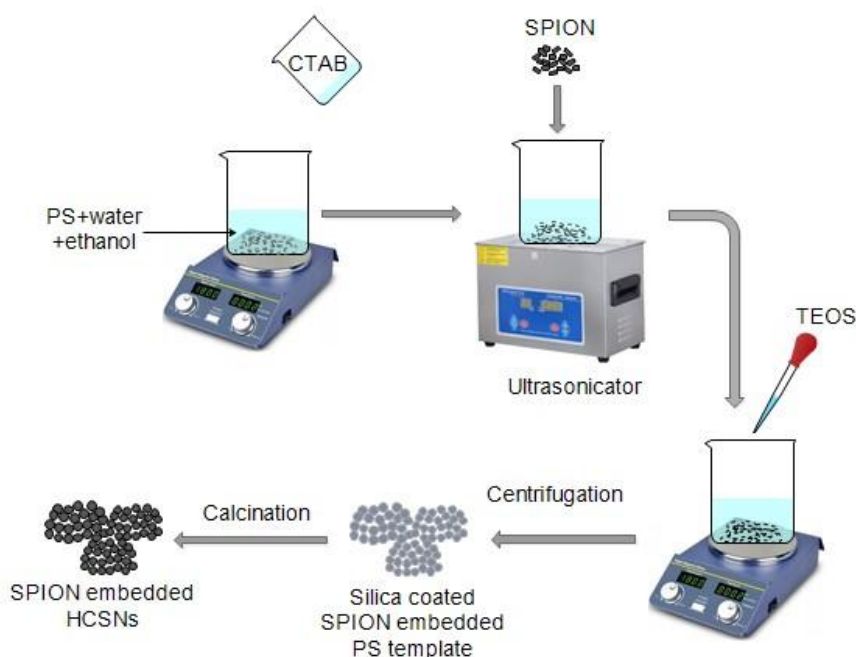
Figure 3.2 Schematic representation of synthesis of SPION embedded HCSNs using PS template

3.6.1 Radiofrequency heating of SPION embedded HCSNs

SPION embedded HCSNs samples were heated in a radio frequency induction heating system. The induction heating machine (ZVS, 48 V, 20 A) with 1 kW power output, operated with frequency of 100 kHz was used as shown in Figure 3.3. The cooling water circuit was provided for the copper coil of diameter 63 mm which generated the radio frequency field. 50 mg of SPION embedded samples T_{f1}, T_{f2} and T_{f3} were dispersed

separately in 10 ml of water and heated in the radio frequency heating system. Time is noted for every 1 ^{0}C rise in the temperature.
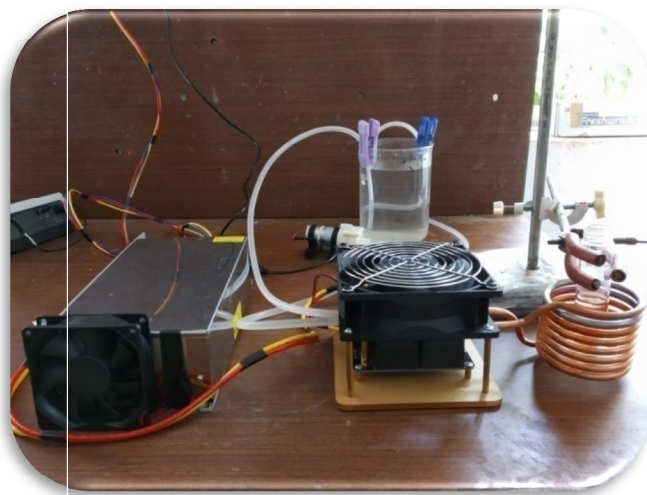
Figure 3.3 Radio frequency induced heating of SPION embedded HCSNs

3.7 Drug loading and release studies

50 mg of HCSNs/SPION embedded HCSNs were well dispersed in 100 ppm doxorubicin solution by ultrasonication for one minute. Samples were stored at 4 ^{0}C for 48 hours. Doxorubicin loaded silica nanoparticles were separated by centrifugation at 12,000 rpm for 15 minutes and dispersed in phosphate buffer of known pH (at pH of 6, 7.4 and 8). The resultant mixture was gently stirred at 37 ^{0}C using a magnetic stirrer (for HCSNs samples). Drug loaded SPION embedded HCSNs samples were maintained at desired temperatures using the radiofrequency heating method. To study the release of doxorubicin, 5 mL of solution was extracted at predetermined time intervals and centrifuged at 12,000 rpm for 5 minutes. The supernatant was analyzed in a UV-visible spectrophotometer at a wavelength of 480 nm and the sample was poured back to maintain a constant volume. Experiments were carried out in duplicates and the average value is reported in the thesis. Calibration curve for doxorubicin is given in Appendix AII.1. The loading capacity and entrapment efficiency of doxorubicin were calculated by using the equations (4) and (5) respectively (Jiao et al. 2012).

$$\text{Loading capacity (wt\%)} = \frac{\text{Mass of drug in the HCSNs}}{\text{Mass of HCSNs}} \times 100 \qquad (4)$$

$$\text{Encapsulation efficiency (wt\%)} = \frac{\text{Mass of drug in the HCSNs}}{\text{Initial mass of drug}} \times 100 \qquad (5)$$

3.8 Cytotoxicity studies

The cytotoxicity studies were carried out by 3-(4,5-dimethylthiazol-2-yl)-2,5-diphenyltetrazolium bromide (MTT) assay method for HCSNs and SPION embedded HCSNs. Human embryonic kidney (HEK 293T) and lung adenocarcinoma (A549) cells were procured from national center for cell sciences, Pune. They were cultured in Dulbecco's modified eagles medium (DMEM) supplemented with 10% fetal bovine serum and 1% antibiotic antimycotic solution. Cells were maintained at 37 ^{0}C with 5% CO_2 in a humidified atmosphere. Cells were seeded onto 96 well microtitre plates at a seeding density of 5000 cells/well. After adherence, they were treated with different concentrations of HCSNs and SPION embedded HCSNs samples dispersed in water (such as 25, 50, 100 and 200 µg/mL). After 48 hours of the post incubation period, MTT assay reagent was added and incubated at 37 ^{0}C for 4 hours. Formazan crystals formed were solubilized using dimethyl sulfoxide and absorbance was recorded at 570 nm using a multimode microplate reader (FluoSTAR Omega, BMG labtech). The percentage viability of the test compounds was calculated with respect to the cell control.

3.9 Characterization techniques

Scanning electron microscope (SEM, JEOL-JSM 6380 LA) and Field emission scanning electron microscope (FESEM) were used to analyze the surface morphology of synthesized nanoparticles. Samples were gold sputtered prior to visualization. The hollow core-shell structure of silica nanoparticles was studied using transmission electron microscopy (TEM, JEOL JEM-2100). Before observing in TEM, samples were dispersed in ethanol by ultrasonication and dropped on to the carbon coated copper grid. Nitrogen adsorption/desorption isotherms of the HCSNs were recorded in a volumetric adsorption

analyzer (Quantachrome Corporation, NOVA1000). The samples were degassed in vacuum at 450 ^{o}C for 8 hours and analysis was carried out at 77 K over a range of relative pressures (P/P$_0$). The specific surface area was calculated by using BET and the pore size distribution was obtained from desorption isotherm curves using Barrett–Joyner–Halenda (BJH) methods. X-ray diffraction (XRD) pattern of HCSNs was obtained using Rigaku Miniflex-600 diffractometer with Cu Kα radiation, operated at 40 kV and 15 mA. XRD patterns were recorded for 2θ ranging from 5 ^{0} to 90 ^{0} with a scanning step of 0.02 ^{0}. Fourier transform infrared spectra (FTIR) of the PS, silica coated PS and HCSNs were obtained by the KBr pellet technique using FTIR (Thermonicolet Avatar-370). Thermogravimetric analysis (TGA) was carried out at a heating rate of 10 K/min from room temperature to 750 ^{0}C in airflow by using TG/TGA instrument (Hitachi-6300). Horiba (SZ-100) instrument was used to find out the zeta potential and particle size, by dispersing the samples in distilled water by ultrasonication at pH 7. The drug uptake and release were monitored by UV-visible spectrophotometer (Hitachi, U-2900). Magnetic properties of SPION embedded HCSNs samples were analyzed using Physical Property Measurement System 9T (Quantum Designs/PPMS 639) in vibrating sample magnetometer (VSM) mode.

CHAPTER 4

4. RESULTS AND DISCUSSION

Part I

4.1 HCSNs synthesis by using sacrificial PS template and application in targeted drug delivery

A simple two-step method is adopted to synthesize HCSNs. PS nanoparticles were synthesized in the first step and they were used as sacrificial templates in the second step while synthesizing HCSNs. Effects of parameters like water-ethanol volume ratio, concentration of ammonia, concentration of CTAB, and PS/tetraethyl orthosilicate (TEOS) weight ratio on morphology of HCSNs were analyzed. The microporous HCSNs with tunable shell thickness and hollow core-shell structure was found to have high demand in the field of drug delivery. Therefore, loading and release properties of HCSNs were examined using doxorubicin as a model drug.

4.1.1 PS synthesis and optimization

PS nanoparticles were synthesized by emulsion polymerization technique. The process variables such as initiator concentration, stabilizer concentration, reaction temperature and reaction time were optimized to obtain spherical monodispersed PS nanoparticles.

Effect of initiator concentration on PS particle size and morphology: FESEM images of PS nanoparticles synthesized at different initiator concentrations are shown in Figure 4.1. Polymerization reaction was initiated in the presence of an initiator and generating nuclei through which particles were formed. The PS nanoparticles grew and separated from the reaction medium. Absence of spherical shaped PS particles was evident at lower concentration of initiator (<129 mmols). However, lower concentration of initiator caused the reduction in concentration of free radicals available for the occurrence of polymerization (Liu et al. 2016).

It was also found that with increase in the concentration of initiator to 129 mmols, uniform sized, spherical PS nanoparticles were obtained. The reason behind this behavior could be explained based on free radical concentration. As KPS concentration was increased, a large number of free radicals were formed which increased the number of polymer nuclei. Higher free radical concentration promoted the growth of nuclei present in the reaction medium (Yoon et al. 2014; Yun et al. 2010).
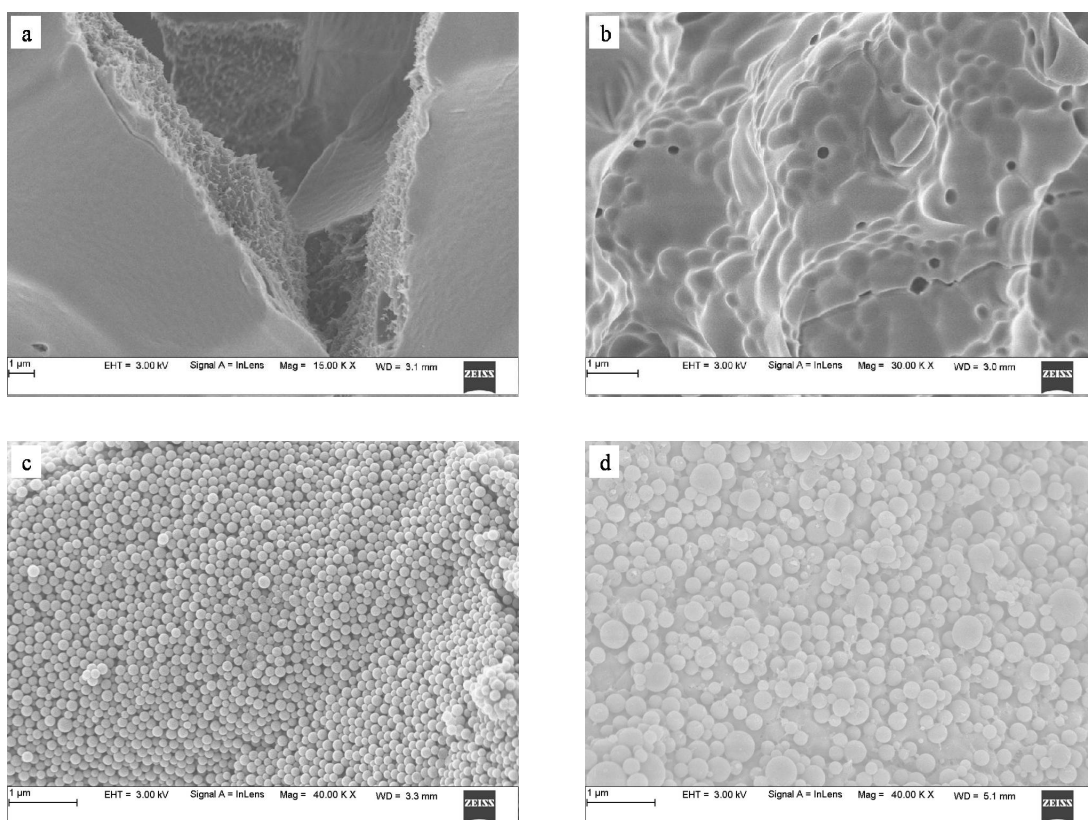
Figure 4.1 FESEM images of PS nanoparticles synthesized by variation of initiator concentration (in µmol): a) 55; b) 96; c) 129; d) 166. Styrene 45 mmols, PVP 15 µmols, water 45 mL, reaction time 24 hour and reaction temperature 70 ^{0}C

Effect of stabilizer concentration: Influence of the stabilizer concentration on particle size and morphology is represented in Figure 4.2. PVP acted as a stabilizing agent during the

polymerization reaction and played a crucial role in procuring PS nanoparticles in a spherical shape.
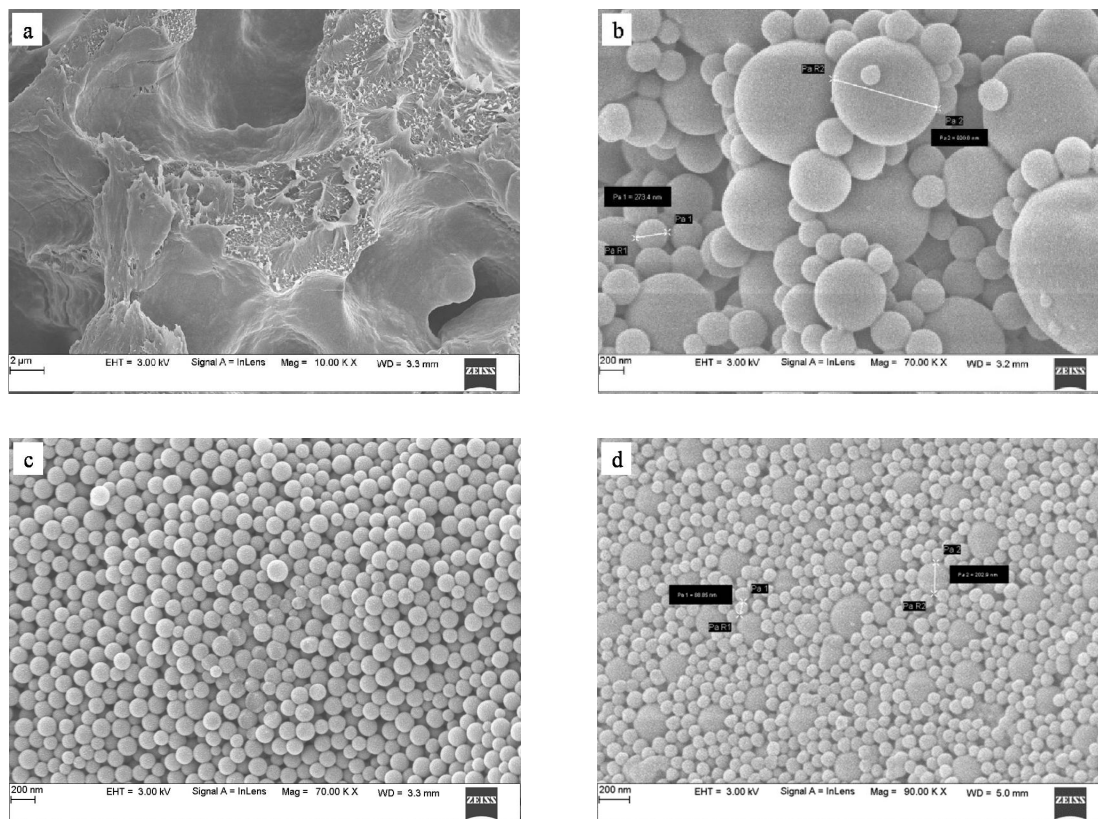
Figure 4.2 FESEM images of PS synthesized by variation of stabilizer concentrations (in μmols): a) 3.7; b) 7.5; c) 15; d) 30. Styrene 45 mmols, KPS 129 μmols, water 45 mL, reaction time 24 hour and reaction temperature 70 ^{0}C

Agglomeration of colloidal particles with the PS nanoparticles was reduced by the addition of PVP, which lead to reduction in the size of PS nanoparticles (Gorsd et al. 2012). PVP covered the negative surface charge of PS when used at higher concentration of about 15 μmols (Sandberg et al. 2013). There was a gradual reduction in the PS particle size with increase in the concentration of PVP as observed in Figure 4.2 (Milosevic et al. 2009). The large surface area of PS nanoparticles was stabilized by the addition of PVP (stabilizer) at higher concentrations (Zou et al. 2008). Thus, reduction in

the growth of existing polymers was prominent which lead to decrease in size of PS nanoparticles (Figure 4.2c, d). Spherical shaped PS particles were not observed at a lower concentration of PVP (3.7 µmols), due to the insufficient concentration of PVP.

Effect of reaction temperature:
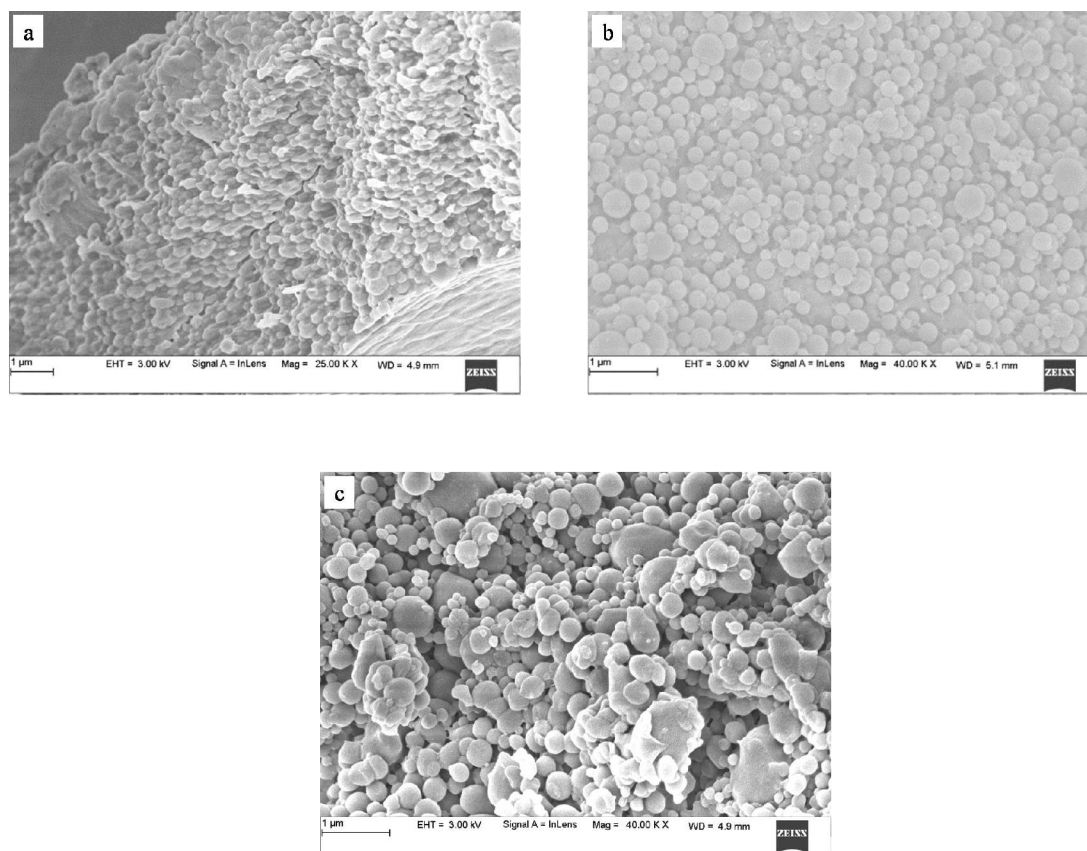
Figure 4.3 FESEM images of PS nanoparticles synthesized by variation of temperature a) 60 ^{0}C; b) 70 ^{0}C; c) 80 ^{0}C. Styrene 45 mmols, KPS 129 µmols, PVP 15 µmols, water 45 mL and reaction time 24 hour

Figure 4.3 represents variation in the PS particle size with respect to variation in reaction temperature from 60-80 ^{0}C. Fewer numbers of free radicals were produced at lower temperature (60 ^{0}C) lead to the formation of agglomerated PS particles which were not in a spherical shape (Figure 4a). When the reaction temperature was raised to 70 ^{0}C, the

46

thermodecomposition of the initiator showed an increase. Thus, large numbers of free radicals were made available for polymerization reaction at temperatures above 70 ^{0}C, resulted in the growth of PS particles (Figure 4.3) (Kaiyi and Zhaoqun 2007; Yun et al. 2010).

Effect of reaction time: PS particle sizes were measured at different reaction time. SEM images of PS synthesized at 1, 2, 6, 18 and 24 hours reaction time are shown in Figure 4.4. With reaction time of 1 hour, particles produced were not in spherical shapes. However, PS nanoparticles of clear spherical shape with narrow size distribution were obtained after 2 hours of reaction time. Further, particle size was found to increase with increase in the reaction time due to the binding of more number of nuclei to the PS nanoparticles (Liu et al. 2016). However, the growth of PS nanoparticles was rapid at the early reaction stages and reached a steady level after 18 hours (Figure 4.4), which was similar to the earlier literature (Yun et al. 2010). The reaction time of 24 hours was used further to obtain monodispersed spherical PS nanoparticles.

Particle size measured by varying initiator concentration, stabilizer concentration, reaction temperature and reaction time are displayed in Figure 4.5. Zeta potential of PS was found to be -53.3±0.43 mV at pH of 7. Image of the white colored PS powder is shown in Figure 4.6. For further studies, PS nanoparticles were synthesized using the following conditions such as KPS concentration of 129 μmols, PVP concentration of 15 μmols for reaction time of 24 hours at reaction temperature of 70 ^{0}C to obtain monodispersed spherical particles of average particle size 150±20 nm.
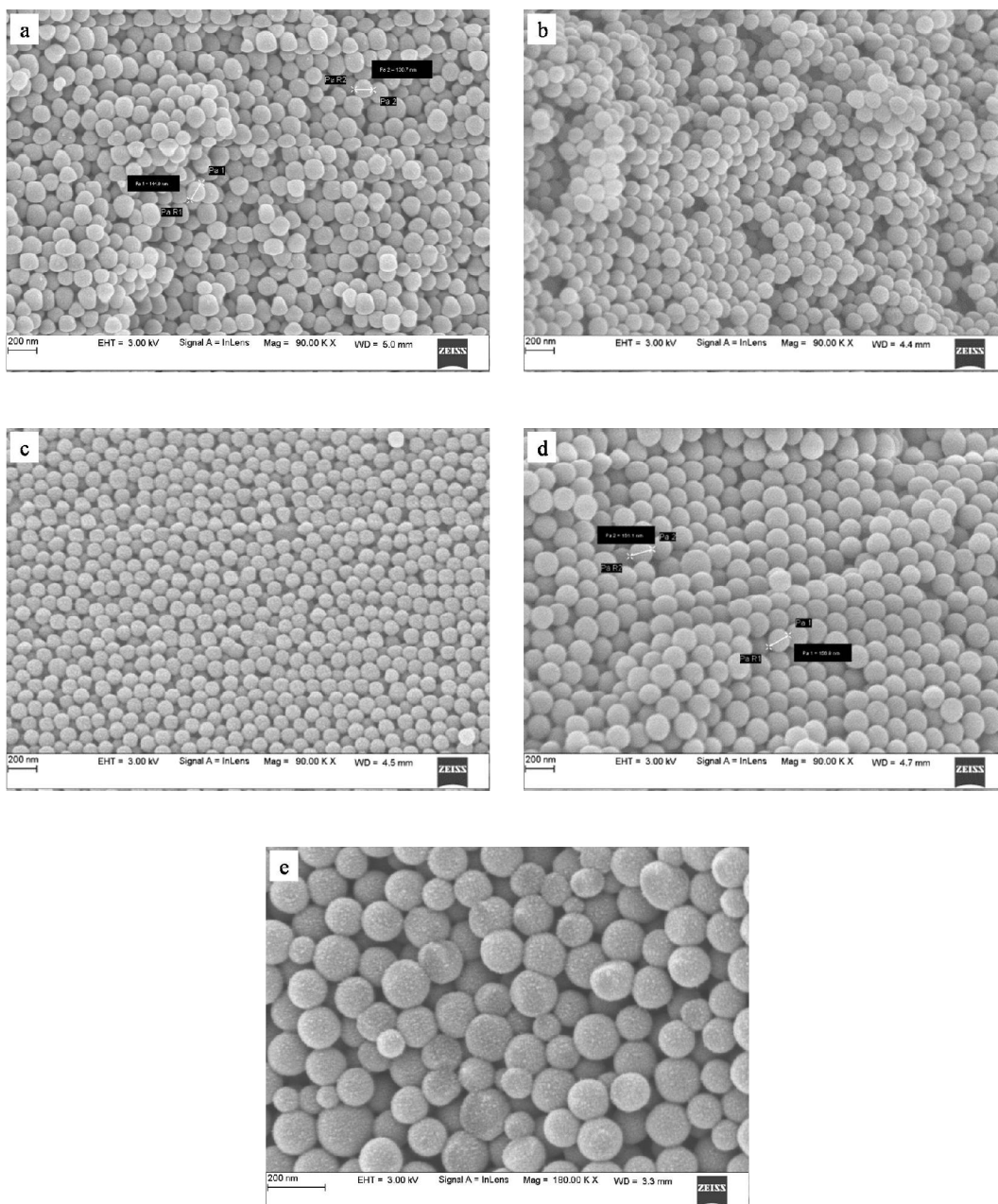
Figure 4.4 FESEM images of PS nanoparticles synthesized by variation of reaction time (hours) a) 1; b) 2; c) 6; d) 18; e) 24. Styrene 45 mmols, KPS 129 μmols, PVP 15 μmols, water 45 mL and reaction temperature 70 ^{0}C
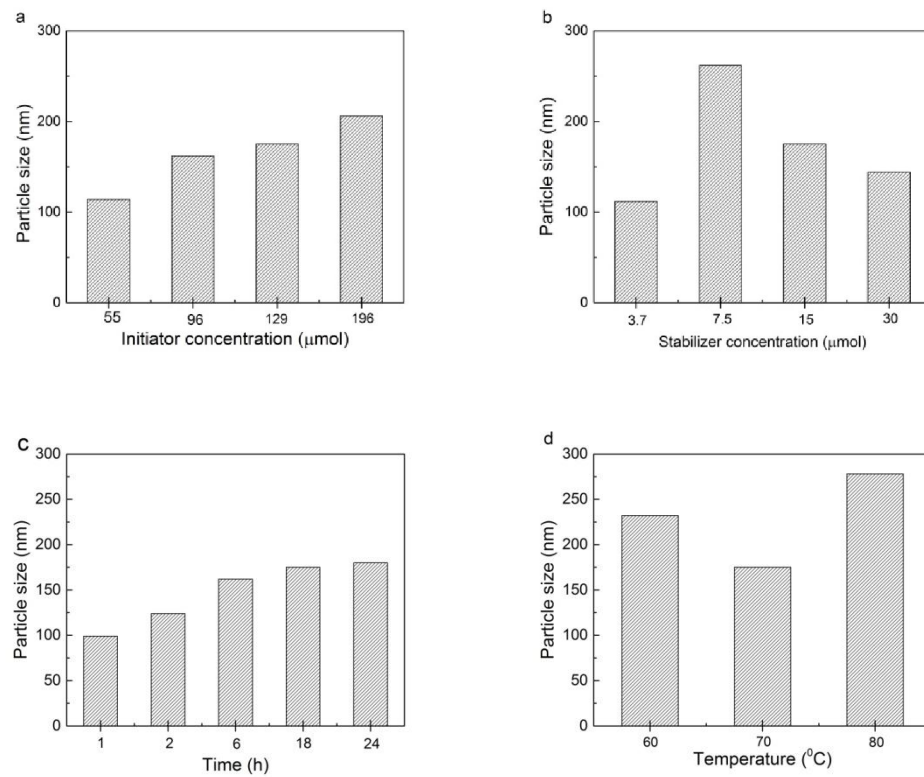
Figure 4.5 Particle size measured by nanoparticle size analyzer with increase in a) concentration of initiator; b) stabilizer; c) reaction time; d) reaction temperature

Figure 4.6 Image of PS nanoparticles

4.1.2 Synthesis of HCSNs using PS template and optimization

HCSNs were synthesized using PS as the template by optimizing reaction parameters such as water/ethanol ratio, concentration of ammonia, concentration of CTAB and concentration of TEOS to achieve the desired morphology.

Effect of variation of water/ethanol ratio: The effect of variation in water/ethanol volume ratio on the morphology of HCSNs is represented in Figure 4.7. The particles were found to be in random shape and highly porous in nature when water alone was used as the dispersion medium (Figure 4.7a). The irregularity in particle size was due to the rapid hydrolysis and condensation of TEOS (Berru et al. 2013). Figure 4.7(b-d) shows the variation in morphology of HCSNs as the fraction of water reduces from 4:1 to 1:4, in the mixture of water-ethanol. Monodispersed HCSNs with a smooth surface and spherical shape were achieved when the volume ratio of water/ethanol was maintained as 1:4 (Figure 4.7d). The HCSNs were found to agglomerate when ethanol alone was used as the dispersion medium (Figure 4.7e). Agglomeration was due to the low rate of hydrolysis and condensation of TEOS, since water was not used as the dispersion medium. Thus, it reduced the rate of formation of silica shell on the surface of PS particle (Yuan et al. 2010).
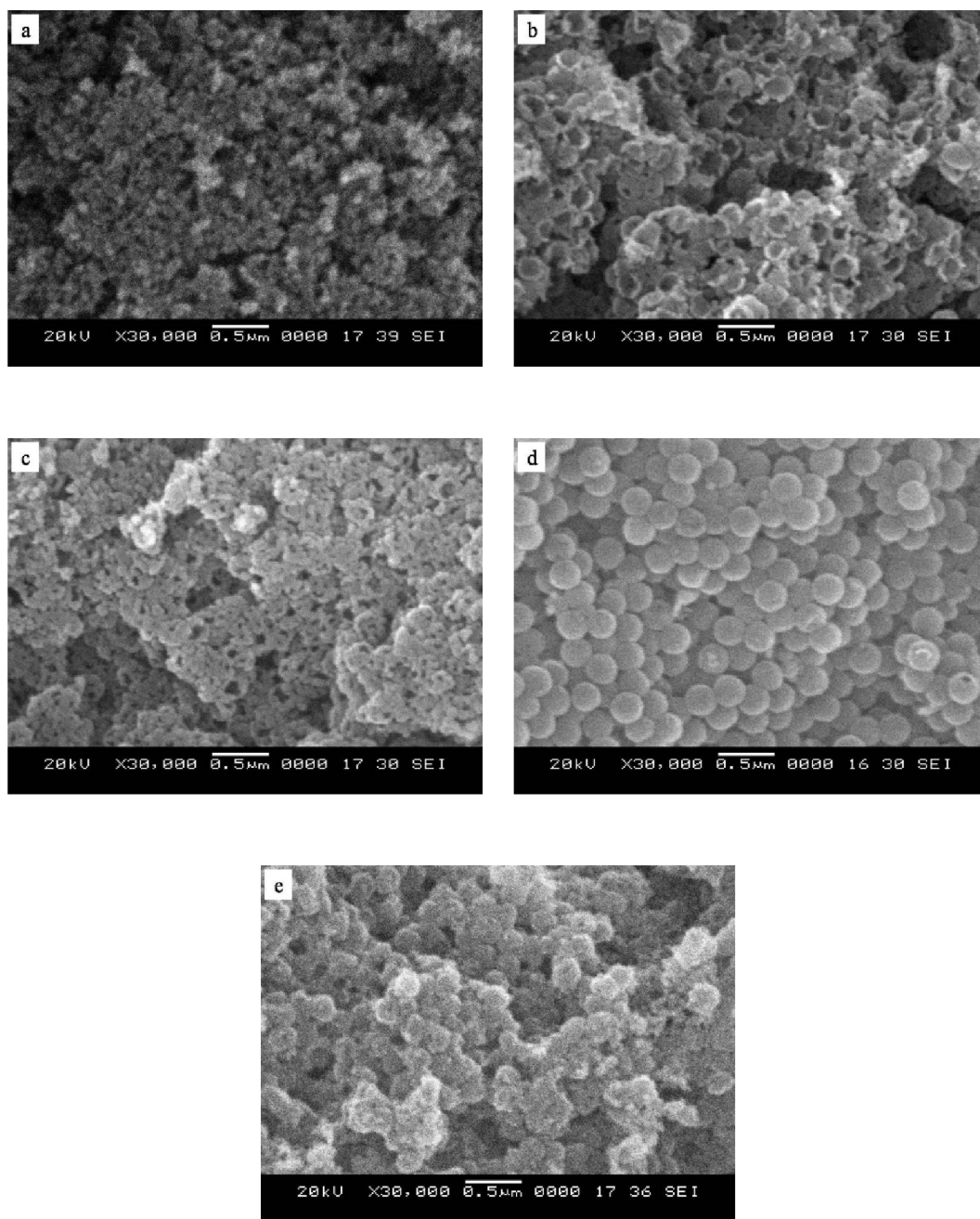
Figure 4.7 SEM images of HCSNs synthesized by variation of water/ethanol volume ratio a) 100% water; b) 4:1; c) 3:2; d) 1:4; e) 100% ethanol (6 ml CTAB, 1 g TEOS, 0.5 mL ammonia)

Effect of variation of ammonia concentration:
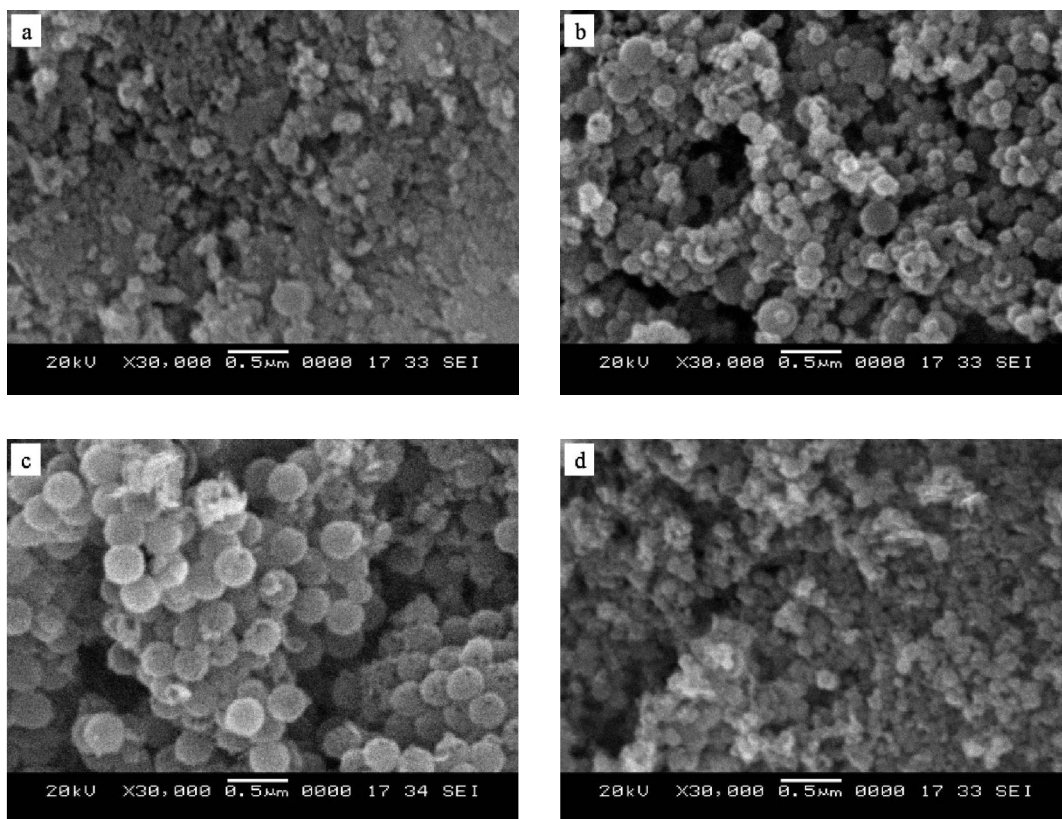
Figure 4.8 SEM images of HCSNs synthesized using sacrificial PS template by variation of ammonia concentration a) 0.2 mL; b) 0.3 mL; c) 0.5 mL; d) 0.7 mL (1:1 weight ratio of PS/TEOS, 6 ml CTAB, 1:4 volume ratio of water/ethanol)

The morphology of the silica shell was also influenced by the concentration of ammonia, which was used as the catalyst during the synthesis of HCSNs (Stober et al. 1968). At a low concentration of ammonia, poor coating of silica on the surface of PS and also agglomeration of particles was observed as shown in Figure 4.8 (a, b). Thus, low hydrolysis rate of TEOS would not be preferable to coat silica on the surface of PS nanoparticles (Yuan et al. 2010). However, as the concentration of ammonia was increased from 0.2 mL to 0.5 mL, the uniform coating was observed resulting in the formation of monodispersed spherical particles (Figure 4.8c). Further increasing the

concentration of ammonia from 0.5 mL to 0.7 mL, undesirable free silica particles were observed (Figure 4.8d) which was due to the heterogeneous nucleation of silica nanoparticles with an increased rate of hydrolysis and condensation of TEOS (Park et al. 2009)

Effect of variation of CTAB concentration:
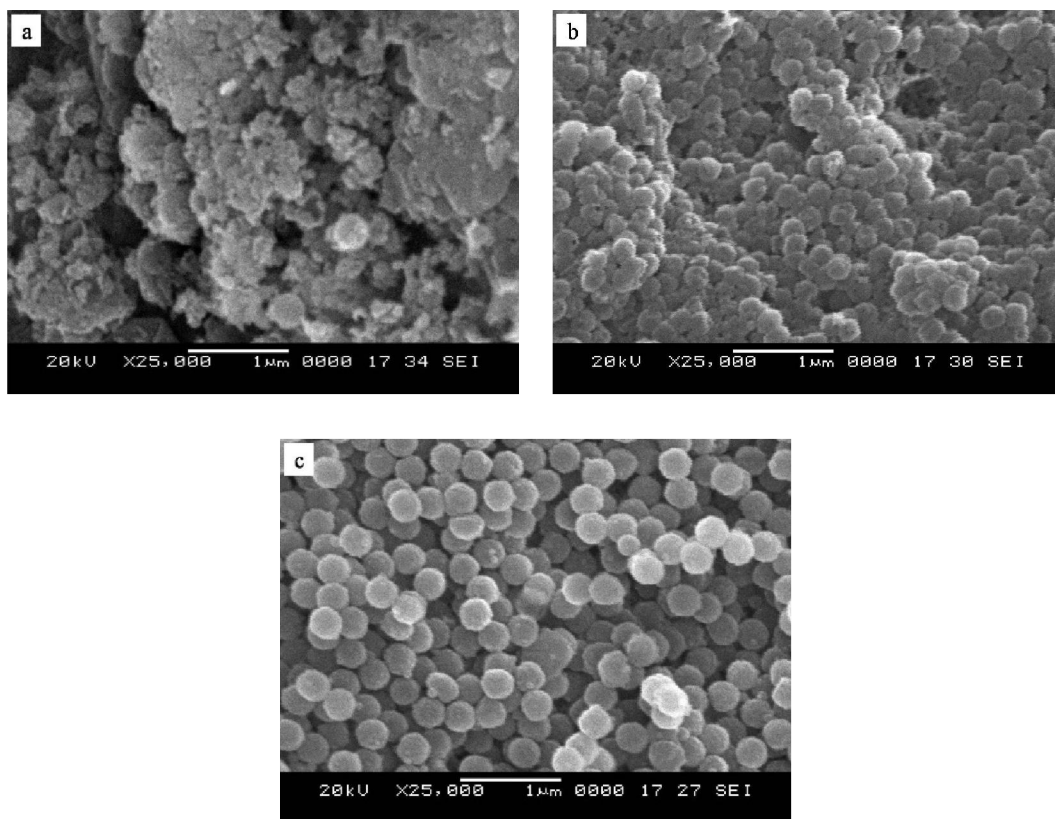
Figure 4.9 SEM images of HCSNs synthesized using sacrificial PS template by variation of CTAB concentration a) 2 ml; b) 6 ml; c) 10 ml (1:1 weight ratio of PS/TEOS, 0.5 mL ammonia, 1:4 volume ratio of water/ethanol)

CTAB acted as a wall formation directing agent by introducing positive charge on the surface of the PS particles. Thus, negatively charged silica sol formed from TEOS bound to the surface of CTAB coated PS (Niu et al. 2010). When the concentration of CTAB was increased (from 2 ml to 10 ml), PS nanoparticles were coated completely with

CTAB. As a result, reduction in agglomerations between HCSNs was observed as shown in Figure 4.9(a-c). Thus, usage of CTAB enabled the formation of uniform silica shell and spherical, monodispersed HCSNs.

Effect of variation of PS/TEOS ratio:
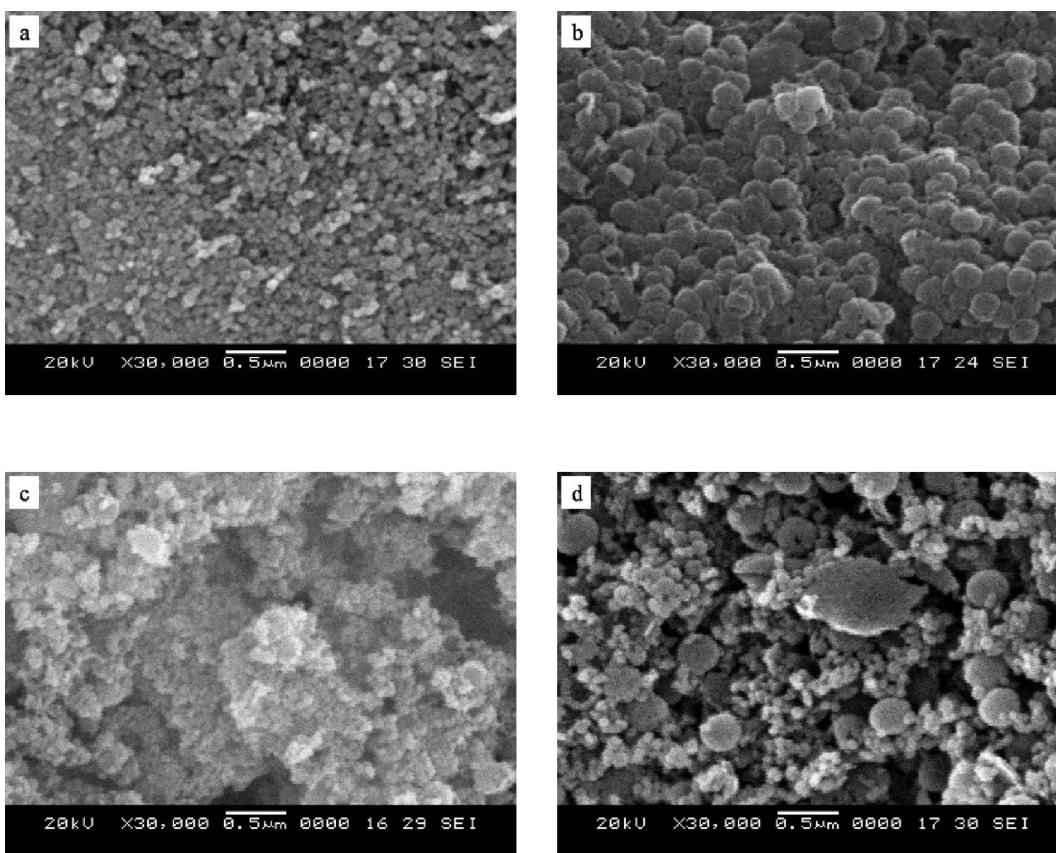
Figure 4.10 SEM images of HCSNs synthesized using sacrificial PS template by PS/TEOS weight ratio variation a) 2:1; b) 1:1; c) 1:2; d) 1:4 (6 ml CTAB, 0.5 mL ammonia, 1:4 volume ratio of water/ethanol)

When the weight ratio of PS/TEOS was maintained as 2:1, the formation of solid silica nanoparticles was observed due to the insufficient concentration of silica sol (Figure 4.10a). An optimum ratio of PS/TEOS of 1:1 was maintained to synthesize HCSNs

(Figure 4.10b). When the concentration of TEOS was further increased, the formation of undesirable solid silica nanoparticles was observed (Figure 4.10c,d), similar to the literature data (Deng et al. 2006; Nguyen et al. 2014).
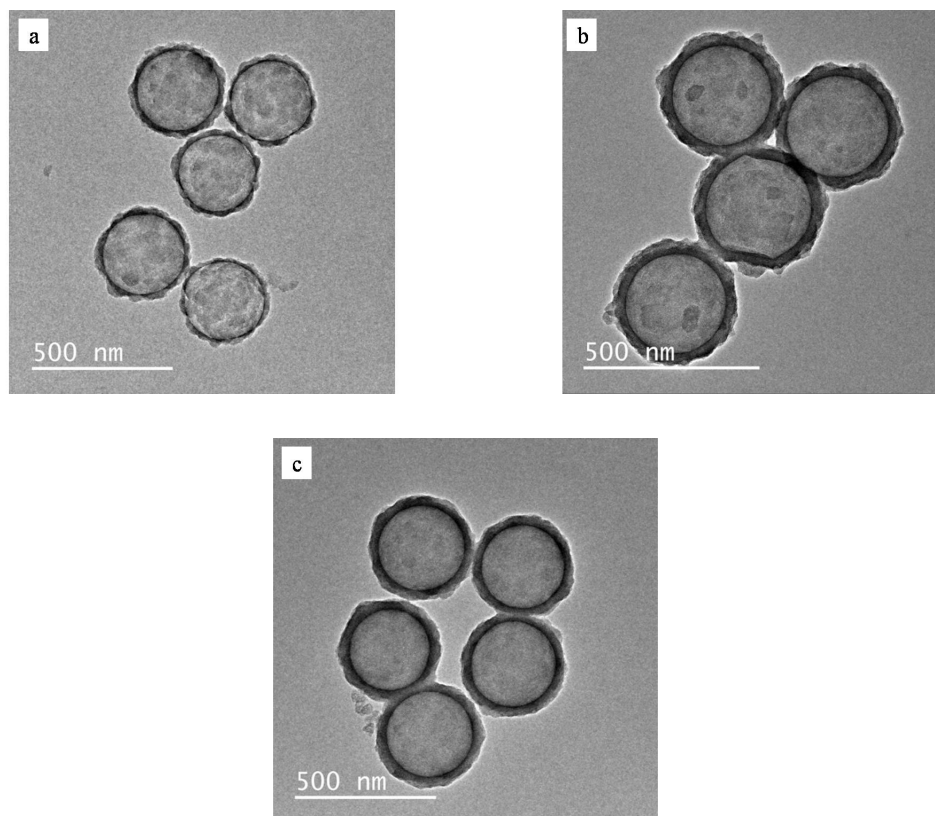
Figure 4.11 TEM micrographs of HCSNs using sacrificial PS template by PS/TEOS variation a) T_1; b) T_2; c) T_3 (6 ml CTAB, 0.5 mL ammonia, 1:4 volume ratio of water/ethanol)

The thickness of silica shell could be modified by varying the concentration of silica precursor (Deng et al. 2006; Yuan et al. 2010). Silica nanoparticles of varied thicknesses were synthesized by tailoring the concentration of TEOS, such that the weight ratio of PS/TEOS was maintained in the range, within 1:1 to 1:2. When TEOS was added during the synthesis of HCSNs, initially TEOS hydrolyzed and condensed to form a layer of silica on the surface of CTAB coated PS template. The silica layer became thicker as

more amount of TEOS condensed (Chen et al. 2013). Thus, HCSNs of varied thicknesses were synthesized by tailoring the concentration of TEOS, such that the weight ratio of PS/TEOS was maintained in the range of 1:1 to 1:2.

Earlier studies have reported that the synthesis of mesoporous silica nanoparticles with varied shell thickness by controlling the concentration of TEOS. Jiao et al. (2012) showed the variation in shell thickness from 20-95 nm, where poly(tert-butylacrylate) was used as a sacrificial template. Mohamed El-Toni et al. (2012) obtained shell thickness in the range of 41-80 nm while using anionic surfactant as a template. TEM micrographs of synthesized HCSNs samples are shown in Figure 5.10(a-c) which confirmed the formation of hollow core-shell structure of silica nanoparticles of size 230±30 nm. HCSNs were found to be monodispersed and spherical in nature when the weight ratio of PS/TEOS was varied as 1:1, 2:3 and 4:7. In the present study thickness of the shell was found to increase from 15 nm to 30 nm with increase in the amount of TEOS (PS/TEOS weight ratio between 1:1 to 4:7) as reported in Table 4.1.

Table 4.1 Variation of thickness of silica shell with PS/TEOS weight ratio for samples T1, T2 and T3

Sample Name	PS/TEOS weight ratio	Thickness (nm)	Average specific surface area (m^2/g)	Pore diameter (nm)
T_1	1:1	15	747.5	1.5
T_2	2:3	20	617.3	1.3
T_3	4:7	30	600.8	1.2

4.1.3 Structural and thermal analysis of HCSNs synthesized using sacrificial PS template

Typical nitrogen adsorption/desorption isotherms at 77 K and pore size distribution curves for the prepared HCSNs are shown in Figure 4.12(a-c). The average specific surface area for the samples T_1, T_2 and T_3 calculated by BET analysis is found in the range of 747.5 to 600.8 m^2/g (Table 4.1.). The pore size distribution data calculated by the BJH method confirmed the narrow size range from 1.2 to 1.5 nm which is less than the pore sizes shown in the earlier reports.
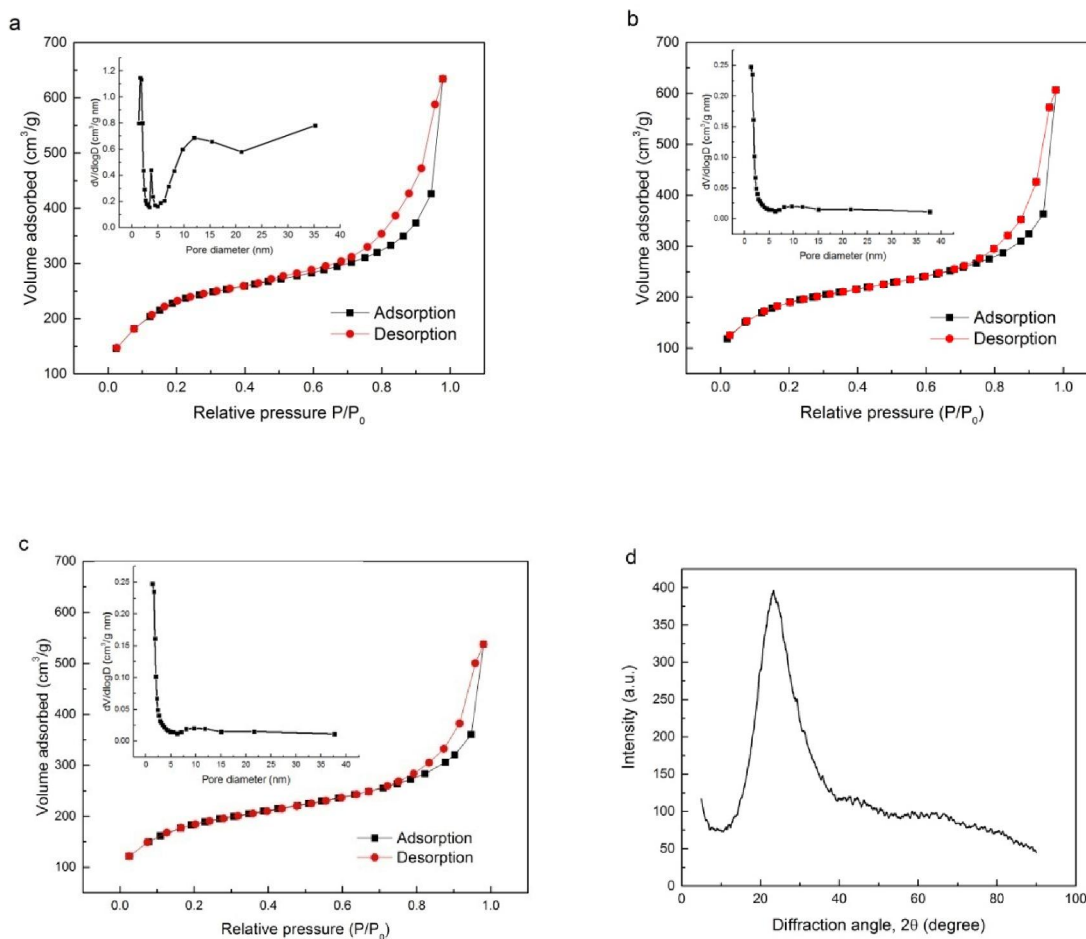
Figure 4.12 Nitrogen adsorption/desorption isotherm and pore size distribution for HCSNs samples a) T_1; b) T_2; c) T_3; d) XRD analysis of HCSNs

The majority of the previous studies were focused on the synthesis of mesoporous silica nanoparticles with pore sizes above 2 nm using various sacrificial templates like PS, anionic surfactant and amphiphilic block copolymers (Mohamed El-Toni et al. 2012; Zhang et al. 2009b; Zhou et al. 2014). The BET isotherms of HCSNs samples were observed to follow H4 type hysteresis curve (Thommes et al. 2015). In the current study, we found that pore diameters of HCSNs were not significantly affected when the thickness of silica shell was varied. The powder XRD pattern of the hollow core-shell silica nanoparticles shows characteristic diffraction peak of silica at 23^0 (Figure 4.12d) (Nguyen et al. 2014).

FTIR analysis plot for PS and HCSNs samples is shown in Figure 4.13. The strong FTIR absorption bands around 2850-3060, 1666, 1493, 755 cm^{-1} are the characteristic peaks of PS as represented in Figure 4.13a (Agrawal et al. 2008; Ding et al. 2004). The peaks due to alkyl (C_nH_{2n+1}) groups (in the range of 2850-3060 cm^{-1}) disappeared in HCSNs, which confirmed the complete removal of PS template by the calcination process (Figure 4.13b). Three strong peaks observed at 1090, 800 and 462 cm^{-1} are from Si-O-Si vibrations confirmed the formation of HCSNs (Liu et al. 2012; Nandiyanto et al. 2009).
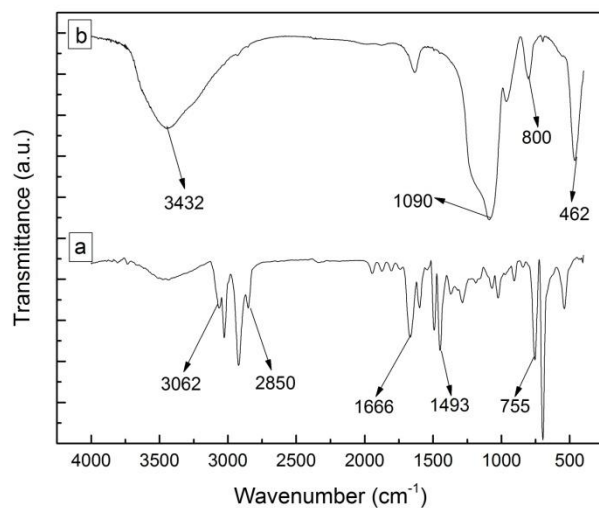
Figure 4.13 FTIR spectra of a) PS; b) HCSNs
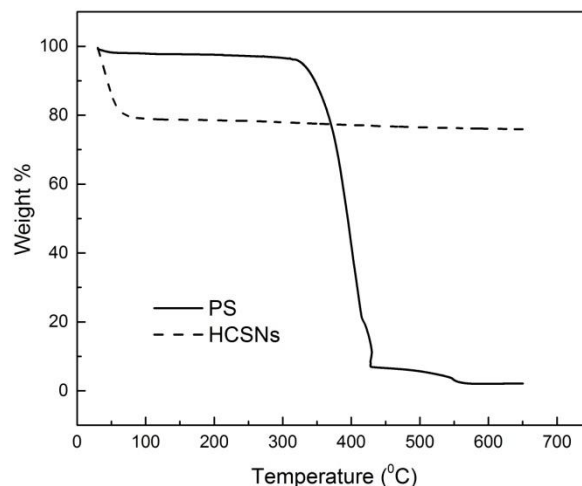
Figure 4.14 TGA plot for PS and HCSNs

TGA curves for PS and silica coated PS exhibited a rapid drop in weight at $\sim$310 ^{0}C and plateau at >550 ^{0}C as shown in Figure 4.14. The weight loss observed at lower temperatures (<100 ^{0}C) was due to the evaporation of water adsorbed on the surface (Nguyen et al. 2014). Since there was no weight loss observed in the TGA curve for HCSNs at higher temperatures which confirmed the absence of any remnant PS particles along with silica particles.

4.1.4 Formation of HCSNs using sacrificial PS template

The formation of HCSNs using PS sacrificial template can be explained as follows. Scheme of evolution of HCSNs using PS as sacrificial template is represented in Figure 4.15. The surface of PS was negatively charged and CTAB micelles couple with negatively charged PS in the presence of aqueous ammonia solution (Du and He 2008). CTAB-PS composites were generated via electrostatic interactions between CTA+ and PS-, which was similar to the process proposed by Niu et al. (2010). As soon as the TEOS molecules were added, they were hydrolyzed and silica ions started to assemble with CTAB by self assembly leading to the growth of silica on the surface of the PS

particles (Liu et al.2012; Zhang et al. 2013). PS templates were removed completely by calcination at an elevated temperature of 550 ^{0}C which was confirmed by TGA analysis.
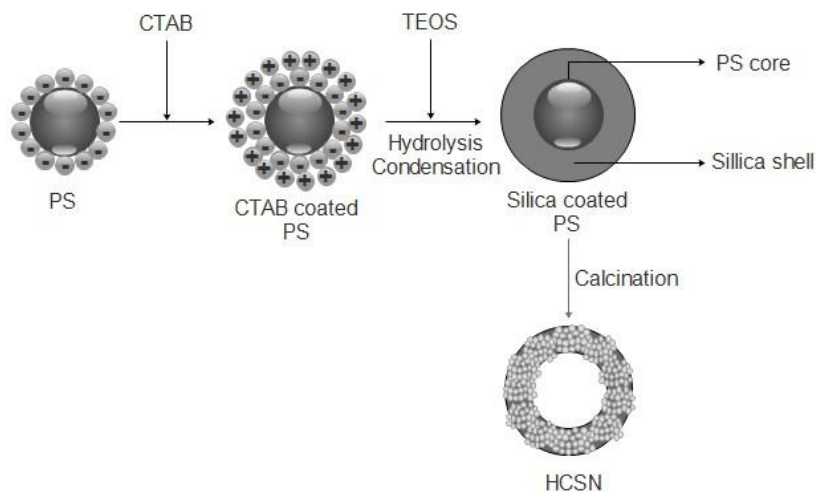
Figure 4.15 Schematic representation of synthesis of HCSNs using PS template

4.1.5 Loading and release studies using HCSNs synthesized using sacrificial PS template

The loading and release properties of HCSNs as drug carriers were explored using doxorubicin, an anticancer drug. Doxorubicin loading capacities of samples T_1, T_2 and T_3 were found to be 1.2, 1.08 and 1.06 wt% respectively. Small variation in the loading capacities might be due to the similar core sizes which has lead to equal loading of the drug (Jiao et al. 2012). Since the PS cores of same size were used during the synthesis of samples T_1, T_2 and T_3. Similar values of loading capacities were also reported by Bouchoucha et al. (2016).
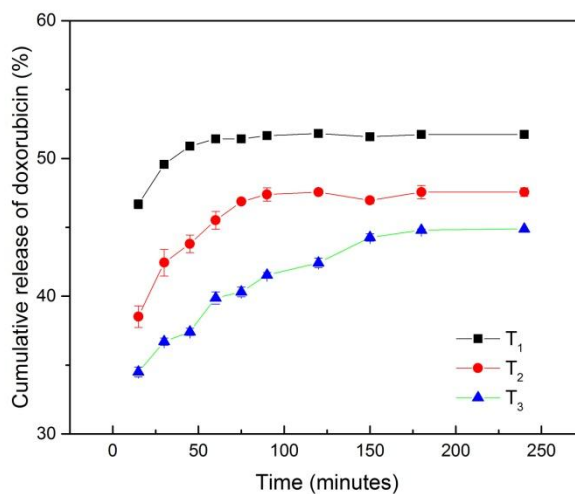
Figure 4.16 Cumulative doxorubicin release profile for HCSNs at different thicknesses

Doxorubicin encapsulation efficiencies of samples T_1, T_2 and T_3 were estimated to be 35.7, 33.01 and 32.27 wt% respectively. The N_2 adsorption-desorption studies revealed that the pore sizes of HCSNs were almost remained the same (1.5 to 1.2 nm) while the shell thickness was varied (Table 4.1), which could be the reason for similar values of encapsulation efficiencies. Thus, doxorubicin was predominantly stored in the hollow core and partially adsorbed in the shell. However, a slight decrease in encapsulation efficiency could be attributed to the decrease in surface area of HCSNs samples T_1, T_2 and T_3 (Table 4.1). In the present study, moderately higher encapsulation efficiency was observed compared to the studies done by Mohamed El-Toni et al. (2012) on mesoporous silica spheres.

Release kinetics showed a high initial dose followed by a steady dosage of the drug for prolonged period of time. The rapid leaching of doxorubicin was observed during the initial period, due to the release of molecules coated on the surface and pore entrance (Li et al. 2004; Zhang et al. 2012a). Figure 4.16 shows the cumulative doxorubicin release profile for HCSNs samples with different thicknesses (T_1, T_2 and T_3). Doxorubicin

release prolonged for 200 minutes and attained steady state further, as observed in Figure 4.16.

The two major factors influencing the doxorubicin release rate are shell thickness and surface area of HCSNs (Li et al. 2004; Niu et al. 2010). Sample T_1 showed the fastest release rate (46.6 % within 15 minutes) with the shortest thickness of 15 nm and the lowest microchannel length which had permitted the rapid diffusion of doxorubicin into the phosphate buffer medium. However, it exhibited the largest specific surface area (747.478 m^2/g) compared to the other two samples which had caused facile leaching of drug molecules from the core. Similarly, variation in the release rate for the samples T_2 and T_3 could be correlated to their shell thickness and surface area. The lowest release rate (34.5 % after 15 minutes) was observed for the HCSNs with a highest shell thickness of 30 nm (sample T_3), where the longer microchannel length led to the slower diffusion rate of the drug molecules into the medium. Moreover, it had a lower specific surface area (600.828 m^2/g), which had inhibited the rapid release of drug in to the medium. When the thickness of the silica shell decreases from 30 to 15 nm, doxorubicin diffused out easily through the porous shell (Jiao et al. 2012).
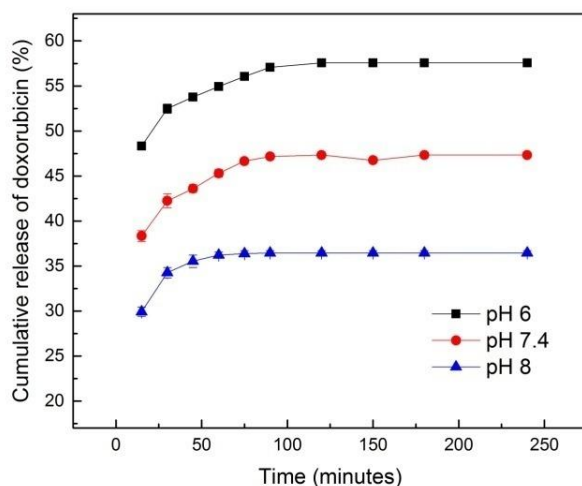
Figure 4.17 Cumulative doxorubicin release profile for HCSNs at different pH (6, 7.4 and 8) for sample T_2

The delay in drug release with the increase in shell thickness and decrease in surface area is in accordance with the findings of Mohamed El-Toni et al. (2012). Lower drug release rates could be advantageous in delivering the therapeutic amount of drug for a prolonged period of time by targeted drug delivery system.

Release medium pH is one of the important parameters which effects the release of drug from the carrier (Mhlanga and Ray 2015). The effect of pH on doxorubicin release was studied on sample T_2 at pH of 6, 7.4 and 8 as displayed in Figure 4.17. At lower pH (pH-6), higher release of drug (48.3 % in 15 minutes) was observed due to the higher solubility of doxorubicin. Poor solubility of doxorubicin was the primary cause of lower release at a higher pH of 8. The drug release at pH 6 and 7.4 followed a similar trend as shown in the plot. Quantity of drug released at pH 6 was found to be higher than that at pH 7.4 (Jiao et al. 2012).

4.1.6 Mathematical modeling of drug release from HCSNs synthesized using PS template for HCSNs

The cumulative release of doxorubicin was studied in phosphate buffer having pH 7.4 as shown in Figure 4.16. Further, the obtained data were fitted in zero order, first order and Higuchi models as depicted in Figure 4.18. Doxorubicin release pattern fitted with various models were analyzed based on the regression coefficient R. Table 4.2 summarizes the regression coefficient R and values of constants K_0, K_1 and K_2.

Table 4.2 Correlation coefficients of mathematical models for samples T_1, T_2 and T_3

Sample name	Zero order		First order		Higuchi model	
	K_0	R^2	K_1	R^2	K_2	R^2
T_1	0.103	0.894	2.24×10^{-3}	0.942	1.236	0.92
T_2	0.086	0.974	1.57×10^{-3}	0.977	1.564	0.96
T_3	0.062	0.949	1.49×10^{-3}	0.970	1.120	0.96

The drug release from the HCSNs was found to show the best fit for the first order model. Thus, the release of doxorubicin from the samples was controlled by the amount of drug spared in the HCSNs. Other models did not provide $R^2 > 0.97$. However, these models are associated with errors due to several factors such as the intrinsic dissolution rate of drug, change in nature of the drug and so on (Costa and Lobo 2001; Varga et al. 2014).
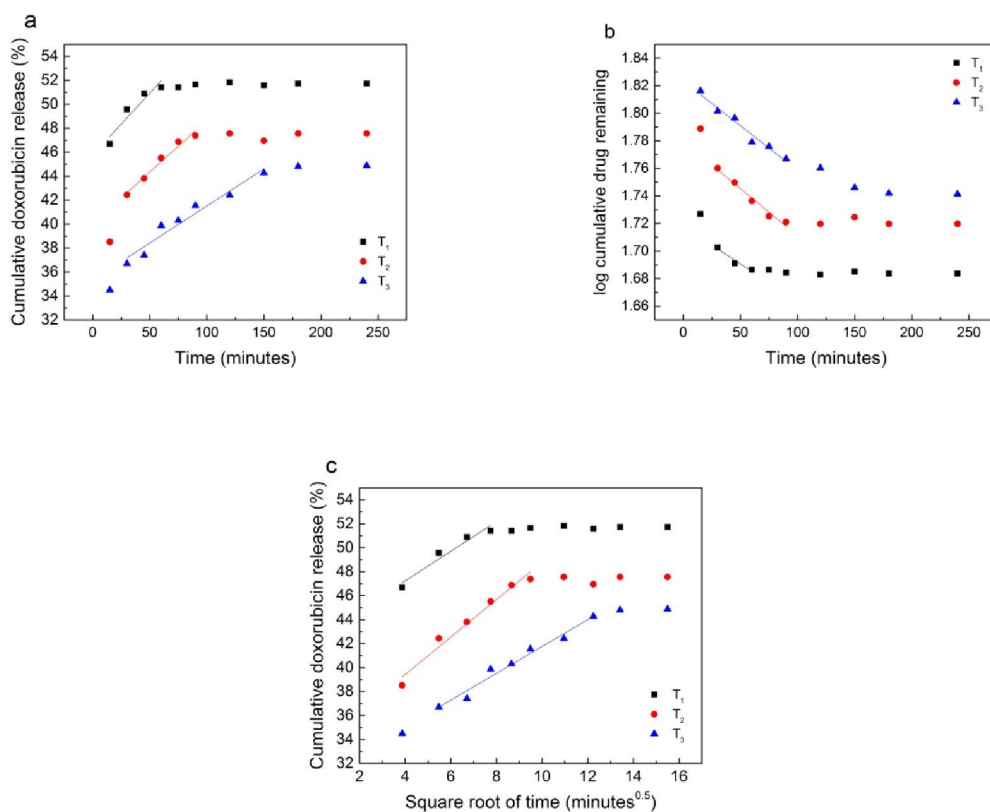
Figure 4.18 Doxorubicin release kinetics for samples T_1, T_2 and T_3 a) Zero order; b) First order; c) Higuchi model

4.1.7 Cytotoxicity studies for HCSNs synthesized using PS template

The biocompatibility of HCSNs was determined by cytotoxicity studies using MTT assay method. HCSNs were introduced on the normal cells (human embryonic kidney cells, HEK 293T) which showed IC_{50} values above 94% as observed from the plot of cell

viability versus concentration (Figure 4.19a). Thus, the samples did not cause any toxicity to the normal cells when the concentration of samples increased from 25 µg/ml to 200 µg/ml. Figure 4.19b shows the cytotoxicity behavior for HCSNs, doxorubicin loaded HCSNs and doxorubicin on cancer cells (A9549). Doxorubicin is used in the study due to its cytotoxic and cardiomyopathic nature (Havanur and JagadeeshBabu 2018). HCSNs samples did not cause any toxicity to the cancer cells; above 97 % of cells were viable. Death of cancer cells was found to increase when the concentration of doxorubicin loaded HCSNs increased. The percentage of viable cells reduced from 67 % to 16 % as the concentration of HCSNs was increased from 25 µg/ml to 200 µg/ml as shown in Figure 4.19b. But when doxorubicin alone was used at 200 µg/ml, 5% cell viability was observed.
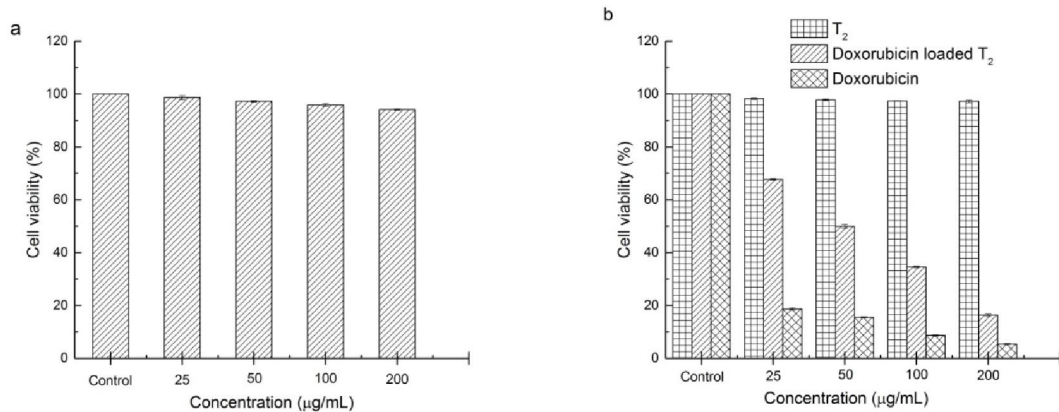
Figure 4.19 Cytotoxicity studies for sample T_2 on a) Normal cells (HEK 293T); b) Cancer cells (A549)

Part II

4.2 HCSNs synthesis from sulfonated PS template and application in targeted drug delivery

In this chapter, sulfonation of PS was carried out to improve the surface charge properties of PS. Sulfonated PS was used as a template to synthesize the HCSNs with enhanced thickness by modified Stober method. A detailed investigation was done to analyze the influence of sulfonated PS on variation of surface area and shell thickness of mesoporous HCSNs. Systematic study was conducted to determine the drug loading and release behavior in controlled form for HCSNs at different shell thicknesses. Cytotoxicity studies were done for HCSNs, doxorubicin loaded HCSNs and doxorubicin on lung adenocarcinoma (A549) cells.

4.2.1 Sulfonation of PS template

Sulfonation of PS nanoparticles was carried out by using different concentrations of sulfuric acid. During sulfonation, sulfonate group was formed on the surface of PS. Thus, presence of sulfonate group would alter the charge on the surface of PS which can be analyzed by using zeta potential analysis. The zeta potential of sulfonated PS was tabulated as given in Table 4.3. Concentration of sulfuric acid was varied as 1M, 5M, 10M and 17.9M during the sulfonation reaction carried out at 30 ^{0}C.

It was observed that dilute sulfuric acid was not effective in altering the surface charge properties. Negligible change in zeta potential was noticed when diluted sulfuric acid was used. However, when the sulfuric acid with a higher concentration of 17.9M was used, zeta potential was raised to -65±1.6 mV. Thus, concentrated sulfuric acid (17.9M) was used further for sulfonation of PS and the sulfonated PS were found to be pale yellow in color (Figure 4.20a). SEM image of the sulfonated PS particles confirmed that the nanoparticles hold the spherical and monodispersed morphology with size (160±20 nm) after sulfonation reaction. When concentrated sulfuric acid was used, the average particle size of 160 nm was obtained for sulfonated PS nanoparticles (Figure 4.20c).
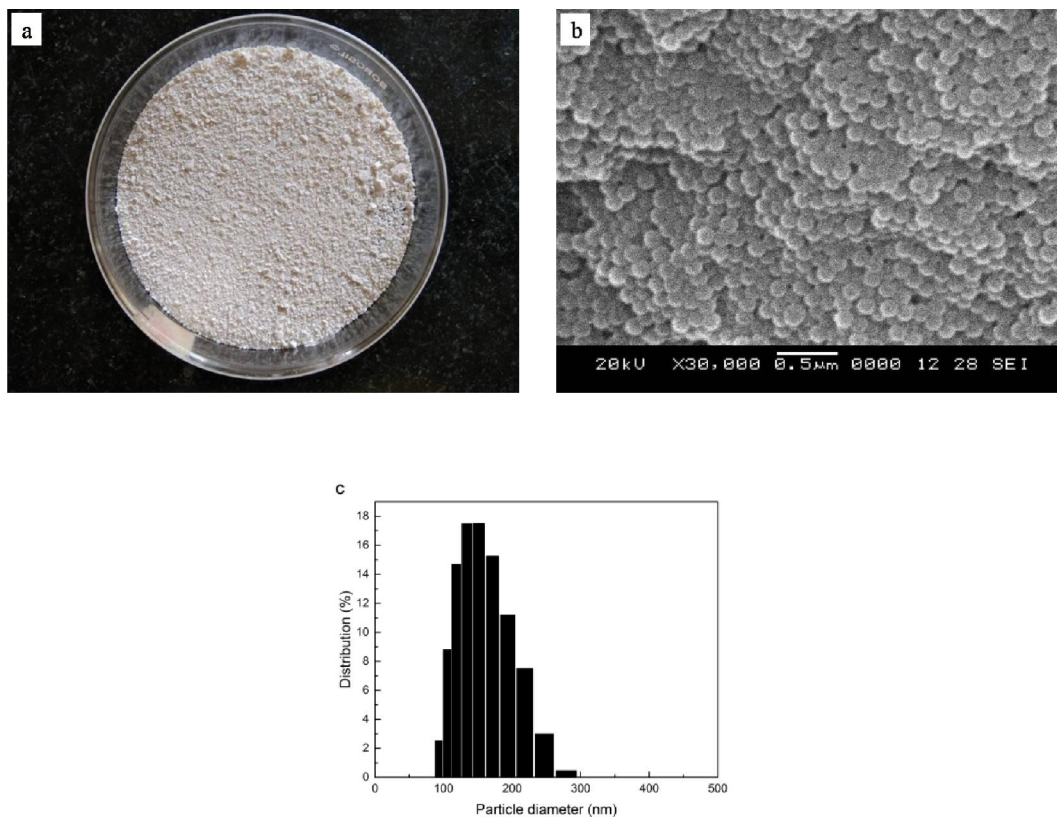
Figure 4.20 Sulfonation of PS at 17.9M sulfuric acid (C30) a) Image of sulfonated PS; b) SEM image of sulfonated PS; c) Particle size distribution for sulfonated PS

Table 4.3 Variation in zeta potential for sulfonated PS

Sample name	Sulfuric acid concentration (M)	Zeta potential (mV)
PS	0	-53.3±0.43
1M30	1	-55.8
5M30	5	-49.6
10M30	10	-45.7
C30	17.9	-65±1.6

4.2.2 Synthesis of HCSNs using sulfonated PS template and optimization

HCSNs were synthesized using sulfonated PS as the sacrificial template and the reaction parameters such as concentration of ammonia, concentration of CTAB and sulfonated PS/TEOS ratio were optimized.

Effect of concentration of ammonia:
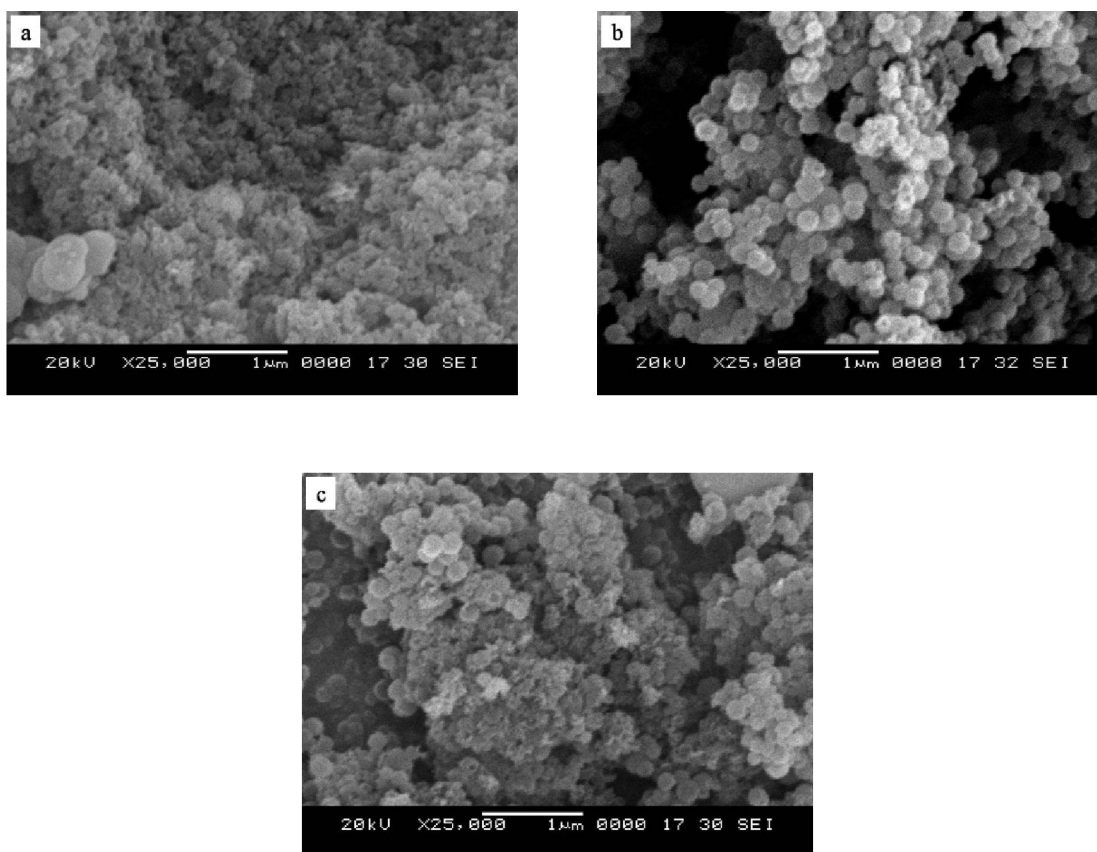
Figure 4.21 SEM images of HCSNs synthesized using sacrificial sulfonated PS template by variation of concentration of ammonia a) 0.3 mL; b) 0.5 mL; c) 0.7 mL (1:1 weight ratio of sulfonated PS/TEOS, 10 ml CTAB, 1:4 volume ratio of water/ethanol)

SEM images of HCSNs while the concentration of ammonia was varied from 0.3 mL to 0.7 mL are given in Figure 4.21. Formation of undesirable and agglomerated silica

particles was occurred at lower (0.3 mL) and higher (0.7 mL) concentrations of ammonia (Figure 4.21 a, c). 0.5 mL concentration of ammonia was found to be optimum to synthesize spherical monodispersed HCSNs using sacrificial sulfonated PS template (Deng et al. 2006; Yuan et al. 2010) (Figure 4.21 b).

Effect of concentration of CTAB:
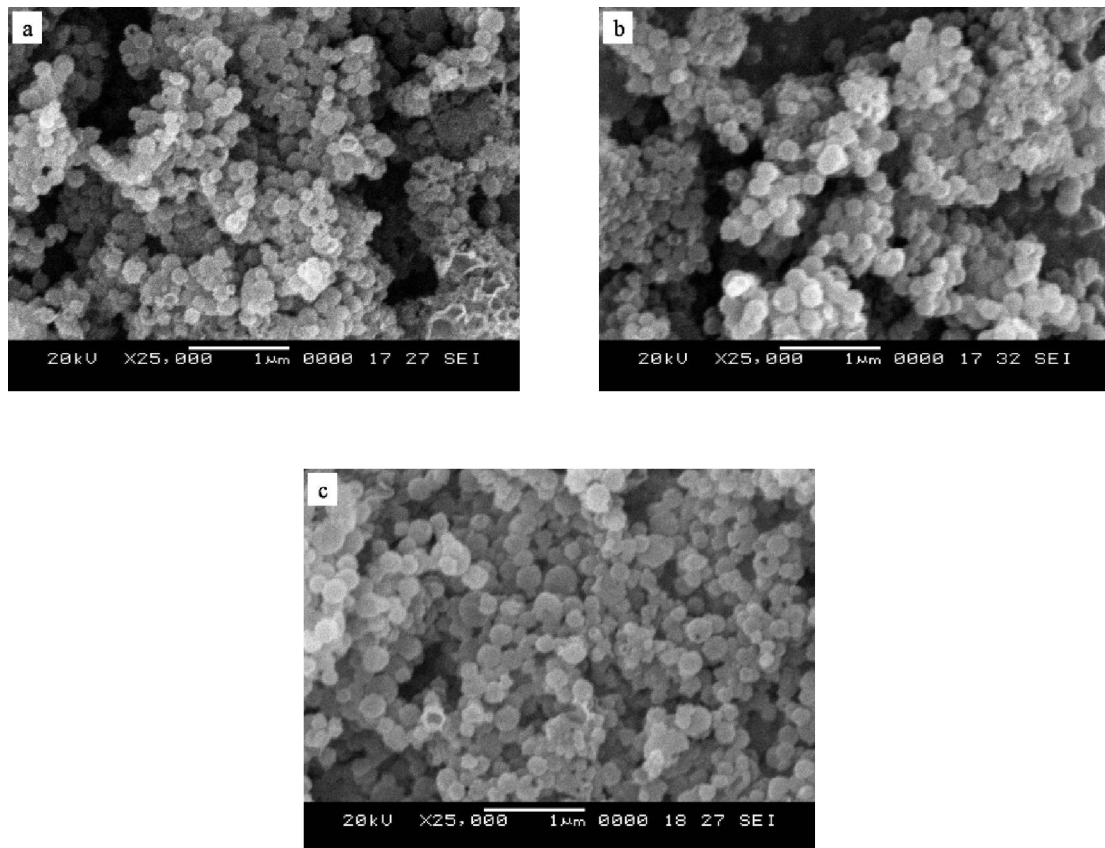
Figure 4.22 SEM images of HCSNs synthesized using sacrificial sulfonated PS template by variation of CTAB concentration a) 6 ml; b) 8 ml; c) 10 ml (1:1 weight ratio of sulfonated PS/TEOS, 0.5 mL ammonia, 1:4 volume ratio of water/ethanol)

CTAB performed as a surfactant during the synthesis of HCSNs (Chen et al. 2013). CTAB micelles were coupled with negatively charged PS in the presence of aqueous

ammonia solution. Composites of CTAB with sulfonated PS were generated via electrostatic interactions (Du and He 2008; Niu et al. 2010). When TEOS molecules were added, they were hydrolyzed and silica ions started to assemble with CTAB by self assembly leading to the growth of silica on the surface of the sulfonated PS particles (Liu et al. 2012; Zhang et al. 2014). SEM images of HCSNs synthesized at varying concentrations of CTAB are shown in Figure 4.22. 10 mL of CTAB concentration was found to be best for the synthesis of HCSNs with spherical structure (Figure 4.22c).

Effect of sulfonated PS/TEOS ratio: The concentration of silica precursor and enhanced surface charge of the sulfonated PS template played a key role in tuning the shell thickness of HCSNs. During the synthesis step of HCSNs, TEOS hydrolyzed and deposited on the surface of CTAB coated sulfonated PS. The thickness of silica shell was found to increase from 20 to 60 nm (Figure 4.23a-c), altering the ratio of sulfonated PS/TEOS from 1:1 to 4:7 as given in Table 4.4. When the concentration of TEOS was enhanced, an additional amount of silica deposited on the surface of sulfonated PS which enhanced the thickness of the shell (Chen et al. 2013).

Shell thickness of HCSNs synthesized using the sulfonated PS template was found to be higher, compared to that of HCSNs synthesized using the PS template (Table 4.1). This phenomenon had accounted for the increase in the attractive force between the positively charged CTAB and negatively charged silica ions. The presence of sulfonic acid group had enhanced the negative charge on the surface of PS as confirmed by zeta potential analysis which in turn, enhanced the deposition of CTAB on the surface of sulfonated PS. Thus, the higher thickness of silica shell was attained using sulfonated PS as a template. The silica shell thickness was found to increase with the increase in acidity of acidic functional group (Liu et al. 2011). Further increase in the concentration of TEOS (sulfonated PS/TEOS ratio of 1:2) lead to the evolution of undesirable free solid silica particles due to the fast rate of formation of silica as observed in Figure 4.23d. PS templates were found to be inadequate to capture all silica nanoparticles on the surface (Deng et al. 2006).
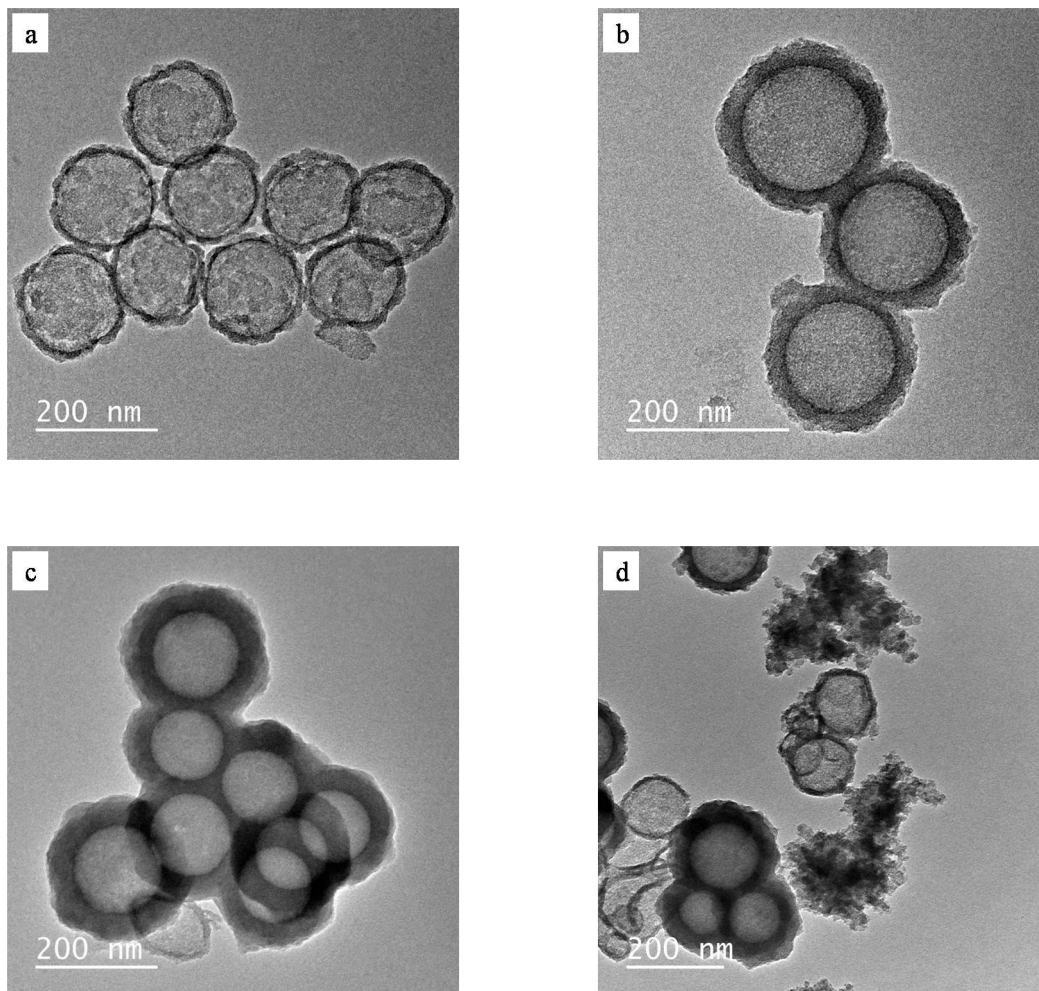
Figure 4.23 TEM images of HCSNs synthesized using sacrificial sulfonated PS template by sulfonated PS/TEOS weight ratio variation a) Ts_1; b) Ts_2; c) Ts_3 (10 ml CTAB, 0.5 mL ammonia, 1:4 volume ratio of water/ethanol)

Table 4.4 Variation of specific surface area and pore size with thickness of silica shell for samples Ts_1, Ts_2 and Ts_3

Sample	PS/TEOS ratio	Shell thickness (nm)	Average pore diameter (nm)	Specific surface area (m^2/g)
Ts_1	1:1	20	1.5	644.1
Ts_2	2:3	40	2.7	391.5
Ts_3	4:7	60	3.4	197.8

4.2.3 Structural and thermal analysis of HCSNs synthesized using sulfonated PS

N_2 adsorption/desorption studies were performed on HCSNs with varied shell thicknesses (Ts_1, Ts_2 and Ts_3) as shown in Figure 4.24. The N_2 adsorption/desorption isotherms displayed a type-IV curve, indicating the mesoporous nature of shell with the hollow internal cavity (Jiao et al. 2012; Li et al. 2013; Zhou et al. 2014). Hysteresis was noticed at the relative pressure range from 0.4 to 1 for samples Ts_1, Ts_2 and Ts_3 (Figure 4.24). The nature of hysteresis loop agreed with H4 type as observed from the BET isotherms (Thommes et al. 2015).

The average pore sizes were determined by using the BJH method which were found to vary from 1.5 to 3.4 nm with the increase in shell thickness from 20 to 60 nm (Table 4.4). The specific surface area of HCSNs was found to reduce from 644.1 to 197.8 m^2/g with the increase in shell thickness of silica from 20 to 60 nm. When the concentration of TEOS was increased, thickness of the silica shell also increased due to deposition of more number of silica particles on the shell quickly. Thus, the rapid condensation of silica particles on the surface occurred which had led to the formation of less rigid network of silica particles with a higher pore size of 3.4 nm. XRD analysis result also confirmed the presence of silica nanoparticles as the characteristic diffraction peak of silica occurred at ~23^0 (Figure 4.24d) (Nguyen et al. 2014).
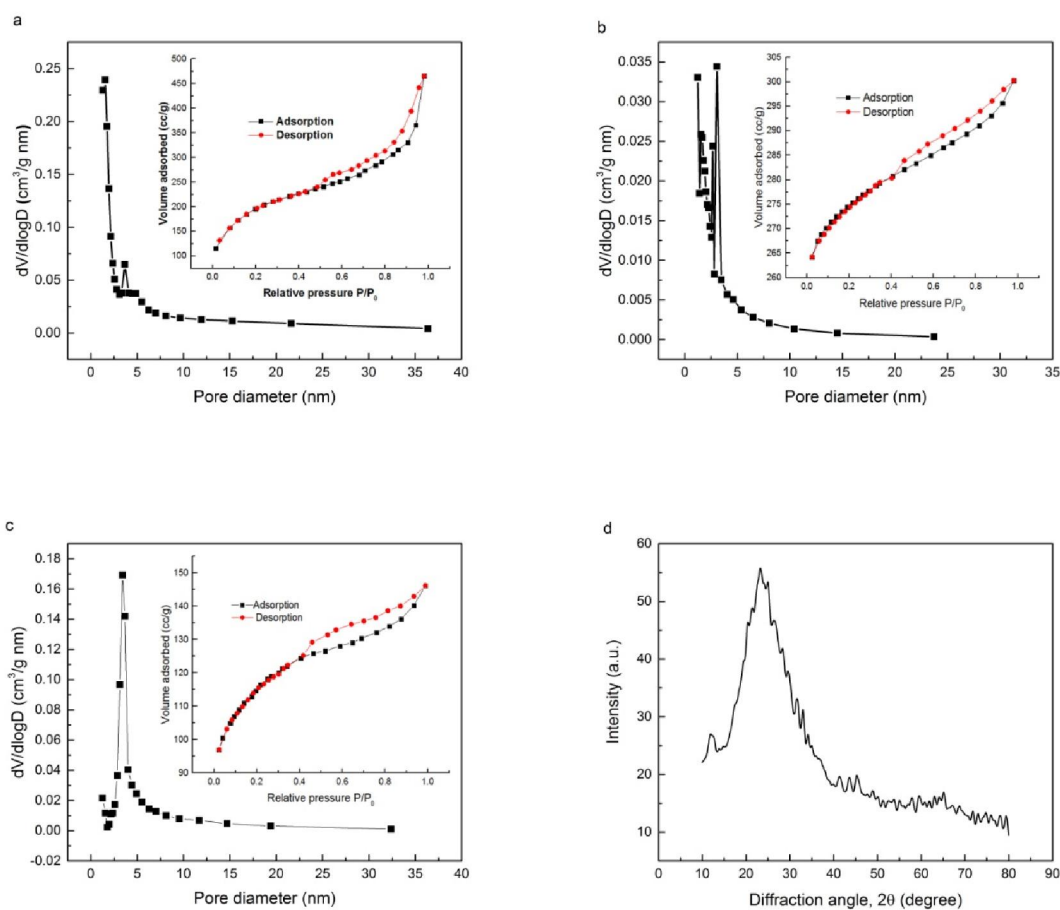
Figure 4.24 Nitrogen adsorption/desorption isotherm and pore size distribution for HCSNs samples a) Ts_1; b) Ts_2; c) Ts_3; d) XRD analysis of HCSNs

FTIR absorption spectra of sulfonated PS and HCSNs are presented in Figure 4.25. Sulfonation of PS is confirmed by the occurrence of the strong absorption band at 1170 cm^{-1} (Figure 4.25a) corresponding to the sulfonic group (-SO$_3$H) (Liu et al. 2011; Yang et al. 2006). The peaks at 696 and 756 cm^{-1} have corresponded to vibrations (C-H) of the benzene ring and those at 1493, 1450 and 1600 cm^{-1} have attributed to the vibrations of benzene ring (C-C) of sulfonated PS (Ding et al. 2004; Zhang et al. 2012b) (Figure 4.25a). Sequence of absorption bands comprising of 1093 and 800 cm^{-1} belong to Si-O-Si asymmetric and symmetric stretching vibration. Presence of silanol groups (Si-OH) on

the surface is confirmed by the peak at 962 cm^{-1}. The oxygen deformation vibration (Si-O-Si) is observed from the band at 460 cm^{-1} (Varga et al. 2015). The bands due to alkyl groups have vanished in HCSNs in the range of 2850-3062 cm^{-1} which agreed with the complete removal of sulfonated PS core during the process of calcination (Nandiyanto et al. 2009).
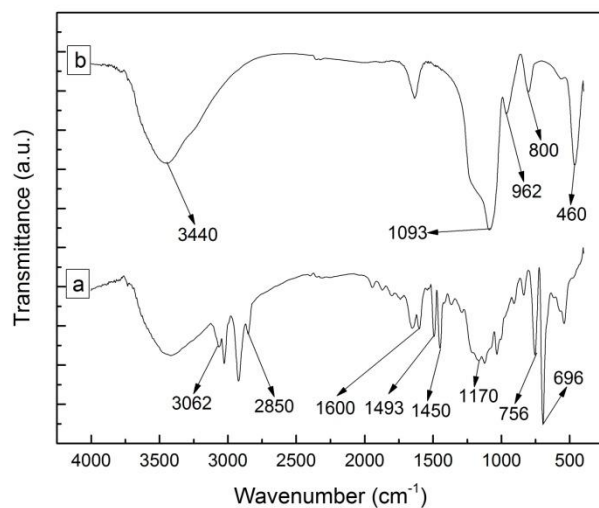
Figure 4.25 FTIR spectra of a) sulfonated PS; b) HCSNs

TGA analysis was done to determine the thermal stability of the synthesized nanoparticles. TGA curves for sulfonated PS and HCSNs are represented in Figure 4.26. The weight loss observed at lower temperatures, i.e. below 100 ^{0}C was due to the evaporation of water absorbed on the surface of the particle (Zou et al. 2008). Sulfonated PS displayed a quick drop at ~340 ^{0}C and no weight loss was observed above 550 ^{0}C. Thus, the absence of any remenant sulfonated PS particles along with silica was confirmed at higher temperatures (>550 ^{0}C). The TGA graph of silica did not show any decomposition after 100 ^{0}C which confirmed the absence of any polymer template residue in the HCSNs (Figure 4.26).
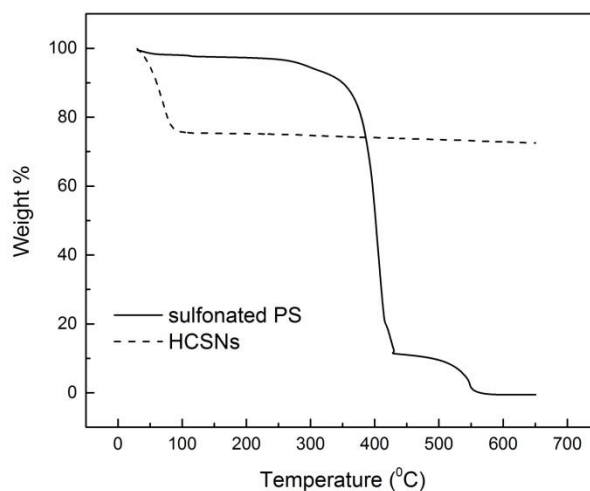
Figure 4.26 TGA plot for sulfonated PS and HCSNs

4.2.4 Formation of HCSNs using sacrificial sulfonated PS template

Surface of the sulfonated PS template was negatively charged due to the presence of sulfonic acid group confirmed by FTIR analysis. Surface of sulfonated PS was coated employing cationic surfactant CTAB by electrostatic force. CTAB acted as a major ingredient in the formation of HCSNs. Self assembly of TEOS on sulfonated PS was guided by CTAB. Further, TEOS was allowed to hydrolyze in the basic condition forming siliceous micelles with negative charge. Calcination of silica coated sulfonated PS lead to the formation of HCSNs and complete removal of polymer template. Higher thickness of silica shell was achieved while sulfonated PS template was used (Ge et al. 2009; Liu et al. 2011). Schematic representation of evolution of HCSNs is represented in Figure 4.27.
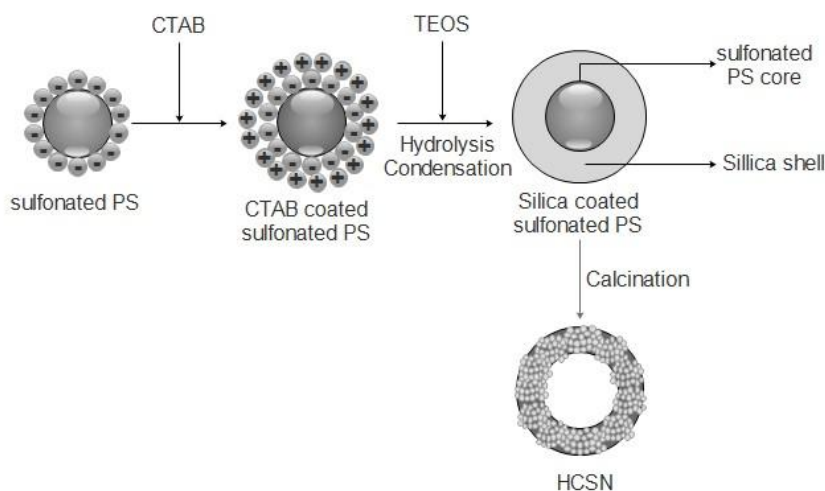
Figure 4.27 Schematic representation of synthesis of HCSNs using PS template

4.2.5 Loading and release studies using HCSNs synthesized using sacrificial sulfonated PS template

The loading capacities of samples Ts_1, Ts_2 and Ts_3 were calculated according to equation 4 and were found to be 1.31, 1.11 and 1.06 wt% respectively. Since the core sizes of HCSNs were nearly same, similar values of loading capacities were observed. Encapsulation efficiencies were determined using equation 5 for samples Ts_1, Ts_2 and Ts_3 were found to be 45.4, 39.1 and 37.4 wt% respectively. The decrease in encapsulation efficiencies of samples Ts_1, Ts_2 and Ts_3 could be due to the reduction in specific surface area of samples from 644.1 to 197.8 m^2/g (Mohamed El-Toni et al. 2012). The reduction in specific surface area could be due to the reduction in number of surface pores with increase in the thickness of silica shell, when sulfonated PS was used as the template.

The cumulative doxorubicin release plot of HCSNs samples synthesized using PS template and sulfonated PS template is shown in Figure 4.28. The drug release mechanism for rigid mesoporous systems was noted to be diffusion controlled (Maria et al. 2012). Initial burst release of drug upon contact with phosphate buffer was high for sample with the lowest thickness of 20 nm (Ts_1). However sample Ts_3 with the highest

thickness showed minimum burst release than the other samples (Bouchoucha et al. 2016). The rapid release of the drug occurred during the initial 15 minutes has accounted for the discharge of drug particles present on the surface and pore entrances of HCSNs (Ayad et al. 2016). After 1 hour, the percentage cumulative release of doxorubicin reached 49.1 %, 43.8 % and 35.2 % for samples Ts_1, Ts_2 and Ts_3 respectively.
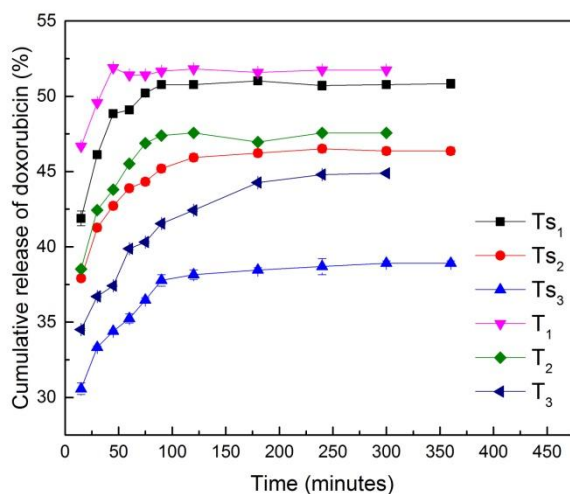
Figure 4.28 Cumulative release of doxorubicin from HCSNs of varying thickness synthesized using PS template and sulfonated PS template (Ts_1, Ts_2 and Ts_3)

Higher rate of doxorubicin release for sample Ts_1 and the lowest rate of doxorubicin release for sample Ts_3 were noticed. The influence of average specific surface area of HCSNs and thickness of the silica shell on the drug release rate was the prominent reason behind the variation in the doxorubicin release for HCSNs samples (Ts_1, Ts_2 and Ts_3). Sample Ts_1 exhibited the highest specific surface area and lowest thickness (Table 1) which had shorter mesopore length which had caused the rapid release of doxorubicin. However, a reduced release rate was observed for sample Ts_3, which had the lowest specific surface area and highest thickness (Table 4.4) (Jiao et al. 2012; Mohamed El-Toni et al. 2012). Further, the steady release of drug was observed for 300 minutes as shown in Figure 4.28. HCSNs samples synthesized using PS template found to have a lower thickness (15-30 nm) and hence showed a steady release up to 200 minutes as

reported earlier. However, sample Ts_3 achieved greater delay in the initial burst and steady release of doxorubicin for prolonged time compared to other samples.
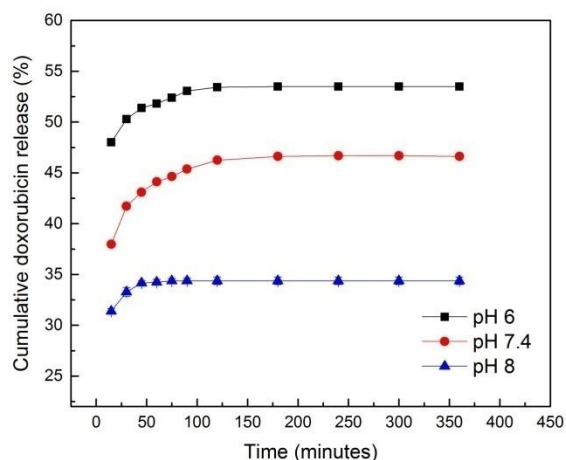
Figure 4.29 Cumulative doxorubicin release profile for HCSNs at different pH (6, 7.4 and 8) for sample Ts_2

The dependency of drug release on the pH of the release medium (phosphate buffer) was studied on sample Ts_2. The plot of cumulative drug release versus time is given in Figure 4.29 at pH of 6, 7.4 and 8. Low rate of drug release was observed at higher pH of 8, as the solubility of doxorubicin decreased at a higher pH (Mhlanga and Ray 2015). At pH 6, higher drug release (48 % in 15 minutes) was seen. Quantity of drug released at pH 6 was found to be higher than that at pH 7.4 (Jiao et al. 2012).

4.2.6 Mathematical modeling of drug release from HCSNs synthesized using sulfonated PS template for HCSNs

The cumulative doxorubicin release studies were carried out in phosphate buffer at pH 7.4 as given in Figure 4.28. Models used to study the drug release behavior are zero order, first order and Higuchi models. The drug release pattern is analyzed with these models and graphs are shown in Figure 4.30. Doxorubicin release was analyzed based on the regression coefficient R. Table 4.5 summarizes the regression coefficient R and values of constants K_0, K_1 and K_2. The drug release from the HCSNs was found to show

best fit for first order model. Thus, the release of doxorubicin from the samples was controlled by the amount of drug spared in the HCSNs (Varga et al. 2014).
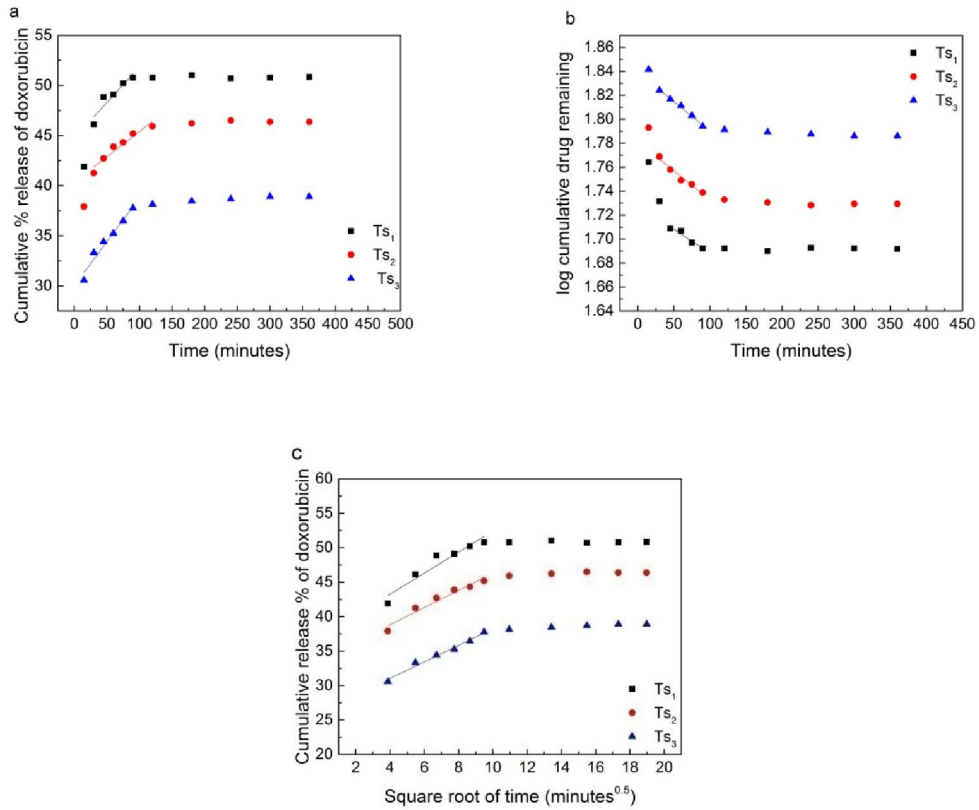
Figure 4.30 Doxorubicin release kinetics for samples Ts_1, Ts_2 and Ts_3 a) Zero order; b) First order; c) Higuchi model

Table 4.5 Correlation coefficients of mathematical models for samples Ts_1, Ts_2 and Ts_3

Sample name	Zero order		First order		Higuchi model	
	K_0	R^2	K_1	R^2	K_2	R^2
Ts_1	0.071	0.879	0.91×10^{-3}	0.950	1.527	0.916
Ts_2	0.050	0.931	1.11×10^{-3}	0.966	1.243	0.952
Ts_3	0.088	0.960	1.13×10^{-3}	0.993	1.201	0.939

4.2.7 Cytotoxicity studies for HCSNs synthesized using sulfonated PS template
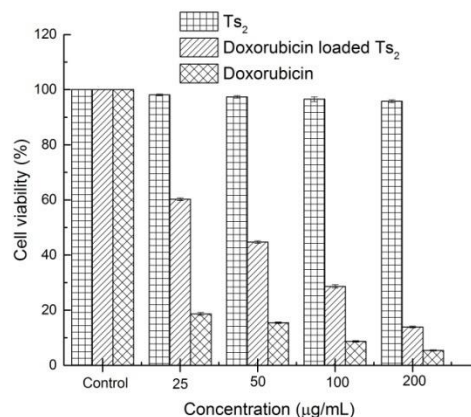
Figure 4.31 Cytotoxicity studies for sample Ts_2 on Cancer cells (A549)

Cytotoxicity studies were conducted for HCSNs by MTT assay method using lung adenocarcinoma (A549) cells. When the concentration of samples were increased from 25 μg/ml to 200 μg/ml, toxicity showed by HCSNs samples was significantly less (1.9-4.2%) as observed from Figure 4.31. Doxorubicin loaded HCSNs samples caused the death of cancer cells was proved by the decrease in cell viability from 60.2 to 13.9 % as the concentrations of the samples were increased. However, while doxorubicin alone used in the cytotoxicity study showed a slightly higher cell death (5.4% cells viable at the concentration of 200 μg/ml).

Part III

4.3 HCSNs synthesis by using sacrificial nitrated PS template and application in targeted drug delivery

Nitrated PS nanoparticles were synthesized by nitration of PS nanoparticles. Nitrated PS nanoparticles with enhanced surface charge were used as template for the synthesis of HCSNs with higher pore size and higher encapsulation efficiency of drug. HCSNs were loaded with doxorubicin and release behavior was monitored for HCSNs with tunable thickness. Release studies were also performed by varying pH of the release medium-phosphate buffer; since tumor micro-environment in a body becomes more acidic relative to normal tissue.

4.3.1 Nitration of PS template

The nitration of PS was carried out by varying the ratio between nitric acid and sulfuric acid as given in Table 4.6. Zeta potential was found to be maximum when the ratio of sulfuric acid and nitric acid (15.14 M nitric acid, 17.9 M sulfuric acid) was maintained at 2:3 (Wang et al. 2013) (Table 4.6). Further, nitrated PS nanoparticles were synthesized by keeping the ratio of nitric acid and sulfuric acid at 2:3. SEM images of PS and nitrated PS (at 2:3 ratio) were shown in Figure 4.32b. The average particle size of nitrated PS was found to be 170±20 nm. Nitrated PS nanoparticles exhibited slightly agglomerated nature, after functionalization with the nitro group.
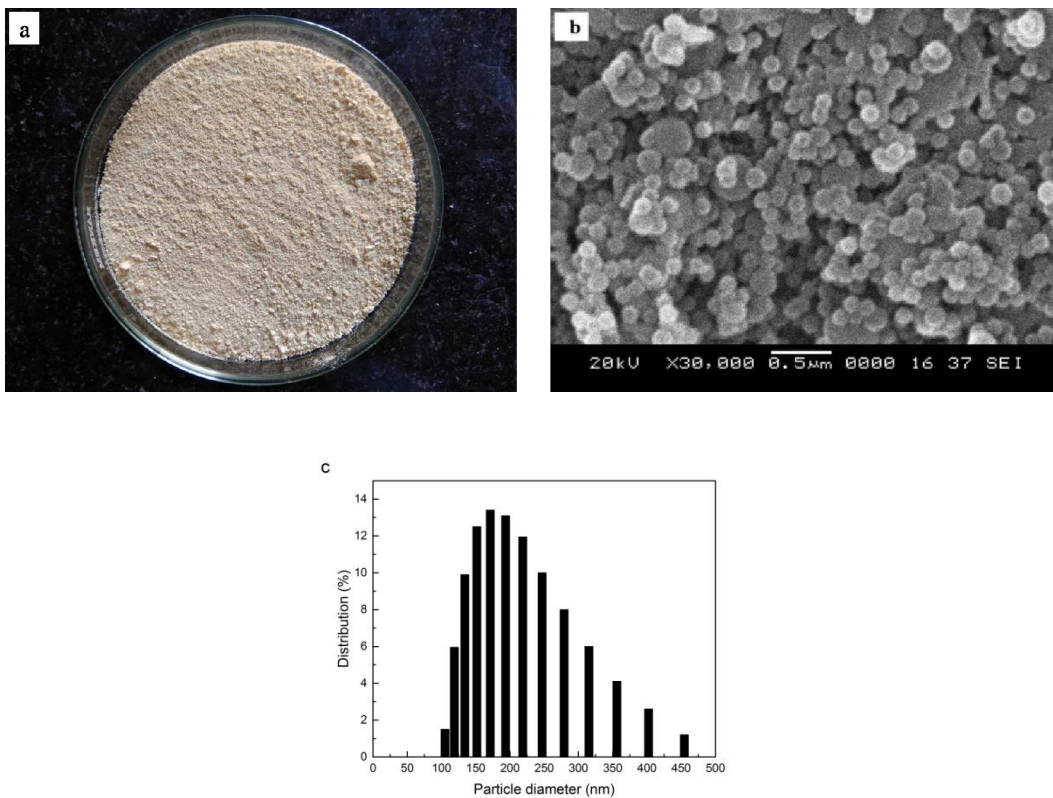
Figure 4.32 Nitration of PS at nitric acid and sulfuric acid kept at a ratio of 2:3 a) Image of nitrated PS; b) SEM image of nitrated PS; c) Particle size distribution for nitrated PS; d) Zeta potential plot for nitrated PS

Table 4.6 Zeta potential for nitrated PS

Sample name	Nitric acid (ml)	Sulfuric acid (ml)	Nitric acid sulfuric acid volume ratio	Zeta potential (mV)
PS	0	0	-	-52.6
S_1	4	6	2:3	-56.8±0.8
S_2	4.8	3.2	3:2	-47.9
S_3	3.2	6.4	1:2	-42.4

4.3.2 Synthesis of HCSNs using nitrated PS template and optimization

Effect of ammonia concentration:
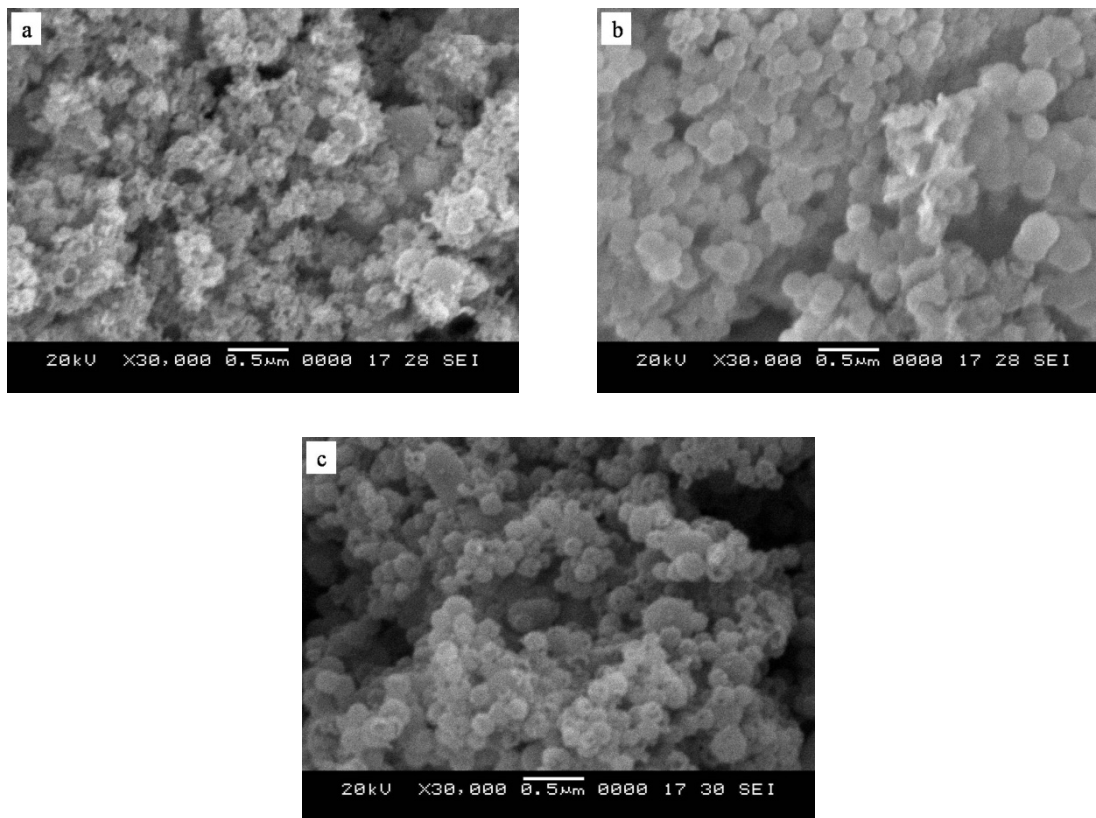
Figure 4.33 SEM images of HCSNs synthesized using sacrificial nitrated PS template by variation of concentration of ammonia a) 0.3 mL; b) 0.5 mL; c) 0.7 mL (1:1 weight ratio of PS/TEOS, 6 ml CTAB, 1:4 volume ratio of water/ethanol)

Concentration of ammonia was altered from 0.3 to 0.7 mL. The SEM images of HCSNs synthesized by varying ammonia concentrations are shown in Figure 4.33. The HCSNs synthesized at higher concentrations of ammonia were found to be broken which might be due to the dissolution of polymer template in ammonia. The hydrolysis of TEOS to form silica coating on the nitrated PS would be relatively fast which lead to the formation of random shaped HCSNs (Figure 4.33c) (Deng et al. 2006). However, lower concentrations of ammonia were not found to be sufficient to obtain HCSNs with a

spherical shape, due to the lower rate of hydrolysis of TEOS (Figure 4.33a) (Yuan et al. 2008). 0.5 mL of ammonia was found to be the optimum concentration for the synthesis of HCSNs.

Effect of CTAB concentration: The effect of variation of concentration of CTAB is shown in Figure 4.34. CTAB acted as the binding agent which allowed the self assembly of silica micelles on the surface of nitrated PS nanoparticles (Chen et al. 2013; Ge et al. 2009). HCSNs with spherical morphology were obtained at a CTAB concentration of 6 mL.
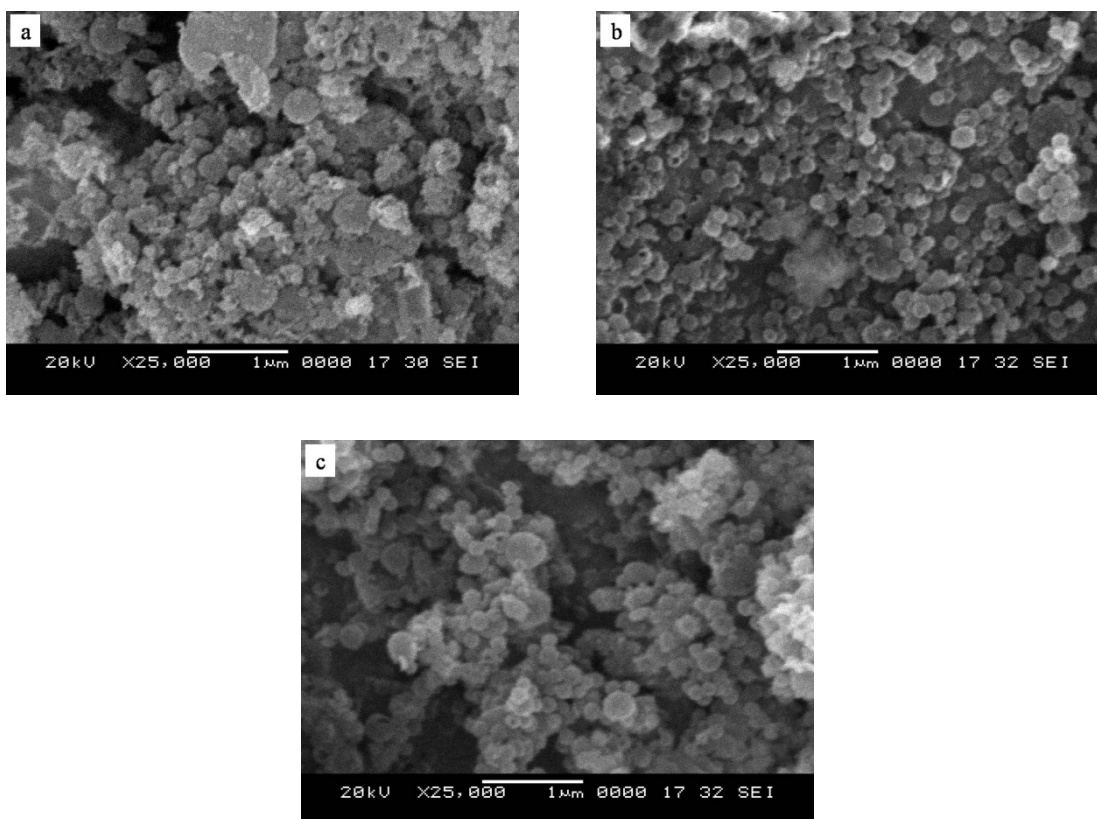
Figure 4.34 SEM images of HCSNs synthesized using sacrificial nitrated PS template by variation of CTAB concentration a) 2 ml; b) 6 ml; c) 10 ml (1:1 weight ratio of PS/TEOS, 0.5 mL ammonia, 1:4 volume ratio of water/ethanol)

Effect of variation of PS/TEOS ratio: Quantity of TEOS was increased to tune the thickness of the silica shell from 15 nm to 35 nm, while the PS/TEOS ratio was varied from 1:1 to 4:7 as given in Table 4.6. HCSNs were observed under TEM and the images showed the presence of hollow core and a thick shell structure with size of 220±50 nm (Figure 4.35).
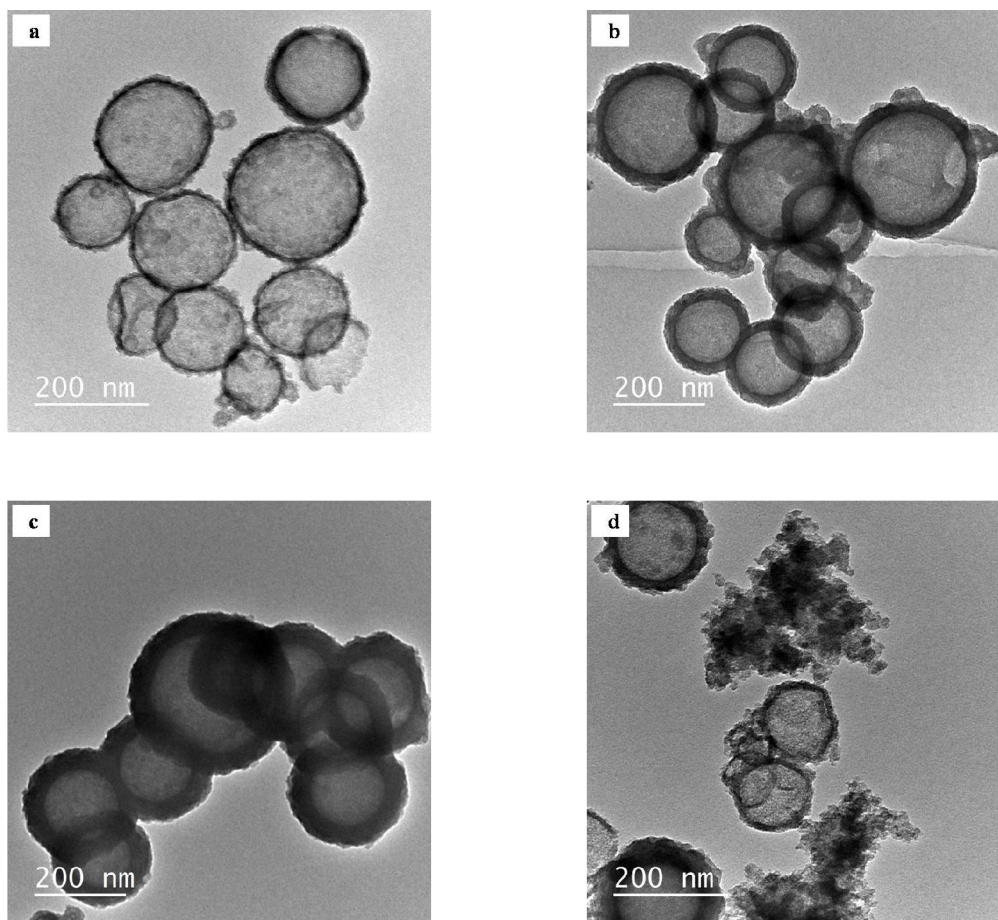
Figure 4.35 TEM images of HCSNs synthesized using sacrificial nitrated PS template by PS/TEOS weight ratio variation a) 1:1; b) 2:3; c) 4:7; d) 1:2 (6 ml CTAB, 0.5 mL ammonia, 1:4 volume ratio of water/ethanol)

There was an enhancement in the shell thickness of silica with an increase in the concentration of TEOS as a result of the deposition of higher amount of silica particles on

the surface of nitrated PS (Niu et al. 2010). Variation in thickness of the silica shell is observed from the TEM images as shown in Figure 4.35a-c. However, there was formation of secondary silica particles as the concentration of TEOS was enhanced with PS/TEOS ratio of 1:2 (Fig. 4.35d) (Deng et al. 2006).

Table 4.7 Variation of average specific surface area with thickness of silica shell for samples Tn_1, Tn_2 and Tn_3

Sample Name	PS/TEOS ratio	Thickness (nm)	Average specific surface area (m^2/g)	Average pore diameter (nm)
Tn_1	1:1	15	533.6	2.6
Tn_2	2:3	20	291.9	3.4
Tn_3	4:7	35	130.5	3.7

4.3.3 Structural and thermal analysis of HCSNs synthesized using sacrificial nitrated PS template

To analyze the pore size and surface area of HCSNs, BET analysis was done. The N_2 adsorption/desorption isotherms for samples Tn_1, Tn_2 and Tn_3 are displayed in Figure 4.36. The specific surface area of HCSNs was varied from 533.6 m^2/g to 130.5 m^2/g for increase in thickness from 15 nm to 35 nm as calculated by BET method (Table 4.7). The N_2 adsorption/desorption isotherm followed type 4 isotherm for all the samples (Tn_1, Tn_2 and Tn_3) showing hysteresis at a relative pressure (P/P_0) range from 0.4 to 1. Type 4 isotherms are characteristic of particles with mesoscale pores and hollow cavity (Huh et al. 2003; Zhou et al. 2014). The isotherms indicated the presence of H4 type hysteresis which confirmed the existence of the mesopores in the silica shell (Thommes et al. 2015; Zhang et al. 2014). Average pore sizes were determined by BJH method which was found to be from 2.6 nm to 3.7 nm. Pore sizes of HCSNs were found to increase by the use of nitro functionalized PS as a template.

86
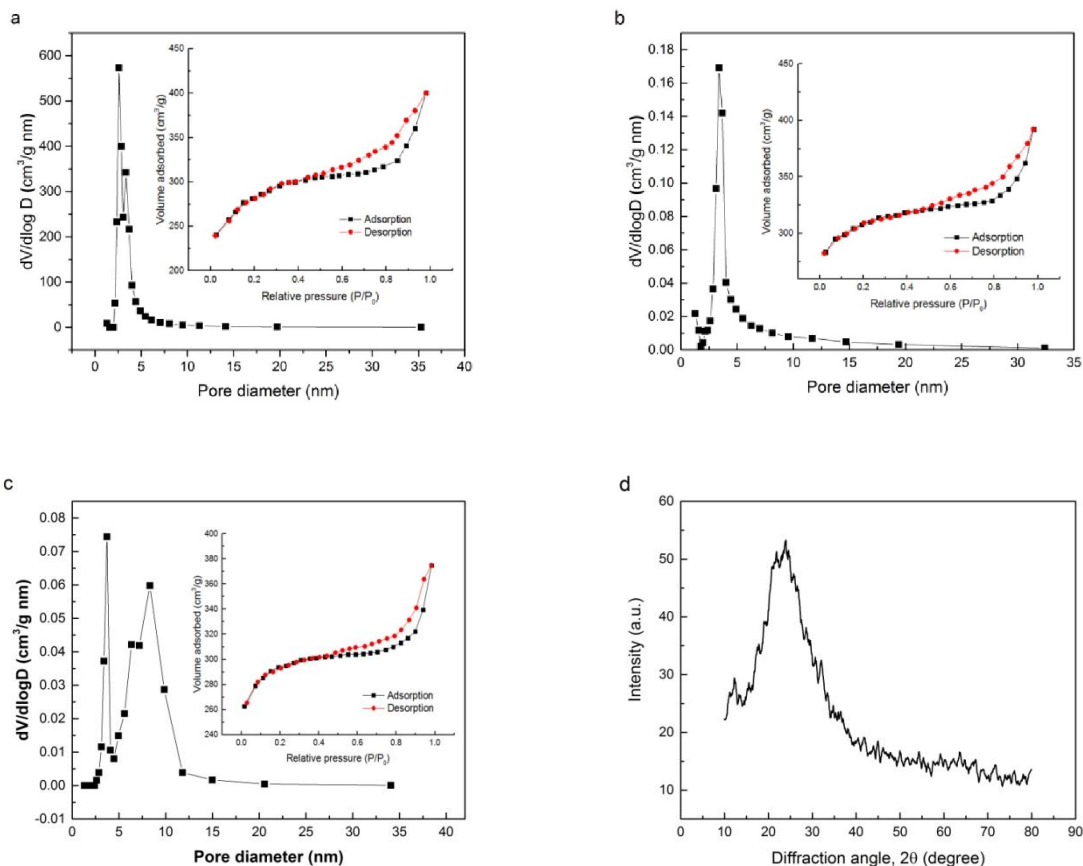
Figure 4.36 Nitrogen adsorption/desorption isotherm and pore size distribution for HCSNs samples a) Tn_1; b) Tn_2; c) Tn_3; d) XRD analysis of HCSNs

The FTIR analysis was carried out for nitrated PS and HCSNs (Figure 4.37). Two characteristic FTIR bands at 1348 and 1520 cm^{-1} confirmed the nitro group in the nitrated PS (Wang et al. 2013). Absolute removal of the polymer was assured by the absence of alkyl groups in the HCSNs in the range 3064-2850 cm^{-1}, after calcination of silica coated nitrated PS samples. The presence of absorption bands at 798 and 1090 cm^{-1} have contributed to Si-O-Si symmetric and asymmetric vibrations. The broad absorption band around 3440 cm^{-1} is due to the presence of silanol groups (Liu et al. 2011; Nandiyanto et al. 2009).
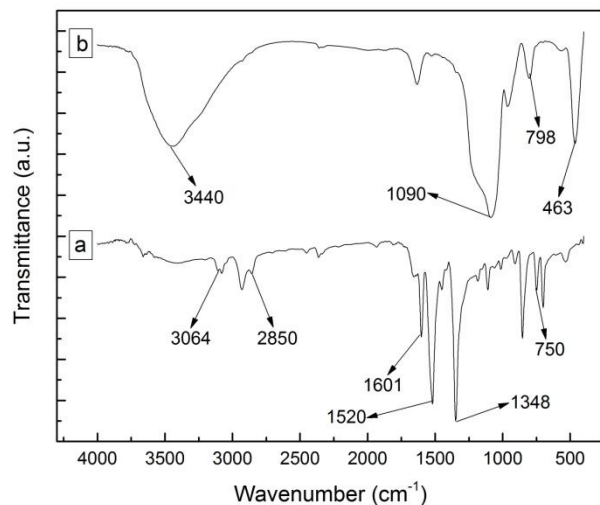
Figure 4.37 FTIR spectra of a) nitrated PS; b) HCSNs
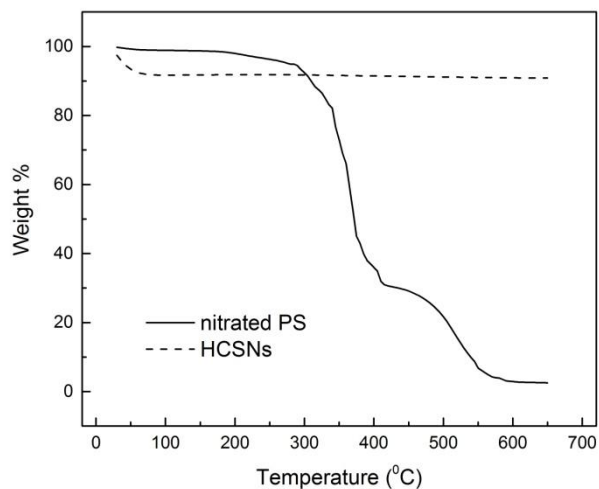
Figure 4.38 TGA plot for nitrated PS and HCSNs

The TGA plot of PS, nitrated PS and HCSNs is shown in Figure 4.38. Initial weight loss noticed at temperature <100 ^{0}C was due to the evaporation of the moisture present on the surface of the particles (Yuan et al. 2010). Nitrated PS showed a rapid drop in weight %

above 350 ^{0}C due to the breakage of polymer backbone and there was no remarkable loss in weight at temperatures above 550 ^{0}C. TGA plot of HCSNs exhibited no weight reduction at temperatures above 100 ^{0}C.

4.3.4 Formation of HCSNs using sacrificial nitrated PS template

Formation of HCSNs using nitrated PS as sacrificial template could be proposed using the electrostatic interaction between the nitrated PS and the CTAB molecules. A Schematic representation of synthesis of HCSNs using nitrated PS template is shown in Figure 4.39. When CTAB was added to the dispersion containing nitrated PS, CTA+ ions get coated on the polymer surface due to the electrostatic interaction of CTA+ with nitrated PS. In the next step, TEOS was added as silica precursor which formed negatively charged silica ions. Further, electrostatic interaction between the CTA+ and silica ions lead to the formation of silica particles on nitrated PS surface. Self assembly of negatively charged silica micelles with CTA+ coated nitrated PS occurred spontaneously (Chen et al. 2013; Ge et al. 2009). The core shell structure of silica nanoparticles with hollow interior was achieved upon complete removal of polymer particles by calcination.
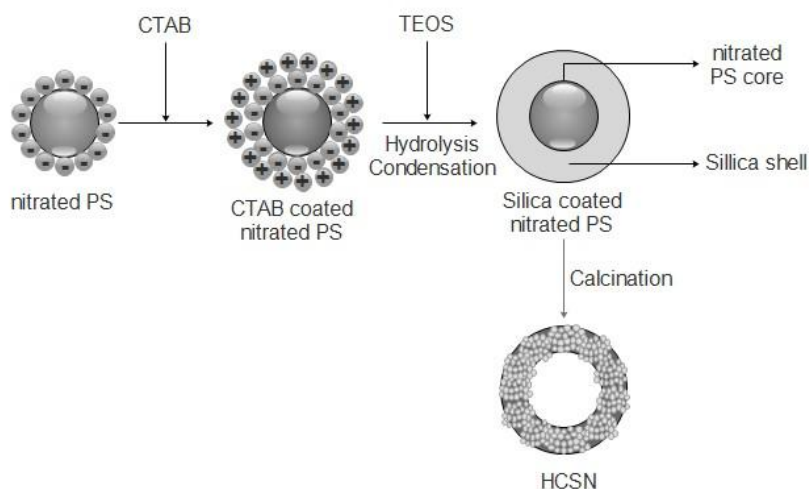
Figure 4.39 Schematic representation of synthesis of HCSNs using nitrated PS template

4.3.5 Loading and release studies using HCSNs synthesized using sacrificial nitrated PS template

To evaluate the ability of HCSNs as drug deliver vector, doxorubicin loading and release studies were carried out using HCSNs at different thicknesses (Tn_1, Tn_2 and Tn_3). The loading capacities and encapsulation efficiencies were calculated according to equation 4 and 5. Samples Tn_1, Tn_2 and Tn_3 exhibited mostly identical values of loading capacities such as 1.15, 1.09 and 1.08 % respectively due to the similar core sizes of HCSNs (Jiao et al. 2012). Encapsulation efficiencies of HCSNs samples (Tn_1, Tn_2 and Tn_3) were found to be high such as 38.5, 36.5, 36.2 %. HCSNs samples synthesized by using the PS template showed comparatively less encapsulation efficiencies (32-35%). Increment of encapsulation efficiency was achieved as the pore sizes of the samples increased when nitrated PS nanoparticles were used as a template. Encapsulation efficiency decreased as the surface area of samples reduced from 533.6 m^2/g to 130.46 m^2/g (Table 4.7).
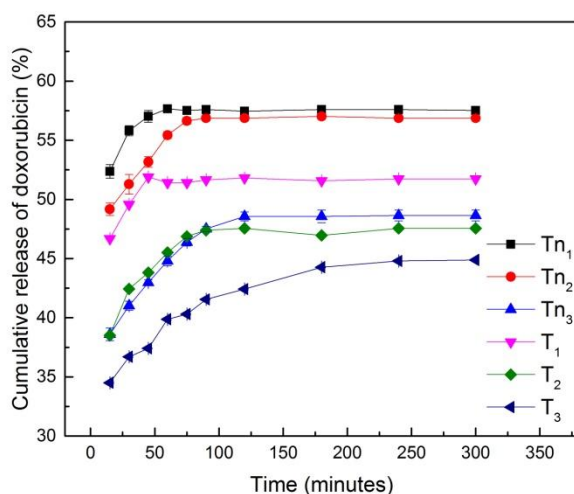
Figure 4.40 Effect of thickness of the silica shell on doxorubicin release for samples Tn_1, Tn_2 and Tn_3

A plot of percentage doxorubicin release with the time displayed an elevated initial release and steady release of drug for 250 minutes (Figure 4.40). The quick release of drug at initial 15 minutes was due to the liberation of drug present at the entrances of the

90

pores (Li et al. 2004). The sample Tn_3 showed slow release of doxorubicin (38.6% in 15 minutes), since the thickness of the shell was high (35 nm) and specific surface area was found to be 130.5 m^2/g. Hence, the longest mesochannel length and minimum specific surface area of Tn_3 allowed the slow release of drug from the core. In the contrary, sample Tn_1 exhibited rapid release (52.3% in 15 minutes) of doxorubicin due to the shortest mesochannel length (15 nm) and large surface area (Table 4.7) (Jiao et al. 2012; Mohamed El-Toni et al. 2012).

Release medium pH is one of the important parameters which affects the release of drug from the carrier (Mhlanga and Ray 2015). The effect of pH of phosphate buffer was studied for sample Tn_2 by maintaining pH of the release medium at 6, 7.4 and 8. The results of doxorubicin release show that at a higher pH of 8, poor solubility of doxorubicin was the primary cause of the lower release. At lower a pH of 6, the higher release of drug (54.2% in 15 minutes) was observed due to the higher solubility of doxorubicin. Figure 4.41 shows the cumulative release of doxorubicin with time by varying pH from 6-8. The drug release at pH 6 and 7.4 followed the similar trend as shown in the plot (Figure 4.41). Quantity of drug released at pH 6 was found to be higher than that at pH 7.4 (Jiao et al. 2012).
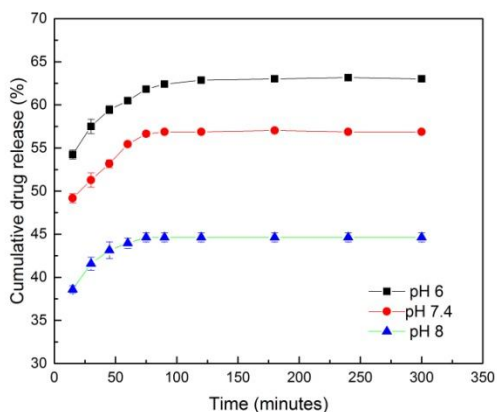
Figure 4.41 Effect of pH on doxorubicin release for sample Tn_2

4.3.6 Mathematical modeling of drug release from HCSNs synthesized using nitrated PS template for HCSNs

Models used to study the drug release behavior are zero order, first order and Higuchi models. The drug release pattern is analyzed with these models. The model graphs are shown in Figure 4.42 where the doxorubicin release was analyzed based on the regression coefficient R. Table 4.8 summarizes the regression coefficient R and values of constants K_0, K_1 and K_2. The drug release from the HCSNs had found to show the best fit with the first order model. Thus, the release of doxorubicin from the samples was controlled by the amount of drug remaining in the HCSNs. Other models did not provide R^2 >0.97 (Varga et al. 2014) (Table 4.8).
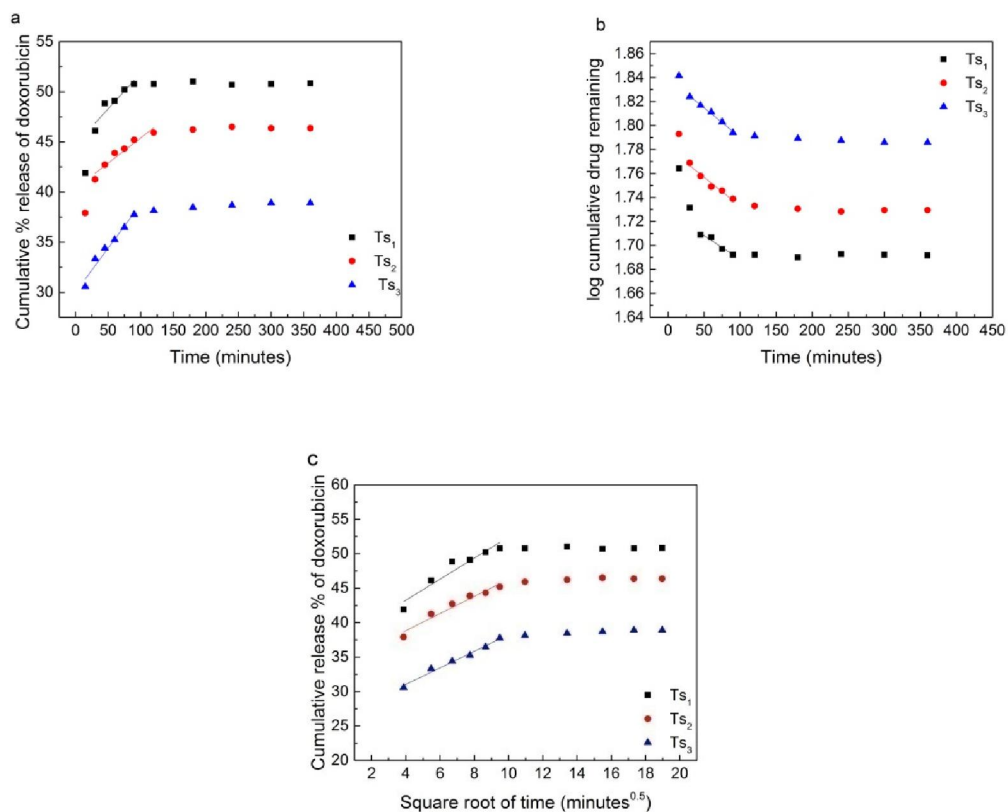
Figure 4.42 Doxorubicin release kinetics for samples Tn_1, Tn_2 and Tn_3 a) Zero order; b) First order; c) Higuchi model

Table 4.8 Correlation coefficients of mathematical models for samples Tn_1, Tn_2 and Tn_3

Sample name	Zero order		First order		Higuchi model	
	K_0	R^2	K_1	R^2	K_2	R^2
Tn_1	0.114	0.813	1.43×10^{-3}	0.971	1.366	0.898
Tn_2	0.127	0.993	2.57×10^{-3}	0.994	1.602	0.989
Tn_3	0.119	0.986	2.09×10^{-3}	0.991	1.434	0.971

4.3.7 Cytotoxicity studies for HCSNs synthesized using nitrated PS template

Cytotoxicity studies were performed for samples Tn_2, doxorubicin loaded Tn_2 and doxorubicin using lung adenocarcinoma (A549) cells. The concentrations of test samples were varied from 25 μg/ml to 200 μg/ml. The cell viability versus concentration of samples is given in Figure 4.43. The Tn_2 samples were found to be biocompatible from the cytotoxicity results; ~ 96 % cells were found to be viable when the concentration of sample Tn_2 was 200 μg/ml. The survival fraction of the cancer cells showed a gradual reduction from 64 % to 15 % as the concentration of doxorubicin loaded HCSNs increased (from 25 μg/ml to 200 μg/ml). Considerably higher death of cells was observed when doxorubicin alone was used in the cytotoxicity studies.
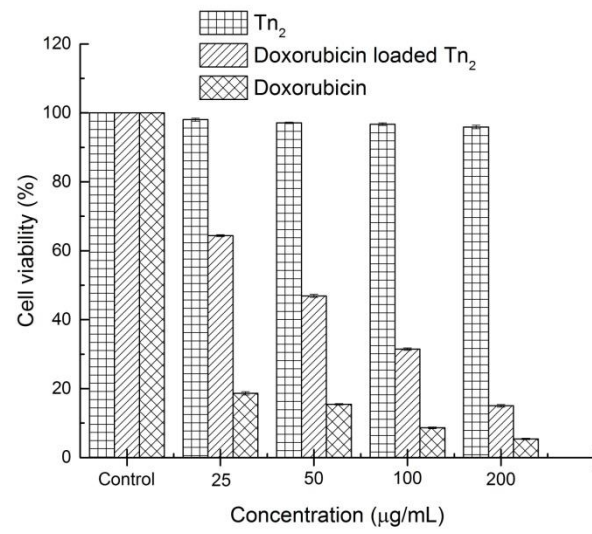
Figure 4.43 Cytotoxicity studies for sample Ts$_2$ on cancer cells (A549)

Part IV

4.4 Synthesis of SPION embedded HCSNs and application in targeted drug delivery

SPION embedded HCSNs were developed as targeted drug delivery vector by using a sacrificial PS template approach. Initially, PS was synthesized and coated with SPION and silica. The properties of synthesized SPION embedded HCSNs were studied to determine the drug loading and release behavior. Presence of SPION was an added advantage which aided in radiofrequency heating of the nanoparticles and allowed to study the variation of SPION concentration on the temperature. In vitro cytotoxicity studies were done by MTT assay using human embryonic kidney (HEK 293T) cells to determine the biocompatibility of SPION embedded HCSNs.

4.4.1 SPION embedded HCSNs synthesis

Figure 4.44 Image of SPION embedded HCSNs (T_{f2})

Figure 4.44 shows the image of SPION embedded HCSNs. SPION embedded HCSNs were synthesized by varying the concentration of the SPION from 5 mg to 30 mg. Images of the samples observed under SEM are shown in Figure 4.45a-c. Samples T_{f1}, T_{f2} and T_{f3} were found to be in uniform spherical shape. Thus, we concluded that, the morphology of HCSNs was not affected by increasing the concentration of SPION. To confirm the

formation of hollow core shell structure, sample T_{f2} was analyzed under TEM as shown in Figure 4.45d. SPION embedded silica nanoparticles showed the formation of hollow internal cavity and shell structure as shown in Figure 4.45d.
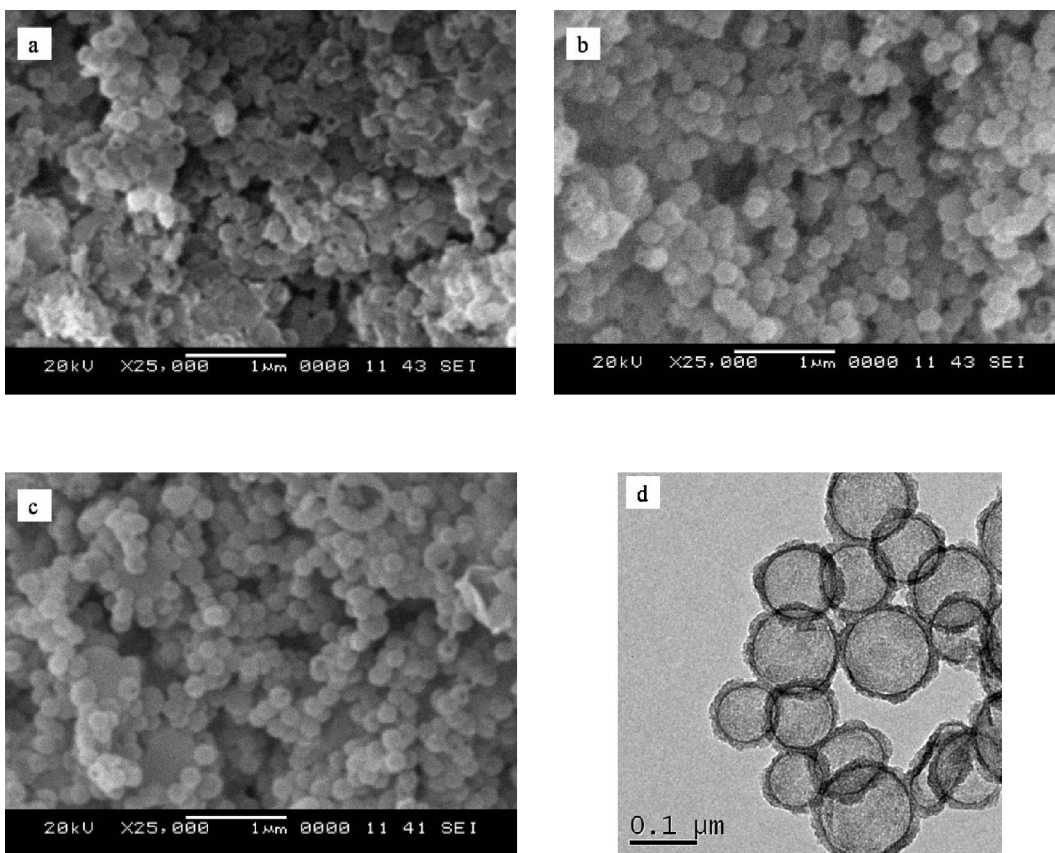
Figure 4.45 SEM images of the samples a) T_{f1}; b) T_{f2}; c) T_{f3}; d) TEM image of T_{f2}

4.4.2 Structural and thermal analysis of SPION embedded HCSNs synthesized using PS

Results of BET and BJH analysis carried out for SPION embedded HCSNs samples are shown in Figure 4.46a-c. The specific surface area of SPION embedded HCSNs was in the range from 406.3 to 527.1 m^2/g and the average pore size was found to be 8 nm. BET isotherms followed type 4 curves with the hysteresis present in the relative pressure range from 0.4 to 1 which confirmed the existence of hollow core structure with mesopores in

the silica shell (Zhang et al. 2014; Zhou et al. 2014). Table 4.9 summarizes the variation in the specific surface area while varying the concentration of SPION. XRD plot for SPION embedded HCSNs is shown in Figure 4.46d. The wide peak appeared at ~23^0 corresponded to the amorphous silica nanoparticles. The diffraction peaks from 30^0 to 70^0 such as [2 2 0], [3 1 1], [4 0 0], [4 4 0] and [5 1 1] confirmed the presence of iron oxide particles (Fe_3O_4) (Wu et al. 2007).
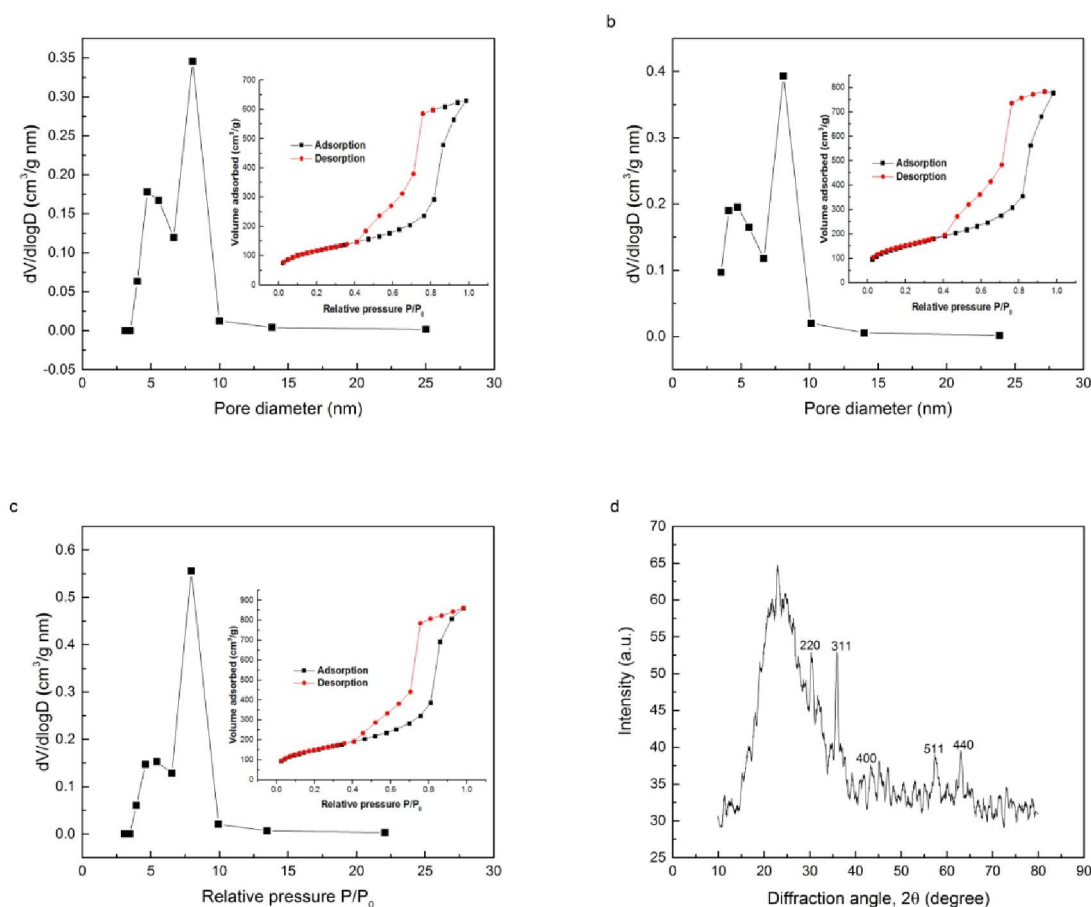
Figure 4.46 BET isotherms and pore size distribution plots for a) T_{f1}; b) T_{f2}; c) T_{f3}; d) XRD plot for SPION embedded HCSNs

Figure 4.47 shows the FTIR spectra of PS and SPION embedded HCSNs. The distinctive peaks at 700, 756, 1490, 1666 and 2850-3068 cm^{-1} in the FTIR spectrum, confirmed the

PS (Ding et al. 2004; Liu et al. 2011). In the FTIR spectra of SPION embedded HCSNs, the bands due to PS have disappeared. The adsorption bands at 464, 800 and 1081 cm^{-1} are characteristics of silica particles, from Si-O-Si vibrations. The peak at 3431 cm^{-1} contributed to the silanol group of silica particles (Nandiyanto et al. 2009; Zhang et al. 2012b). The presence of iron-oxygen bond (Fe-O) is confirmed by the absorption band appeared at 576 cm^{-1} (Hwang et al. 2014).

Table 4.9 Variation in specific surface area with variation in SPION concentration for SPION embedded HCSNs

Sample name	SPION (mg)	Pore diameter (nm)	Specific surface area (m^2/g)
T$_{f1}$	5	8.03	406.3
T$_{f2}$	10	8.09	525.3
T$_{f3}$	30	7.95	527.1

TGA was carried out for PS and SPION embedded HCSNs (Figure 4.48). The weight loss observed below 100 ^{0}C corresponded to moisture present on the surface of the particles (Yuan et al. 2010). The quick reduction in weight percentage above 350 ^{0}C was found in the TGA curve for PS and SPION embedded silica coated PS due to the fracturing of the polymer backbone. The weight loss observed at temperatures above 550 ^{0}C was found negligible.
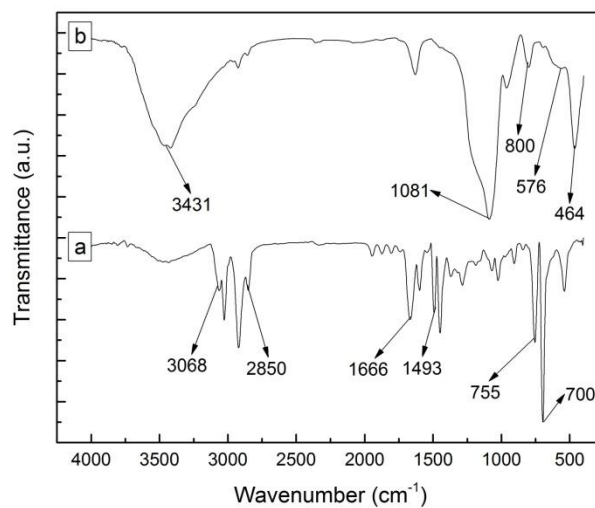
Figure 4.47 FTIR plot for a) PS; b) SPION embedded HCSNs
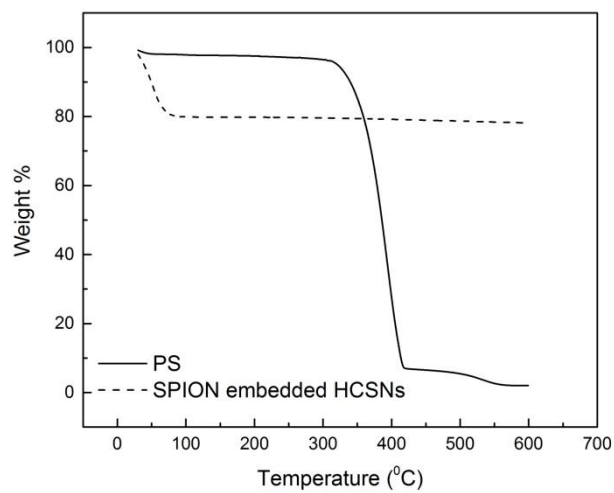
Figure 4.48 TGA plot for PS, SPION embedded HCSNs
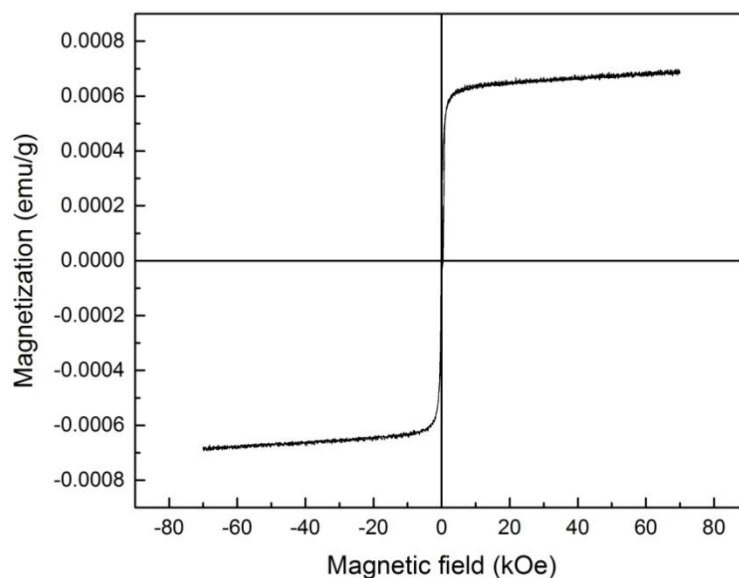
Figure 4.49 VSM analysis of SPION embedded HCSNs at 300 K

Figure 4.49 shows the VSM analysis result of SPION embedded HCSNs. The plot of magnetic field versus magnetization was carried out at 300 K. The characteristic nature of super paramagnetic particles is confirmed by the absence of hysteresis in the plot at 300K (Figure 4.49). Thus, there is no remnant magnetization after the removal of the magnetic field. The magnetization curve passes through the origin of magnetization versus magnetic field plot which indicated that when external field is zero the magnetization is also zero (Nalbandian et al. 2016) as shown in Figure 4.49.

4.4.3 Formation of SPION embedded HCSNs using sacrificial PS template

The formation of SPION embedded HCSNs using PS as sacrificial template is represented in Figure 4.50. The PS nanoparticles bound to CTAB particles through electrostatic interaction among negatively charged PS and positively charged CTA ions (Du and He 2008; Niu et al. 2010). Silica precursor (TEOS) formed silica ions after the process of hydrolysis. SPION and silica ions got coated on the surface of CTA-PS composite by the self assembly mechanism (Liu et al. 2012; Zhang et al. 2013). In the

100

final step, PS template was removed by the calcination as observed from FTIR and TGA analysis.
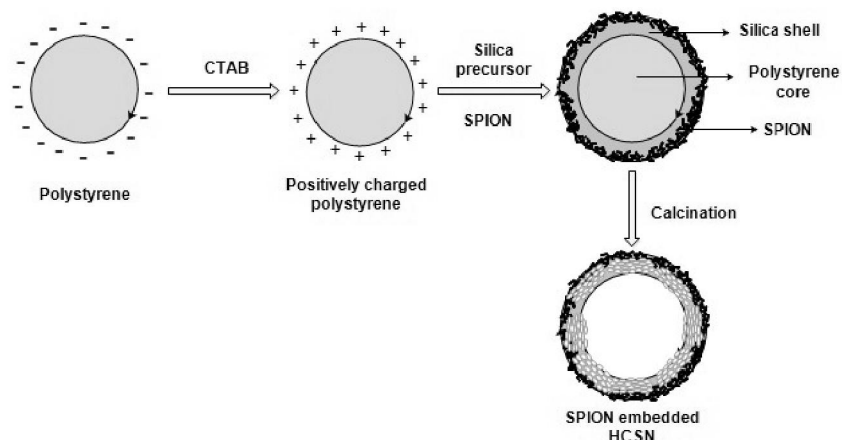
Figure 4.50 Schematic representation of synthesis of SPION embedded HCSNs using PS template

4.4.4 Radiofrequency induced heating and drug release studies for SPION embedded HCSNs

The rise in temperature with time was determined for SPION embedded HCSNs (SPION varied as 10, 20 and 30 mg) while radiofrequency heating was induced (Figure 4.51a). The rapid rise in temperature of 4 ^{0}C/minute was observed at the initial period for HCSNs embedded with 30 mg of SPION. The heating rate was found to increase with increase in the quantity of SPION added. Maximum temperatures achieved through the radio frequency heating at 20 minutes for samples T_{f1}, T_{f2} and T_{f3} were 55, 51 and 47 ^{0}C respectively. These temperature rises would be sufficient for radiofrequency monitored heating in drug release studies (Kovacik et al. 2012).

101
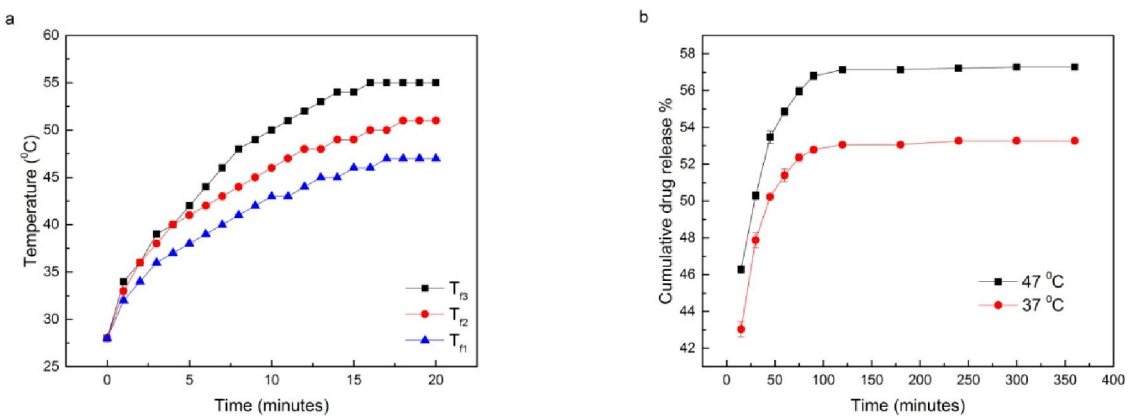
Figure 4.51 a) Temperature rise with time on radio frequency heating; b) Doxorubicin release study for T_{f2}

The doxorubicin loading and release studies were carried out for SPION embedded HCSNs at 37 ^{0}C and 47 ^{0}C. Loading capacity and encapsulation efficiency of HCSNs were assessed according to the literature (Mhlanga and Ray 2015). The loading capacity and encapsulation efficiency were found to be 1.18 % and 41.34 % (using equation 4 and 5) respectively. The cumulative drug release plot of SPION embedded HCSNs was depicted in Figure 4.51b. Rapid release of drug was observed during the initial period (0-15 minutes), as a result of leaching of drugs present on the surface and the pore entrances (Ayad et al. 2016). The cumulative drug release plot for sample T_{f2} at 37 ^{0}C and 47 ^{0}C are displayed in Figure 4.51b. The doxorubicin release from SPION embedded HCSNs was found to be temperature dependent as observed. At a higher temperature (47 ^{0}C), quick release of doxorubicin was observed (i.e. 50.08% doxorubicin released in 30 minutes). However, at 37 ^{0}C, 47.86% of doxorubicin was found to release from the samples.

4.4.5 Mathematical modeling of drug release from SPION embedded HCSNs synthesized using PS template
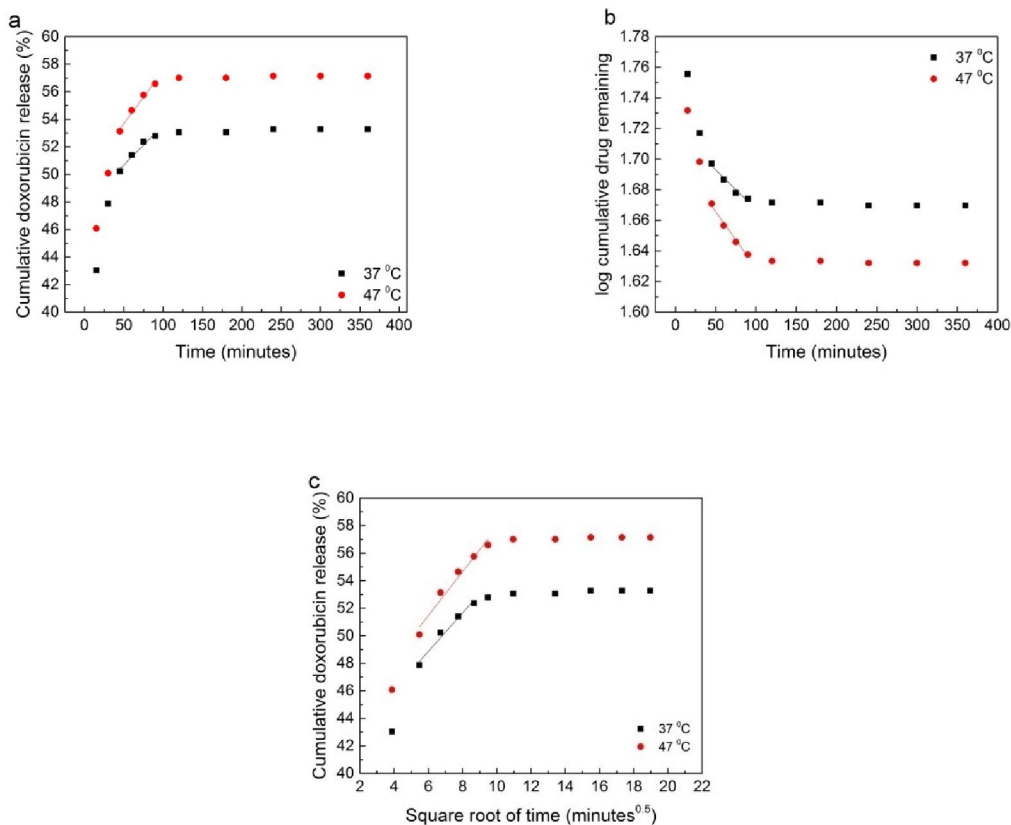
Figure 4.52 Doxorubicin release kinetics for sample T_{f2} at 37 ^{0}C and 47 ^{0}C a) Zero order; b) First order; c) Higuchi model

Models used to study the drug release behavior are zero order, first order and Higuchi models. Drug release patterns at 37 ^{0}C and 47 ^{0}C are analyzed with these models. The model fitting graphs are shown in Figure 4.52. Doxorubicin release was analyzed based on the regression coefficient R. Table 4.10 summarizes the regression coefficient R and the values of constants K_0, K_1 and K_2. The drug release from the SPION embedded HCSNs was found to show the best fit with the first order model. Thus, the release of doxorubicin from the samples was controlled by the amount of drug remaining in the SPION embedded HCSNs. Other models did not provide R^2 >0.963 (Varga et al. 2014).

The linear correlation coefficients (R^2) showed that processes are controlled by the release mechanism (Table 4.10).

Table 4.10 Correlation coefficients of mathematical models for samples T_{f2} at 37 ^{0}C and 47 ^{0}C

Temperature (^{0}C)	Zero order		First order		Higuchi model	
	K_0	R^2	K_1	R^2	K_2	R^2
37	0.058	0.961	1.18×10^{-4}	0.963	1.398	0.965
47	0.76	0.982	1.69×10^{-4}	0.985	1.591	0.952

4.4.6 Cytotoxicity studies for SPION embedded HCSNs synthesized using PS template
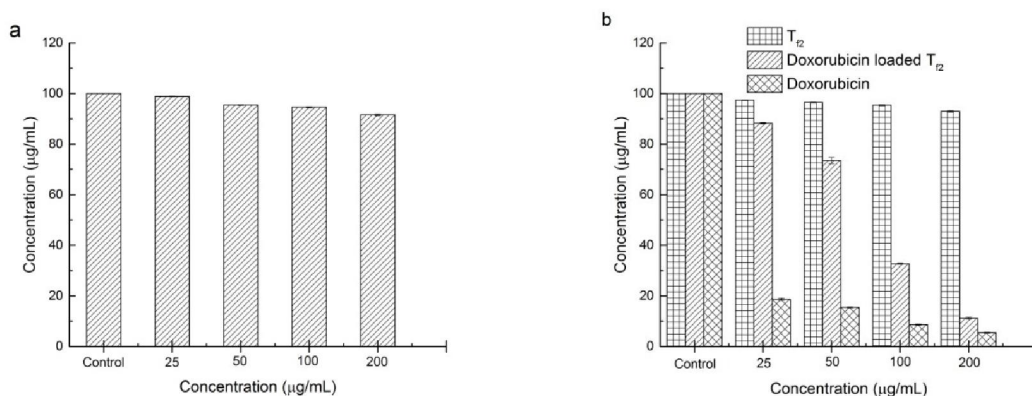
Figure 4.53 Cytotoxicity studies for sample T_{f2} on a) Normal cells (HEK 293T); b) Cancer cells (A549)

Cytotoxicity assays were utilized to assess the potential of SPION embedded HCSNs for the application in drug delivery system. The cell viability values for HEK 293T cells were found to be high, even though the concentration of samples T_{f2} was raised to 200 µg/ml (Figure 4.53). A549 cell death was examined while using samples T_{f2}, doxorubicin loaded T_{f2} and doxorubicin (Figure 4.53). Minimal cell death occurred when SPION

embedded HCSNs samples were used in the study (~7%). Cell viability was found to be very less (~5%) while doxorubicin alone was used. However, doxorubicin loaded T_{f2} samples were able to kill ~89% of the cancer cells when used at 200 μg/ml.

4.4.7 Comparison of the properties of HCSNs and SPION embedded HCSNs

Properties of HCSNs synthesized using templates such as PS, sulfonated PS, nitrated PS and SPION embedded HCSNs were compared to the study effect on drug delivery application. Table 4.11 gives the list of properties such as thickness of the shell, specific surface area, pore diameter, loading capacity, encapsulation efficiency, drug release time and maximum drug released for the HCSNs and SPION embedded HCSNs samples.

Table 4.11 Properties of HCSNs and SPION embedded HCSNs

Sample Name	Thickness of the shell (nm)	Specific surface area (m^2/g)	Pore diameter (nm)	Encapsulation efficiency (wt%)	Drug release time (minutes)	Maximum drug released (%)
T_1	15	747.5	1.5	35.7	200	51.7
T_2	20	617.3	1.3	33.01	200	47.6
T_3	30	600.8	1.2	32.3	200	44.8
Ts_1	20	644.1	1.5	45.4	300	50.7
Ts_2	40	391.5	2.7	39.1	300	46.3
Ts_3	60	197.8	3.4	37.4	300	38.9
Tn_1	15	533.6	2.6	38.5	250	57.5
Tn_2	20	291.9	3.4	36.5	250	56.8
Tn_3	35	130.5	3.7	36.2	250	48.6
T_{f2}	20	525.3	8.02	41.34	200	53.3

Properties of the silica nanoparticles such as thickness of the silica shell, pore diameter and specific surface area had played major role in controlling the drug release properties of them. HCSNs samples synthesized using PS showed thickness ranging from 15 to 30 nm. The specific surface area exhibited by T_1, T_2 and T_3 were found to be highest among the other samples and the pore sizes were found to be in microporous size range (< 2 nm). However, encapsulation efficiency was observed to be lowest (35.7 to 32.3 %) compared to other samples. Drug release time was found to be minimum for samples T_1, T_2 and T_3

ie. 200 minutes with maximum drug released in the range of 51.7 to 44.8 %. HCSNs samples synthesized using nitrated PS exhibited silica shell thickness from 15 to 35 nm with lowest specific surface area and highest pore size compared to other samples (Table 4.11). Samples Tn_1, Tn_2 and Tn_3 observed to have encapsulation efficiency from 38.5 to 36.2 % and showed highest drug release in the range 57.5 to 48.6 % in comparison with other samples. SPION embedded HCSNs samples had highest pore diameter of 8 nm and showed drug release time of 200 minutes. HCSNs samples synthesized using sulfonated PS showed higher thickness compared to the HCSNs synthesized using PS and nitrated PS templates. The encapsulation efficiencies of samples Ts_1, Ts_2 and Ts_3 were found to be higher compared to the other samples. HCSNs synthesized using sulfonated PS showed a maximum release period of 300 minutes with maximum drug released in the range of 50.7 to 38.9 %. Thus application of HCSNs synthesized using sulfonated PS in sustained release of doxorubicin is advantageous compared to the other synthesized samples (T_1, T_2, T_3, Tn_1, Tn_2, Tn_3 and T_{f2}).

Chapter 5

5. SUMMARY AND CONCLUSIONS

5.1 Summary

Hollow core shell silica nanoparticles (HCSNs) have made notable impact in the field of targeted drug delivery systems due to their unique properties (tunable morphology, large specific surface area and biocompatibility). In the present research work, HCSNs were synthesized successfully by sacrificial polymer template method. Various templates like polystyrene nanoparticles, nitrated polystyrene nanoparticles and sulfonated polystyrene nanoparticles were used. Functionalized PS templates were found to be advantageous in improving the morphology of HCSNs (shell thickness and pore size). HCSNs were used as drug carriers and the drug loading and release properties were studied in detail using doxorubicin as model drug. SPIONs were embedded in HCSNs and effect of temperature on drug release rate was determined. HCSNs synthesized using sulfonated PS was found to be advantageous in sustained release of doxorubicin compared to the other synthesized samples. The release profiles were fitted in various kinetic models (zero order, first order and Higuchi model) to assess the release mechanism and the cytotoxicity studies were carried out to assess the biocompatibility. The results revealed that HCSNs and SPION embedded HCSNs are biocompatible and can be potentially used as drug delivery vector in biomedical applications.

5.2 Conclusions

The need for stable and versatile drug delivery vector to treat cancer is marked by analyzing the earlier literature. Major researches focused on developing a drug delivery vector using mesoporous nanoparticles rather than hollow core-shell nanoparticle due to ease of synthesis techniques. In the present study, HCSNs were synthesized by sacrificial polymer template method using various templates such as polystyrene nanoparticles,

nitrated polystyrene nanoparticles and sulfonated polystyrene nanoparticles. The major findings of the present study are listed below.

- Monodispersed PS nanoparticles of size 150±20 nm with zeta potential of -52.6 mV were synthesized by emulsion polymerization method.
- HCSNs synthesized using PS template showed a variation in the following parameters, thickness from 15 nm to 30 nm, surface area from 747.5 m^2/g to 600.8 m^2/g and pore sizes ranged from 1.5 nm to 1.2 nm. Sample with highest thickness showed delayed doxorubicin release up to 200 minutes.
- Sulfonation of PS with size 160±20 nm was achieved using concentrated sulfuric acid and the presence of sulfonic acid group was confirmed by FTIR analysis. Sulfonated PS nanoparticles had lower zeta potential than PS nanoparticles by ~10 mV.
- HCSNs synthesized using sulfonated PS template showed a variation in the following parameters, thickness varied from 20 nm to 60 nm, surface area varied from 644.1 m^2/g to 197.8 m^2/g and pore sizes ranged from 1.5 nm to 3.4 nm. A delay in release for 300 minutes was achieved for sample with highest thickness at pH 7.4.
- Nitrated PS nanoparticles with size 170±20 nm were synthesized by using mixture of nitric acid and sulfuric acid and the presence of nitro group is confirmed by FTIR analysis result.
- The HCSNs samples synthesized using nitrated PS template showed shell thickness from 15 nm to 35 nm, exhibited pore size of 2.6-3.7 nm and surface area of 533.6 m^2/g to 130.5 m^2/g. In vitro release studies carried out for HCSNs using doxorubicin drug showed sustained release for 250 minutes at pH 7.4.
- SPION embedded HCSNs were synthesized using sacrificial PS template and found to have specific surface area 406.3 to 527.1 m^2/g and pore size around 8 nm.
- Radio frequency induced heating of SPION embedded HCSNs from room temperature (28 ^{0}C) caused a maximum rise in temperature up to 55 ^{0}C in 20 minutes for HCSNs sample with 30 mg of SPION. The doxorubicin release from SPION embedded HCSNs has showed a temperature dependent release. Rapid release of drug was observed at higher temperature of 47 ^{0}C.

- HCSNs synthesized using sulfonated PS showed maximum release period with maximum drug released in the range of 50.7 to 38.9 %. Thus, application of HCSNs synthesized using sulfonated PS in sustained release of doxorubicin is advantageous compared to the other synthesized samples (T_1, T_2, T_3, Tn_1, Tn_2, Tn_3 and T_{f2}).

- Release kinetics of HCSNs and SPION embedded HCSNs showed best fit for first order model.

- Cytotoxicity studies disclosed that HCSNs and SPION embedded HCSNs did not cause much cell death (<10 %). But doxorubicin loaded samples were able to kill >85% of the cancer cells.

- HCSNs synthesized using sulfonated PS showed a maximum release period of 300 minutes with maximum drug released in the range of 50.7 to 38.9 %. Thus application of HCSNs synthesized using sulfonated PS in sustained release of doxorubicin is advantageous compared to the other synthesized samples (T_1, T_2, T_3, Tn_1, Tn_2, Tn_3 and T_{f2}).

- Thus, we anticipate the use of HCSNs and SPION embedded HCSNs as drug carriers to satisfy the demands of targeted drug delivery systems.

5.3 Future scope

- Synthesis and characterization of hollow core shell silica nanoparticles using polymer templates, other than PS.

- In vivo studies of drug delivery using HCSNs

- Functionalization of HCSNs based on specific drug properties

REFERENCES

Agrawal, M., Pich, A., Gupta, S., Zafeiropoulos, N. E., Simon, P., and Stamm, M. (2008). "Synthesis of novel tantalum oxide sub-micrometer hollow spheres with tailored shell thickness." *Langmuir*, 24(3), 1013–1018.

Aimable, A., Sorbier, M. Q., Pagnoux, C., and Tessier-Doyen, N. (2017). "Processing alumina spheres by a colloidal route using silica-polystyrene hybrid nanoparticles." *J. Eur. Ceram.* Soc., 37(16), 5149–5156.

Alavi, M., Karimi, N., and Safaei, M. (2017). "Application of various types of liposomes in drug delivery systems." *Adv. Pharm. Bull.*, 7(1), 3–9.

Antonietti, M., Bremser, W., Muschenborn, D., Rosenauer, C., Schupp, B., and Schmidt, M. (1991). "Synthesis and size control of polystyrene latices via polymerization in microemulsion." *Macromolecules*, 24(25), 6636–6643.

Ayad, M. M., Salahuddin, N. A., El-Nasr, A. A., and Torad, N. L. (2016). "Amine-functionalized mesoporous silica KIT-6 as a controlled release drug delivery carrier." *Microporous Mesoporous Mater.*, 229, 166–177.

Balakrishnan, V., Azwana, H., Wab, A., Razak, K. A., and Shamsuddin, S. (2013). "In vitro evaluation of cytotoxicity of colloidal amorphous silica nanoparticles designed for drug delivery on human cell lines." *J. Nanomater.*, 2013, 1–8.

Berru, S. R., Saniger, J. M., Flores, F. J., and Espindola, M. S. (2013). "Simple method for the controlled growth of SiO2 spheres." *J. Mater. Sci. Eng. A*, 3(4), 237–242.

Bo, Q., Eun, N. G., Jae, C. H., and Yuanzhe, P. (2013). "Synthesis of monodisperse hollow carbon nanocapsules by using protective silica shells." *Asian J. Chem.*, 8, 765–770.

Bonham, J. A., Faers, M. A., and Duijneveldt, J., S. Van. (2014). "Non-aqueous microgel particles: synthesis, properties and applications." *Soft Matter*, 10(47), 9384–9398.

Bouchoucha, M., Cote, M. F., Gaudreault, C. R., Fortin, M. A., and Kleitz, F. (2016). "Size-controlled functionalized mesoporous silica nanoparticles for tunable drug release and enhanced anti-tumoral activity." *Chem. Mater.*, 28(12), 4243–4258.

Bourgeat-Lami, E., and Lang, J. (1998). "Encapsulation of inorganic particles by dispersion polymerization in polar media 1. Silica nanoparticles encapsulated by polystyrene." J. *Colloid Interface Sci.*, 197(2), 293–308.

Brijmohan, S. B., Swier, S., Weiss, R. A., and Shaw, M. T. (2005). "Synthesis and characterization of cross-linked sulfonated polystyrene nanoparticles." *Ind. Eng. Chem. Res.*, 44(21), 8039–8045.

Brinker, C. J. (1988). "Hydrolysis and condensation : effects on structure." 100, 31–50.

Chen, S., Gordin, M. L., Yi, R., Howlett, G., Sohn, H., and Wang, D. (2012). "Silicon core – hollow carbon shell nanocomposites with tunable buffer voids for high capacity anodes of lithium-ion batteries w." *Phys. Chem. Chem. Phys.*, 14, 12741–12745.

Chen, Y. (2012). "Design, synthesis, multifunctionalization and biomedical applications of multifunctional mesoporous silica-based drug delivery nanosystems". Springer, Springer Verlag Berlin, Heidelberg. 1-80.

Chen, Y., Chen, H., Zeng, D., Tian, Y., Chen, F., Feng, J., and Shi, J. (2010). "Core/shell structured hollow mesoporous nanocapsules : a potential platform for simultaneous cell imaging and anticancer drug delivery." *ACS Nano*, 4(10), 6001–6013.

Chen, Z., Niu, D., Li, Y., and Shi, J. (2013). "One-step approach to synthesize hollow mesoporous silica spheres co-templated by an amphiphilic block copolymer and cationic surfactant." *RSC Adv.*, 3(19), 6767–6770.

Costa, P., and Lobo, J. M. S. (2001). "Modelling and comparison of dissolution profiles." *Eur. J. Pharm. Sci.*, 13(2), 123–133.

Danhier, F., Feron, O., and Preat, V. (2010). "To exploit the tumor microenvironment:

passive and active tumor targeting of nanocarriers for anti-cancer drug delivery." *J. Control. Release*, 148(2), 135–146.

Denard, B., Lee, C., and Ye, J. (2012). "Doxorubicin blocks proliferation of cancer cells through proteolytic activation of CREB3L1." *Elife*, 2012(1), 2011–2013.

Deng, T. S., Bongard, H. J., and Marlow, F. (2015). "A one-step method to coat polystyrene particles with an organo-silica shell and their functionalization." *Mater. Chem. Phys.*, 162, 548–554.

Deng, Z., Wu, L., Chen, M., Zhou, S., and You, B. (2006). "A novel method for the fabrication of monodisperse hollow silica spheres." *Langmuir*, 22(14), 6403–6407.

Ding, X., Yu, K., Jiang, Y., Hari-Bala, Zhang, H., and Wang, Z. (2004). "A novel approach to the synthesis of hollow silica nanoparticles." *Mater. Lett.*, 58(27-28), 3618–3621.

Dobo, D. G., Berkesi, D., and Kukovecz, A. (2017). "Morphology conserving aminopropyl functionalization of hollow silica nanospheres in toluene." *J. Mol. Struct.*, 1140, 83–88.

Du, X., and He, J. (2008). "Facile size-controllable syntheses of highly monodisperse polystyrene nano- and microspheres by polyvinylpyrrolidone-mediated emulsifier-free emulsion polymerization." *J. Appl. Polym. Sci.*, 108(3), 1755–1760.

Edewele, R. O. (2010). "Polymer science and technology". CRC Press, Boca Raton, New York, 110-123.

Elhissi, A. M. a, Ahmed, W., Hassan, I. U., Dhanak, V. R., and D'Emanuele, A. (2001). "Carbon nanotubes: from basic research to nanotechnology." Springer, 30-150.

Ge, C., Zhang, D., Wang, A., Yin, H., Ren, M., Liu, Y., Jiang, T., and Yu, L. (2009). "Synthesis of porous hollow silica spheres using polystyrene-methyl acrylic acid latex template at different temperatures." *J. Phys. Chem. Solids*, 70(11), 1432–1437.

Gharibe, S., Afshar, S., and Vafayi, L. (2011). "Synthesis and characterization of porous hollow silica nanoparticles using ZnSe core as template for drug delivery application." *African J. Pharmacy Pharmacol.*, 5(20), 2265–2271.

Gorsd, M. N., Blanco, M. N., and Pizzio, L. R. (2012). "Synthesis of polystyrene microspheres to be used as template in the preparation of hollow spherical materials : study of the operative variables." *Procedia Mater. Sci.*, 1, 432–438.

Gorsd, M. N., Pizzio, L. R., and Blanco, M. N. (2015). "Synthesis and characterization of hollow silica spheres." *Procedia Mater. Sci.*, 8, 567–576.

Gowariker, V. R., Viswanathan, N. V, and Sreedhar, J. (2015). "Polymer science". New age international publishers, New Delhi, 1-100.

Guan, B., Wang, T., Zeng, S., Wang, X., An, D., Wang, D., Cao, Y., and Ma, D. (2013). "A versatile cooperative template-directed coating method to synthesize hollow and yolk-shell mesoporous zirconium titanium oxide nanospheres as catalytic reactors." *Nano Res.*, 7, 246–262.

Guo, L., Gao, G., Liu, X., and Liu, F. (2009). "Synthesis of polystyrene/TiO2 core-shell materials." *Chinese J. Polym. Sci.*, 27(2), 149–155.

Hacene, Y. C., Singh, A., and Mooter, G. Van Den. (2016). "Drug loaded and ethylcellulose coated mesoporous silica for controlled drug release prepared using a pilot scale fluid bed system." *Int. J. Pharm.*, 506(1-2), 138–147.

Havanur, S., and JagadeeshBabu, P. E. (2018). "Role of graphene quantum dots synthesized through pyrolysis in the release behavior of temperature responsive poly (N,N-diethyl acrylamide) hydrogel loaded with doxorubicin." *Int. J. Polym. Anal. Charact.*, 23(7), 606–620.

He, Q., and Shi, J. (2011). "Mesoporous silica nanoparticle based nano drug delivery systems: Synthesis, controlled drug release and delivery, pharmacokinetics and biocompatibility." *J. Mater. Chem.*, 21(16), 5845–5855.

He, Q., Zhang, Z., Gao, F., Li, Y., and Shi, J. (2011). "In vivo biodistribution and urinary excretion of mesoporous silica nanoparticles: Effects of particle size and PEGylation." *Small*, 7(2), 271–280.

Holzapfel, V., Musyanovych, A., Landfester, K., Lorenz, M. R., and Maila, V. (2005). "Preparation of fluorescent carboxyl and amino functionalized polystyrene particles by miniemulsion polymerization as markers for cells." *Macromol. Chem. Phys.*, 206, 2440–2449.

Huang, H., Lu, J., Wang, M., and Ge, X. (2018). "Cagelike porous sulfonated polystyrene@polyaniline composite microspheres for high-performance supercapacitor." *J. Mater. Sci.*, 53(12), 9160–9169.

Huh, S., Wiench, J. W., Yoo, J., Pruski, M., and Lin, V. S. (2003). "Organic functionalization and morphology control of mesoporous silicas via a co-condensation synthesis method." *Chem. Mater.*, 15(22), 4247–4256.

Hwang, S. W., Umar, A., Dar, G. N., Kim, S. H., and Badran, R. I. (2014). "Synthesis and characterization of iron oxide nanoparticles for phenyl hydrazine sensor applications." *Sens. Lett.*, 12(1), 97–101.

Jiao, Y., Guo, J., Shen, S., Chang, B., Zhang, Y., Jiang, X., and Yang, W. (2012). "Synthesis of discrete and dispersible hollow mesoporous silica nanoparticles with tailored shell thickness for controlled drug release." *J. Mater. Chem.*, 22(34), 17636–17643.

Kafshgari, M. H., Mazare, A., Distaso, M., Goldmann, W. H., Peukert, W., Fabry, B., and Schmuki, P. (2019). "Intracellular Drug Delivery with Anodic Titanium Dioxide Nanotubes and Nanocylinders." *ACS Appl. Mater. Interfaces*, 11(16), 14980–14985.

Kaiyi, L., and Zhaoqun, W. (2007). "A novel method for preparing monodispersed polystyrene nanoparticles." *Front. Chem. China*, 2(1), 17–20.

Keshavarz, M., and Ahmad, N. (2013). "Characterization and modification of

mesoporous silica nanoparticles prepared by sol-gel." J. Nanoparticles, 2013, 1–4.

Kim, J. H., Son, M., Sohn, Y., and Shin, W. G. (2013). "Hollow SiO_2 nanospheres : one-step synthesis by introducing guest Ag nanoparticles and an irradiating electron beam under ambient condition." *Aerosol air Qual. reseach*, 13, 415–420.

Kim, M. S., Kim, S. K., Lee, J. Y., Kim, J., and Lee, S. (2008). "Synthesis of polystyrene nanoparticles with monodisperse size distribution and positive surface charge using metal stearates." *Macromol. Res.*, 16(2), 178–181.

Kim, S., Kim, C. A., Choi, Y. H., and Jung, M. Y. (2009). "Synthesis of polystyrene nanoparticles with different surface modification by emulsion polymerization and measurement of IgG adsorption and stability for the application in latex-protein complex based solid-phase immunoassay." *Polym. Bull.*, 32, 23–32.

Knezevic, N. Z., Ruiz-Hernandez, E., Hennink, W. E., and Maria, V.-R. (2013). "Magnetic mesoporous silica-based core/shell nanoparticles for biomedical applications." *RSC Adv.*, 3(25), 9584.

Kobayashi, Y., Morimoto, H., Nakagawa, T., Kubota, Y., Gonda, K., and Ohuchi, N. (2013). "Fabrication of hollow particles composed of silica containing gadolinium compound and magnetic resonance imaging using them." *J. Nanostructure Chem.*, 3(1), 11.

Kong, F. Y., Zhang, J. W., Li, R. F., Wang, Z. X., Wang, W. J., and Wang, W. (2017). "Unique roles of gold nanoparticles in drug delivery, targeting and imaging applications." *Molecules*, 22(9).

Kopanja, L., Kralj, S., Zunic, D., Loncar, B., and Tadic, M. (2016). "Core-shell superparamagnetic iron oxide nanoparticle (SPION) clusters: TEM micrograph analysis, particle design and shape analysis." *Ceram. Int.*, 42(9), 10976–10984.

Kovacik, P., Kremlackova, Z., and Stepanek, F. (2012). "Investigation of radiofrequency induced release kinetics from magnetic hollow silica microspheres." *Microporous*

Mesoporous Mater., 159, 119–125.

Kucera, F., and Jancar, J. (1996). "Preliminary study of sulfonation of polystyrene by homogeneous and heterogeneous reaction." *Chem. Pap.*, 50(4), 224–227.

Kuhlmann, J. (1997). "Drug research: from the idea to the product." *Int. J. Clin. Pharmacol Ther.*, 35(12), 541–552.

Kumar, A., and Himanshu, M. (2014). "Nanoengineered mesoporous silica nanoparticles for smart delivery of doxorubicin." *J. Nanoaparticle Res.*, 16, 2515–2524.

Kumar, S., Poonia, N., Madaan, K., Lather, V., and Pandita, D. (2014). "Dendrimers in drug delivery and targeting: Drug-dendrimer interactions and toxicity issues." *J. Pharm. Bioallied Sci.*, 6(3), 139.

Kwon, S., Singh, R. K., Perez, R. a, Abou Neel, E. a, Kim, H.-W., and Chrzanowski, W. (2013). "Silica-based mesoporous nanoparticles for controlled drug delivery." *J. Tissue Eng.*, 4, 1–18.

Lee, C. H., Lo, L. W., Mou, C. Y., and Yang, C. S. (2008). "Synthesis and characterization of positive-charge functionalized mesoporous silica nanoparticles for oral drug delivery of an anti-inflammatory drug." *Adv. Funct. Mater.*, 18(20), 3283–3292.

Lee, J. E., Lee, N., Kim, H., Kim, J. H. J. H., Choi, S. H., Kim, T., Song, I. C., Park, S. P., Moon, W. K., and Hyeon, T. (2010). "Uniform mesoporous dye-doped silica nanocrystals for simultaneous enhanced magnetic resonance imaging, fluorescence imaging, and drug delivery." *J. Am. Chem. Soc.*, 132(2), 552–557.

Lei, J., and Zhou, G. (2014). "Polystyrene microbeads by dispersion polymerization: Effect of solvent on particle morphology." *Int. J. Polym. Sci.*, 2014.

Li, G., Li, C., Tang, H., Cao, K., Chen, J., and Jin, Y. (2010). "A facile approach to fabrication of PbS hollow spheres with improved polystyrene templates." *Mater. Lett.*, 64(24), 2755–2758.

Li, M., Zhang, C., Yang, X. L., and Xu, H. B. (2013). "Controllable synthesis of hollow mesoporous silica nanoparticles templated by kinetic self-assembly using a gemini surfactant." *RSC Adv.*, 3(37), 16304–16307.

Li, Z. Z., Wen, L. X., Shao, L., and Chen, J. F. (2004). "Fabrication of porous hollow silica nanoparticles and their applications in drug release control." *J. Control. Release*, 98(2), 245–254.

Liberman, A., Mendez, N., Trogler, W. C., and Kummel, A. C. (2014). "Synthesis and surface functionalization of silica nanoparticles for nanomedicine." *Surf. Sci. Rep.*, 69(2-3), 132–158.

Lim, E. K., Jang, E., Lee, K., Haam, S., and Huh, Y. M. (2013). "Delivery of cancer therapeutics using nanotechnology." *Pharmaceutics*, 5(2), 294–317.

Liu, B., Wang, Y., Zhang, M., and Zhang, H. (2016). "Initiator systems effect on particle coagulation and particle size distribution in one-step emulsion polymerization of styrene." *Polymers*, 8(2), 1–14.

Liu, C., Ge, C., Wang, A., Yin, H., Ren, M., Zhang, Y., Yu, L., and Jiang, T. (2011). "Synthesis of porous hollow silica spheres using functionalized polystyrene latex spheres as templates." *Korean J. Chem. Eng.*, 28(6), 1458–1463.

Liu, C., Yin, H. B., Wang, A. L., Wu, Z. A., Wu, G., Jiang, T., Shen, Y. T., and Jiang, T. S. (2012). "Size-controlled preparation of hollow silica spheres and glyphosate release." *Trans. Nonferrous Met. Soc. China*, 22(5), 1161–1168.

Liu, S., and Zhao, H. (2016). "An in-depth investigation on the formation of nanoporous silica microspheres in diluted dodecylamine solutions." *J. Exp. Nanosci.*, 11(7), 490–499.

Lopez, M. B., Teijeiro, A., and Rivas, J. (2013). "Magnetic nanoparticle-based hyperthermia for cancer treatment." *Reports Pract. Oncol. Radiother.*, 18(6), 397–400.

Maria, G., Berger, D., Nastase, S., and Luta, I. (2012). "Kinetic studies on the irinotecan

release based on structural properties of functionalized mesoporous-silica supports." *Microporous Mesoporous Mater.*, 149(1), 25–35.

Mhlanga, N., and Ray, S. S. (2015). "Kinetic models for the release of the anticancer drug doxorubicin from biodegradable polylactide/metal oxide-based hybrids." *Int. J. Biol. Macromol.*, 72, 1301–1307.

Milosevic, I., Mauroy, V., Dabboue, H., Serieye, S., Warmont, F., Salvetat, J. P., Saboungi, M. L., and Guillot, S. (2009). "Synthesis and size control of polystyrene nanoparticles via 'liquid crystalline' nanoemulsion." *Microporous Mesoporous Mater.*, 120, 7–11.

Mitran, R.-A., Matei, C., and Berger, D. (2016). "Correlation of mesoporous silica structural and morphological features with theoretical three-parameter model for drug release kinetics." *J. Phys. Chem. C*, 120(51), 29202–29209.

Mohamed El-Toni, A., Khan, A., Abbas Ibrahim, M., Puzon Labis, J., badr, G., Al-Hoshan, M., Yin, S., and Sato, T. (2012). "Synthesis of double mesoporous core-shell silica spheres with tunable core porosity and their drug release and cancer cell apoptosis properties." *J. Colloid Interface Sci.*, 378(1), 83–92.

Mulens, V., Morales, P., and Barber, D. F. (2013). "Development of magnetic nanoparticles for cancer gene therapy : a comprehensive review." *ISRN Nanomater.*, 2013, 14.

Nalbandian, L., Patrikiadou, E., Zaspalis, V., Patrikidou, A., Hatzidaki, E., and Papandreou, C. N. (2016). "Magnetic nanoparticles in medical diagnostic applications: synthesis, characterization and proteins conjugation." *Curr. Nanosci.*, 12, 455–468.

Nandiyanto, A. B. D., Kim, S. G., Iskandar, F., and Okuyama, K. (2009). "Synthesis of spherical mesoporous silica nanoparticles with nanometer-size controllable pores and outer diameters." *Microporous Mesoporous Mater.*, 120(3), 447–453.

Nguyen, A. T., Park, C. W., and Kim, S. H. (2014). "Synthesis of hollow silica by stober

method with double polymers as templates." *Bull. Korean Chem. Soc.*, 35(1), 173–176.

Niu, D., Ma, Z., Li, Y., and Shi, J. (2010). "Synthesis of core-shell structured dual-mesoporous silica spheres with tunable Pore size and controllable shell thickness." *J. Am. Chem. Soc.*, 132(43), 15144–15147.

Obayemi, J. D., Danyuo, Y., Dozie N., S., Odusanya, O. S., Anuku, N., Malatesta, K., Yu, W., Uhrich, K. E., and Soboyejo, W. O. (2016). "PLGA-based microparticles loaded with bacterial-synthesized prodigiosin for anticancer drug release: Effects of particle size on drug release kinetics and cell viability." Mater. Sci. Eng. C, 66, 51–65.

Ogi, T., Bayu, A., Nandiyanto, D., and Okuyama, K. (2014). "Nanostructuring strategies in functional fine-particle synthesis towards resource and energy saving applications." *Adv. Powder Technol.*, 25(1), 3–17.

Park, I., Ko, S. H., An, Y. S., Choi, K. H., Chun, H., Lee, S., and Kim, G. (2009). "Monodisperse polystyrene-silica core-shell particles and silica hollow spheres prepared by the stober method." *J. Nanosci. Nanotechnol.*, 9(12), 7224–7228.

Peng, W., Zhang, Z., Rong, M., and Zhang, M. (2019). "Core-shell structure design of hollow mesoporous silica nanospheres based on thermo-sensitive PNIPAM and pH-responsive catechol-Fe(3+) complex." *Polymers*, 11, 1–15.

Philippides, A., Budd, P. M., Price, C., and Cuncliffe, A. V. (1993). "The nitration of polystyrene." *Polymer*, 34(16), 3509–3513.

Rani, K., and Paliwal, S. (2014). "A review on targeted drug delivery: its entire focus on advanced therapeutics and diagnostics." *J. Appl. Med. Sci.*, 2(1C), 328–331.

Sandberg, L. I. C., Gao, T., Jelle, B. P., and Gustavsen, A. (2013). "Synthesis of hollow silica nanospheres by sacrificial polystyrene templates for thermal insulation applications." *Adv. Mater. Sci. Eng.*, 2013, 1–6.

She, X., Chen, L., Velleman, L., Li, C., Zhu, H., He, C., Wang, T., Shigdar, S., Duan, W.,

and Kong, L. (2015). "Fabrication of high specificity hollow mesoporous silica nanoparticles assisted by Eudragit for targeted drug delivery." *J. Colloid Interface Sci.*, 445, 151–160.

Shin, K., Kim, J. J., and Suh, K. Do. (2010). "A facile process for generating monolithic-structured nano-silica/polystyrene multi-core/shell microspheres by a seeded sol-gel process method." *J. Colloid Interface Sci.*, 350(2), 581–585.

Shultsev, A. L. (2013). "Preparation of 4-nitrostyrene." *Russian Gen. Chem.*, 83(10), 1859–1863.

Siamak, J., and Hassan, N. (2018). "Doxorubicin loaded carboxymethyl cellulose/graphene quantum dot nanocomposite hydrogel films as a potential anticancer drug delivery system." *Mater. Sci. Eng. C*, 87, 50–59.

Slowing, I. I., Vivero-Escoto, L, J., Wu, Chia-Wen, and Lin, V. S.-Y. Y. (2008). "Mesoporous silica nanoparticles as controlled release drug delivery and gene transfection carriers." *Adv. Drug Deliv. Rev.*, 60(11), 1278–1288.

Soleimani, E., and Mohammadi, M. (2018). "Synthesis, characterization and properties of polystyrene/NiO nanocomposites." *J. Mater. Sci. Mater. Electron.*, 29(11), 9494–9508.

Song, H. M., Anjum, D. H., Sougrat, R., Hedhilib, M. N., and Khashab, and N. M. (2012). "Hollow Au @ Pd and Au @ Pt core – shell nanoparticles as electrocatalysts for ethanol oxidation reactions †." *J. Mater. Chem.*, 22(48), 25003–25010.

Stober, W., Fink, A., and Bohn, E. (1968). "Controlled growth of monodisperse silica spheres in the micron size range." *J. Colloid Interface Sci.*, 26(1), 62–69.

Tang, F., Li, L., and Chen, D. (2012). "Mesoporous silica nanoparticles: synthesis, biocompatibility and drug delivery." *Adv. Mater.*, 24(12), 1504–1534.

Thakur, S., Pramod, K. S., and Malviya, R. (2017). "Utilization of polymeric nanoparticle in cancer treatment: a review." *J Pharma Care Heal. Sys.*, 4(2), 1–12.

Thommes, M., Kaneko, K., Neimark, A. V., Olivier, J. P., Rodriguez-Reinoso, F., Rouquerol, J., and Sing, K. S. W. (2015). "Physisorption of gases, with special reference to the evaluation of surface area and pore size distribution (IUPAC Technical Report)." *Pure Appl. Chem.*, 87(9-10), 1–19.

Tissot, I., Reymond, J. P., Lefebvre, F., and Bourgeat-Lami, E. (2002). "SiOH-functionalized polystyrene latexes. a step toward the synthesis of hollow silica nanoparticles." *Chem. Mater.*, 14(11), 1325–1331.

Varga, N., Benko, M., Sebok, D., Bohus, G., Janovak, L., and Dekany, I. (2014). "Mesoporous silica core-shell composite functionalized with polyelectrolytes for drug delivery." *Microporous Mesoporous Mater.*, 213, 2–9.

Varga, N., Benko, M., Sebok, D., Bohus, G., Janovak, L., and Dekany, I. (2015). "Mesoporous silica core-shell composite functionalized with polyelectrolytes for drug delivery." *Microporous Mesoporous Mater.*, 213(2015), 134–141.

Venkatathri, N. (2007). "Synthesis of silica nanosphere from homogeneous and heterogeneous systems." *Bull. Mater. Sci.*, 30(6), 615–617.

Vetrivel, S., Chen, C. T., and Kao, H. M. (2010). "The ultrafast sonochemical synthesis of mesoporous silica MCM-41." *New J. Chem.*, 34(10), 2109–2112.

Wang, A., and Edwards, B. J. (2016). "Modeling controlled release from hollow porous nanospheres." *Int. J. Heat Mass Transf.*, 103, 997–1007.

Wang, W., Cai, W., Yang, Y., Li, H., Cong, M., and Chen, T. (2013). "Controlled growth of metal nanoparticles on amino-functionalized polystyrene microspheres and their application in surface-enhanced Raman spectroscopy." *Mater. Chem. Phys.*, 142(2-3), 756–762.

Wu, C., Chen, X., and He, Z. (2018). "Polymer/silica hybrid hollow nanoparticles with channels and thermo-responsive gatekeepers for drug storage and release." *Colloid Polym. Sci.*, 296(12), 1961–1969.

Wu, W., Caruntu, D., Martin, A., Yu, M. H., O'Connor, C. J., Zhou, W. L., and Chen, J. F. (2007). "Synthesis of magnetic hollow silica using polystyrene bead as a template." *J. Magn. Magn. Mater.*, 311(2), 578–582.

Wu, W., He, Q., and Jiang, C. (2008). "Magnetic iron oxide nanoparticles: Synthesis and surface functionalization strategies." *Nanoscale Res. Lett.*, 3(11), 397–415.

Yamamoto, T., Nakayama, M., Kanda, Y., and Higashitani, K. (2006). "Growth mechanism of soap-free polymerization of styrene investigated by AFM." *J. Colloid Inter. Sci.*, 297, 112–121.

Yan, J., Hong, L. Y., Wang, A. J., and Kim, D. P. (2007). "Facile synthesis of SiCN ceramic foam via self-sacrificial template method." *Solid State Phenom.*, 124-126, 727–730.

Yang, J., Lind, J. U., and Trogler, W. C. (2008). "Synthesis of hollow silica and titania nanospheres." *Chem. Mater.*, 20(9), 2875–2877.

Yang, Y., Chu, Y., Yang, F., and Zhang, Y. (2005). "Uniform hollow conductive polymer microspheres synthesized with the sulfonated polystyrene template." *Mater. Chem. Phys.*, 92(1), 164–171.

Yang, Y., Chu, Y., Zhang, Y., Yang, F., and Liu, J. (2006). "Polystyrene-ZnO core-shell microspheres and hollow ZnO structures synthesized with the sulfonated polystyrene templates." *J. Solid State Chem.*, 179(2), 470–475.

Yoon, S. B., Kim, J. Y., Kim, J. H., Park, S. G., Kim, J. Y., Lee, C. W., and Yu, J. S. (2006). "Template synthesis of nanostructured silica with hollow core and mesoporous shell structures." *Curr. Appl. Phys.*, 6(6), 1059–1063.

Yoon, S. Y., Park, Y. S., and Lee, J. S. (2014). "Controlled synthesis of spherical polystyrene beads and their template-assisted manual assembly." *Bull. Korean Chem. Soc.*, 35(8), 2281–2284.

Yuan, J., Zhou, G., and Pu, H. (2008). "Preparation and properties of Nafion®/hollow silica spheres composite membranes." *J. Memb. Sci.*, 325(2), 742–748.

Yuan, J., Zhou, T., and Pu, H. (2010). "Nano-sized silica hollow spheres : preparation , mechanism analysis and its water retention property." *J. Phys. Chem. Solids*, 71(7), 1013–1019.

Yun, D. S., Lee, H. S., Jang, H. G., and Yoo, J. W. (2010). "Controlling size and distribution for nano-sized polystyrene spheres." *Bull. Korean Chem. Soc.*, 31(5), 1345–1348.

Zhang, J., Rosenholm, J. M., and Gu, H. (2012a). "Molecular confinement in fluorescent magnetic mesoporous silica nanoparticles: Effect of pore size on multifunctionality." *Chem. Phys. Chem.*, 13(8), 2016–2019.

Zhang, M., Holman, C. D. A. J., Preen, D. B., and Brameld, K. (2007). "Repeat adverse drug reactions causing hospitalization in older Australians: A population-based longitudinal study 1980-2003." *Br. J. Clin. Pharmacol.*, 63(2), 163–170.

Zhang, Q., Ge, J., Goebl, J., Hu, Y., Lu, Z., and Yin, Y. (2009a). "Rattle-type silica colloidal particles prepared by a surface-protected etching process." *Nano Res.*, 2(7), 583–591.

Zhang, S., Ren, F., Wu, W., Zhou, J., Xiao, X., Sun, L., and Jiang, C. (2013). "Controllable synthesis of recyclable core–shell -Fe2O3@SnO2 hollow nanoparticles with enhanced photocatalytic and gas sensing properties." *Phys. Chem. Chem. Phys.*, 15, 8228–8236.

Zhang, S., Xu, L., Liu, H., Zhao, Y., Zhang, Y., Wang, Q., Yu, Z., and Liu, Z. (2009b). "A dual template method for synthesizing hollow silica spheres with mesoporous shells." *Mater. Lett.*, 63(2), 258–259.

Zhang, W. H., Fan, X. D., Tian, W., and Fan, W. W. (2012b). "Polystyrene/nano-SiO 2 composite microspheres fabricated by pickering emulsion polymerization: Preparation,

mechanisms and thermal properties." *Express Polym. Lett.*, 6(7), 532–542.

Zhang, X., Zhang, L., and Yang, Q. (2014). "Designed synthesis of sulfonated polystyrene/mesoporous silica hollow nanospheres as efficient solid acid catalysts." *J. Mater. Chem. A*, 2(20), 7546–7554.

Zhao, D., Feng, J., Huo, Q., Melosh, N., Fredrickson, G. H., Chmelka, B. F., and Stucky, G. D. (1998). "Triblock copolymer syntheses of mesoporous silica with periodic 50 to 300 angstrom pores." *Science*, 279, 548–552.

Zhao, N., Woodle, M. C., and Mixson, A. J. (2018). "Nanomedicine & nanotechnology advances in delivery systems for doxorubicin." *J. Nanomed. Nanotechnol.*, 9(5), 1–9.

Zhou, X., Cheng, X., Feng, W., Qiu, K., Chen, L., Nie, W., Yin, Z., Mo, X., Wang, H., and He, C. (2014). "Synthesis of hollow mesoporous silica nanoparticles with tunable shell thickness and pore size using amphiphilic block copolymers as core templates." *Dalt. Trans.*, 43(31), 11834–11842.

Zou, H., Wu, S., and Shen, J. (2008). "Preparation of silica-coated poly(styrene-co-4-vinylpyridine) particles and hollow particles." *Langmuir*, 24(18), 10453–10461.

APPENDIX I

AI. 1Variation of reaction parameters for synthesis of polystyrene

Sample ID	KPS concentration (moles)	PVP concentration (moles)	Reaction time (hours)	Reaction temperature (^0C)
P-1	55	15	24	70
P-2	96	15	24	70
P-3	129	15	24	70
P-4	166	15	24	70
P-5	129	3.7	24	70
P-6	129	7.5	24	70
P-7	129	30	24	70
P-8	129	15	1	70
P-9	129	15	6	70
P-10	129	15	18	70
P-11	129	15	24	60
P-13	129	15	24	80

AI. 2 Variation of reaction parameters for synthesis of HCSNs using PS template

Sample ID	Water/ethanol ratio	Ammonia (mL)	CTAB (mL)	PS/TEOS ratio
S-1	100 % water	0.5	6	1:1
S-2	4:1	0.5	6	1:1
S-3	3:2	0.5	6	1:1
S-4	1:4	0.5	6	1:1
S-5	100 % ethanol	0.5	6	1:1
S-6	1:4	0.2	6	1:1
S-7	1:4	0.3	6	1:1
S-8	1:4	0.7	6	1:1
S-9	1:4	0.5	2	1:1
S-10	1:4	0.5	10	1:1
S-11	1:4	0.5	6	2:1
S-12	1:4	0.5	6	1:2
S-13	1:4	0.5	6	1:4
S-14	1:4	0.5	6	2:3
S-15	1:4	0.5	6	4:7

AI. 3 Variation of reaction parameters for synthesis of HCSNs using sulfonated PS template

Sample ID	Water/ethanol ratio	Ammonia (mL)	CTAB (mL)	PS/TEOS ratio
SS-1	1:4	0.3	10	1:1
SS-2	1:4	0.5	10	1:1
SS-3	1:4	0.7	10	1:1
SS-4	1:4	0.5	6	1:1
SS-5	1:4	0.5	8	1:1
SS-6	1:4	0.5	10	2:1
SS-7	1:4	0.5	10	1:2
SS-8	1:4	0.5	10	1:4
SS-9	1:4	0.5	10	2:3
SS-10	1:4	0.5	10	4:7

AI. 4 Variation of reaction parameters for synthesis of HCSNs using nitrated PS template

Sample ID	Water/ethanol ratio	Ammonia (mL)	CTAB (mL)	PS/TEOS ratio
SN-1	1:4	0.3	6	1:1
SN-2	1:4	0.5	6	1:1
SN-3	1:4	0.7	6	1:1
SN-4	1:4	0.5	2	1:1
SN-5	1:4	0.5	6	1:1
SN-6	1:4	0.5	10	2:1
SN-7	1:4	0.5	6	1:2
SN-8	1:4	0.5	6	1:4
SN-9	1:4	0.5	6	2:3
SN-10	1:4	0.5	6	4:7

AII. 1 Calibration curve for doxorubicin

Standard solutions of the DOX in the range of 1 to 100 ppm were prepared in milli-Q water. The absorbance was read against milli-Q water blank at 480 nm.
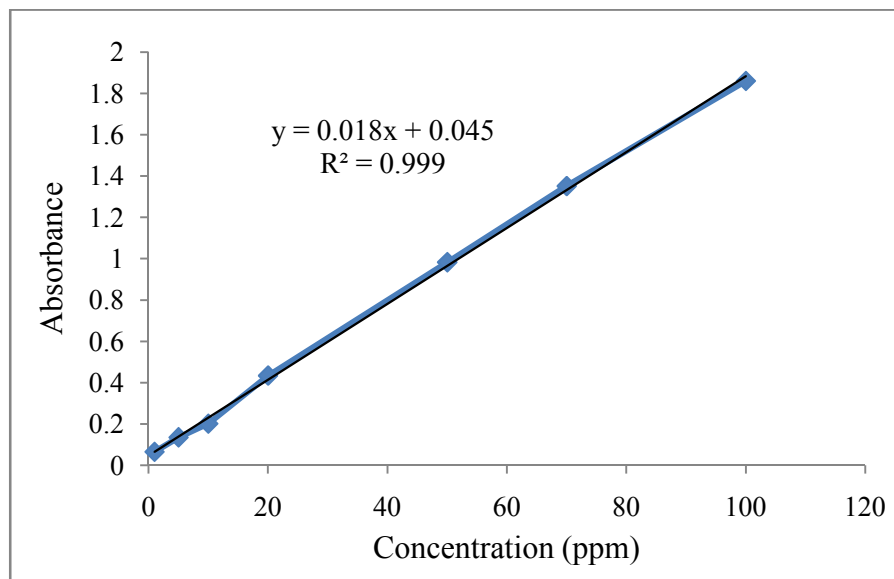
List of publications based on PhD research work

International journal publications

1. Deepika D. and Jagadeeshbabu P., E. (2018). "Synthesis and characterization of microporous hollow core-shell silica nanoparticles for controlled release of doxorubicin (HCSNs)". *Journal of Nanoparticle Research.* Springer, 20 (187), 1-15.

2. Deepika D. and Jagadeeshbabu P., E. "Sacrificial sulfonated polystyrene template assisted synthesis of mesoporous hollow core-shell silica nanoparticles (HCSNs) for drug delivery application". *Journal of bulletin of material science,* Springer, 43(213), 1-9.

3. Deepika D. and Jagadeeshbabu P., E. "Effect of pH and shell thickness on controlled release of doxorubicin from hollow core shell silica nanoparticles synthesized using nitrated polystyrene as sacrificial template". *Journal of materials today proceedings*, Elseveir, Doi: 10.1016/j.matpr.20.02.799 .

Conference Proceedings

1. Deepika D. and Jagadeeshbabu P., E. (2017). "Optimization of size and distribution of monodispersed polystyrene nanoparticles". ICONN*,* August 2017.

2. Deepika D. and Jagadeeshbabu P., E. (2019). "Sacrificial polystyrene template assisted synthesis of tunable pore size hollow core-shell silica nanoparticles (HCSNs) for drug delivery application". ICAMEN*, AIP conference* proceedings, 2148, 30016

BIODATA

DEEPIKA D

Email ID: deepika.anepalla@gmail.com

Contact no: +91-9986449077

Personal Details :

Name   : Deepika D.

Father's name   : Subrahmanya Bhat D.

Date of birth   : 03 September, 1990

Gender   : Female

Permanent address   : Deepika D, W/O Nandana M S, Shedikare house

Kalmadaka Post, Sullia, Karnataka, India - 574212

Educational qualification

- ➢ Ph.D. (Pursuing) in Chemical Engineering (CGPA – 8), 2015-2020
  Department of Chemical Engineering, NITK Surathkal, Karnataka.
- ➢ M.Tech in Chemical engineering (CGPA-9.21), 2012-2014
  SIT, Tumkur, Karnataka.
- ➢ B.Tech in Chemical engineering (CGPA-8.88), 2008-2012
  RVCE Bangalore, Karnataka.

Google scholar citations

No. of patents : 1

No. of publications : 6

Total citations : 16

Declaration:

I hereby declare that the above written particulars are true to the best of my knowledge.

Place: Surathkal, India

DEEPIKA D